LA-UR-24-21771

Title: Dust Formation and Destruction in Core Collapse Supernovae Explosions

Author(s): Stangl, Sarah Marie

Intended for: Doctoral Dissertation

Issued: 2024-04-24 (rev.1)

Los Alamos
NATIONAL LABORATORY

UNIVERSITY OF OKLAHOMA

GRADUATE COLLEGE

DUST FORMATION AND DESTRUCTION IN CORE COLLAPSE SUPERNOVAE EXPLOSIONS

A DISSERTATION

SUBMITTED TO THE GRADUATE FACULTY

in partial fulfillment of the requirements for the

Degree of

DOCTOR OF PHILOSOPHY

By

SARAH M. STANGL
Norman, Oklahoma
2024

DUST FORMATION AND DESTRUCTION IN CORE COLLAPSE SUPERNOVAE EXPLOSIONS

A DISSERTATION APPROVED FOR THE
HOMER L. DODGE DEPARTMENT OF PHYSICS AND ASTRONOMY

BY THE COMMITTEE CONSISTING OF

Dr. Mukremin Kilic, Chair

Dr. Edward Baron

Dr. Doerte Blume

Dr. Xinyu Dai

Dr. Christopher Fryer

Dr. Trina Hope

Dr. Christopher Mauney

Acknowledgements

To Dr. Christopher Mauney – Thank you for the endless patience, thoughtful guidance, and introduction to new science throughout the years.

To Dr. Eddie Baron – Thank you for your mentorship and instruction as I navigated the doctoral program.

To Dr. Mukremin Kilic – Thank you for your support and for taking me on as a student after plans changed.

To My Committee – Thank you Mukremin Kilic, Edward Baron, Doerte Blume, Xinyu Dai, Christopher Fryer, Trina Hope, and Christopher Mauney for your support and insight during the completion of this program.

To Dr. Christopher Mauney, Dr. Christopher Fryer, and Dr. Suzzanah Wood – Thank you for providing the opportunity to investigate and continue this research.

To Dr. Wesley Even, Dr. Sam Jones, and Dr. Morgan Taylor – Thank you for your work in curating the supernova data at Los Alamos National Laboratory.

To Dr. Takaya Nozawa at NAOJ – Thank you for the early assistance in code development.

This work was supported by the U.S. Department of Energy through the Los Alamos National Laboratory (LANL). LANL is operated by Triad National Security, LLC, for the National Nuclear Security Administration of U.S. Department of Energy (Contract No. 89233218CNA000001). This research used resources provided by the Darwin testbed at LANL which is funded by the Computational Systems and Software Environments subprogram of LANL's Advanced Simulation and Computing program (NNSA/DOE). This work is approved for unlimited release with report number LA-UR-24-21771.

Contents

Abstract

Dust is a crucial component of the Interstellar Medium (ISM) and an important driver in many astrophysical processes. Dust formed from evolved stars increases the metallicity of the ISM, enriching it with heavier elements. Dust makes up the source material of collapsing clouds in the ISM leading to stellar and galactic formation. The stabilization of these systems are aided by dust through absorption and scattering of excess energy. As stellar systems evolve and undergo supernova and mass loss events, enriched dust is produced, further enhancing the metallicity of the ISM. However, despite the importance of dust, the processes that produce dust are not well understood.

Core-Collapse Supernovae are one source of dust. Dying massive stars explode, sending their constituent material into the Interstellar Medium, which as the ejecta expands and cools, material condenses and nucleates forming dust grains. I investigate the formation, survivability, and properties of dust. In Chapter 2, dust grain nucleation in CCSNe is discussed. A revised formulation of Kinetic Nucleation Theory (KNT) is used to track the nucleation and growth of dust grains in the ejecta. The affects of the progenitor system on the amount and type of dust is explored, showing a strong dependence on explosion energy. I discuss the code and methods used to model dust nucleation and destruction in Chapter 3. The sputtering and erosion of dust grains in CCSNe shocks are explored in Chapter 4. The erosion and survival of this nucleated dust is modeled through thermal and non-thermal sputtering by the surrounding gas and shocks. The optical properties and scattering of light by surviving dust grains is modeled by Mie scattering in Chapter 5. A discussion of

observations of dust in variable star systems and supernovae is outlined in Chapter 6.

CHAPTER 1

Introduction

Dust is ubiquitous in the universe and is an important component of the Interstellar Medium (ISM). The main components of the ISM are gas, atoms, molecules in the gas-phase, and dust, which consists of solid-phase molecules. Dust grains act as catalysts for complex chemistry, forming molecules through gas-surface reactions (Reboussin et al., 2014). ISM dust absorbs and re-emits stellar radiation as a far-infrared thermal emission, cooling the ISM. Dust grains lock up gas-phase elements, causing a depletion in the ISM gas phase (Savage & Sembach, 1996). Heavier elements such as Fe, Si, and Ni are more strongly depleted and contribute less to the level of ionization.

Dust is an important driver in planetary, stellar, and galactic formation. ISM dust and gas make up the source material in the densest parts of the ISM where stellar formation is more likely to occur. The degree of physical and chemical processing of dust influences the metallicity of the resultant star and any planets that formed in the proto-planetary disk (PPD). Dust grains are important coolants, affecting the dynamical and thermal evolution of the proto-stellar and proto-galactic systems. As the material collapses, gravitational potential energy is released. Dust grains absorb and dissipate this energy, leading to a relaxation or stabilization of the stellar system. Without dust, the gravitational collapse would continue on producing rapid and violent formation scenarios.

Dust plays a crucial role in the formation, chemical evolution, and observations of astronomical objects. It originates from three primary sources. Dust grains nucleate in the cool, expanded envelope of asymptotic giant branch (AGB) stars and are driven into the ISM by stellar winds. New grains can form and grow on existing grains in the cold ISM. Dust grains nucleate within the expanding cooling ejecta of Core-Collapse Supernovae (CCSNe) outflows before injection into the ISM.

1.1. Observational Effects of Dust

Stars emit light as blackbody radiation. By measuring the intensity of light at each wavelength, a stellar spectrum is obtained. The wavelength with the highest intensity determines the star's absolute temperature, T, by Wien's law,

$$T = \frac{b}{\lambda_{max}} \tag{1.1}$$

where $b = 2.89 \times 10^{-1}$ cm·K is the Wien's displacement constant and λ_{max} is the peak wavelength.

Stars are divided into spectral classes based on their ionization state and temperature. Using the Morgan-Keenan system, the stars are grouped into the classes O, B, A, F, G, K, or M. Each spectral class is further divided by temperature with a digit 0, the hottest, to 9, the coolest within the class. Roman numerals I to V denote luminosity classes.

Absorption and emission lines are present within a spectra as a result of temperature differences. The temperature dictates the ionization and excitation of atoms, giving a relative abundances of ions. In high temperature regions, atoms ionize, forming ionization lines characteristic of the levels of ionization in the stellar radiation. Cold gases and molecules in the outer layers of the star absorb radiation and produce absorption lines. The strength of each line is determined by the opacity in the line compared with the continuum. Dust complicates this process, changing the radiation profile.

1.1.1. Reddening & Extinction

Dust grains scatter, absorb, and re-emit light changing the observed spectra by extinction, the total effect of scattering and absorption of radiation between the source and the observer, and reddening (Barnard, 1907, 1910; Trumpler, 1930). These effects can be determined using the pair-method, comparing differences in the spectra of an obscured object with a star of similar spectral features but has little observed obstructions (Rudnick, 1936; Trumpler, 1930).

Assuming that the extinction goes to zero as the wavelength goes towards infinity, observations of the star at longer wavelengths where extinction is negligible are used to determine the extinction as a function of wavelength (Draine, 2011). Atomic hydrogen absorbs light with $h\nu < 13.6$ eV, $\lambda > 911.6$ Å, the attenuation of dust is measurable at $\lambda > 911.6$ Å. The extinction, A_λ, is measured in magnitudes by,

$$A_\lambda = 2.5 \log_{10} \left(\frac{F_\lambda^0}{F_\lambda} \right) \tag{1.2}$$

where F_λ is the observed flux of the star and F_λ^0 is the flux that would be observed with no obstructions and only from the inverse square law, $F = \frac{L}{4\pi d^2}$ where L is the luminosity.

Another way to describe extinction is by the total-to-selective extinction ratio R_V,

$$R_V = \frac{A_V}{A_B - A_V} \tag{1.3}$$

where A_V is the total extinction in the V band, A_B is the total extinction in the B band, and $A_B - A_V$ is the reddening. Sight-lines through denser regions tend to have larger values of R_V (Draine, 2011).

Figure 1.1 shows extinction curves of different R_V values. The most prominent feature is

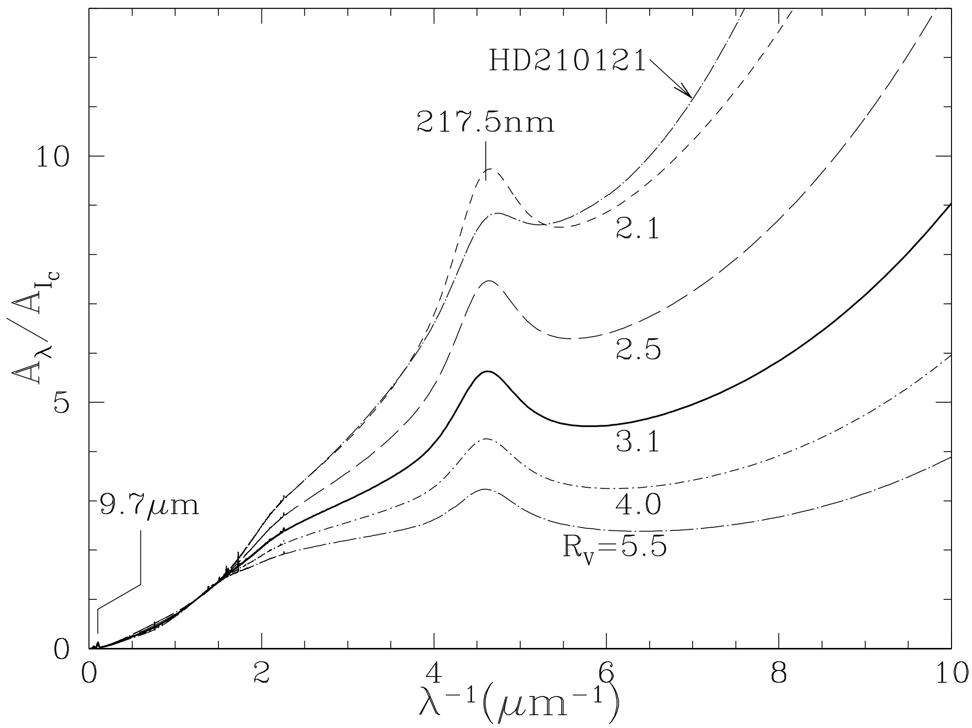

Figure 1.1: Extinction curves of varying R_V using the Fitzpatrick parametrization (Fitzpatrick, 1999). $R_V = 3.1$ are the averaged values through diffuse gases in the Milky Way. The smallest value, $R_V = 2.1$, is towards the star HD 210121 (Welty & Fowler, 1992). The largest R_V is seen towards HD 36982 (Fitzpatrick, 1999). Diffuse interstellar bands are included in the extinction. The emission features at 0.2175 and 9.7 µm are labelled. Image taken from Draine (2003).

the 2175 Å bump. The width and intensity of this feature vary across different sources, but is always present at 2175 Å (Fitzpatrick & Massa, 1986). This feature is believed to be entirely from absorption, however it is not known what material causes this feature. Because of its prevalence and strength, it is believed to be from an abundant material. Draine (2003) shows graphite particles are able to produce this feature.

1.1.2. ISM Depletion

Absorption line spectroscopy can be used to determine the elemental gas phase abundances in the ISM. Multiple gas-phase elemental abundances with respect to H have been measured with this technique. Atomic hydrogen absorbs light with $h\nu < 13.6$ eV, $\lambda > 911.6$ Å, leading to a difficulty determining the gas phase abundance of certain elements. For example Ne and Na have dominant ionization states that resonate at $\lambda < 911.6$ Å. Gas phase abundances in the ISM are expected to follow solar metallicites, but a depletion of certain elements is observed. Figure 1.2 shows the gas-phase abundances with respect to solar abundances in the diffuse cloud towards ζ Oph vs. each element's condensation temperature, the temperature at which 50% of the material would be in the solid phase. As the condensation temperature increases, the element is more depleted. Elemental material is missing from the gas phase suggesting this material is locked up in dust grains. Main contributing elements to dust grains C, Mg, Si, and Fe show significant depletion. The overabundance of gaseous S in this figure is either an observational error or from SII absorption in this region.

1.1.3. Polarization of dust Grains

The polarization of starlight was discovered when Hall (1949); Hall & Mikesell (1949); Hiltner (1949) noticed the degree of polarization was larger for stars with greater reddening and stars in a region experienced similar amounts of reddening. Unpolarized light traveling through the ISM exits linearly polarized. Figure 1.3 shows the degree of linear polarization in Heilis (2000). Polarization results when an electromagnetic wave passes through molecules, aligning them with the wave's electric field vector. Hence, dust grains are aligned by interactions with the interstellar magnetic field. This alignment suggests dust grains are ellipsoidal, not spherical. Light traveling parallel to the elongated axis of the dust is blocked, while perpendicular light will pass through. Dust grains are aligned with their shorter axis parallel to the interstellar magnetic field.

The polarization can be described by the Serkowski law (Serkowski, 1973),

$$p(\lambda) \approx p_{max} \exp\left[-K \ln^2(\frac{\lambda}{\lambda_{max}})\right] \tag{1.4}$$

with the polarization, p, peaking at $\lambda_{max} \approx 5500$ Å and $K \approx 1.15$. The amount of max polariza-

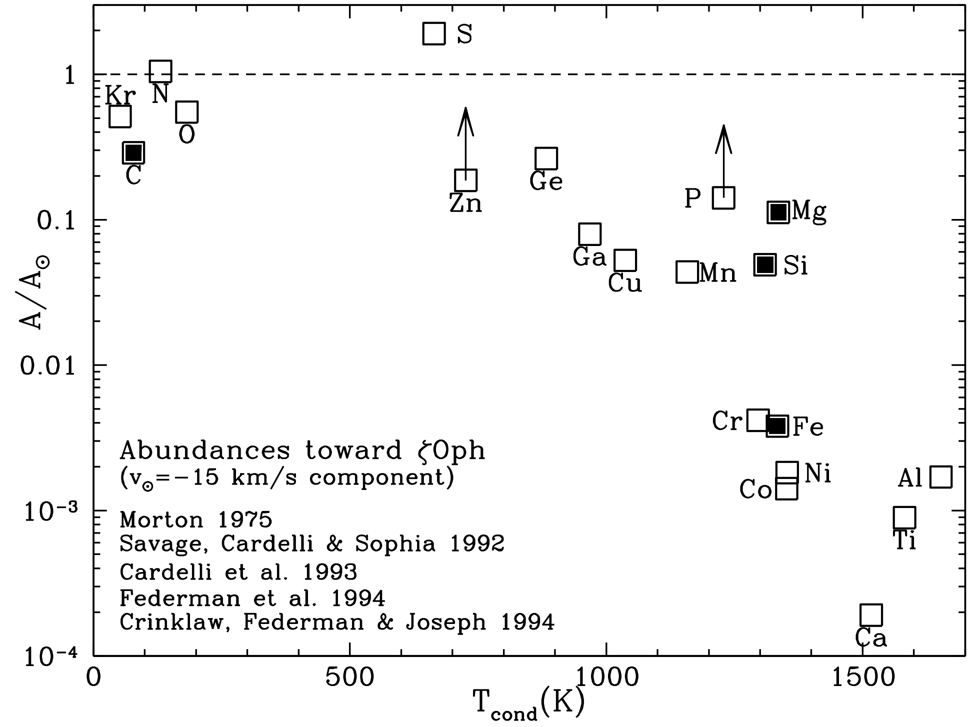

Figure 1.2: Gas phase abundances with respect to H in a sight-line towards ζ Oph plotted against the condensation temperature T_{cond}. The solid symbols represent elements that make up a large amount of dust grains: C, Mg, Si, Fe. The overabundance of S seen here is suggestive of either an observational error or due to SII absorption. Draine (2011).

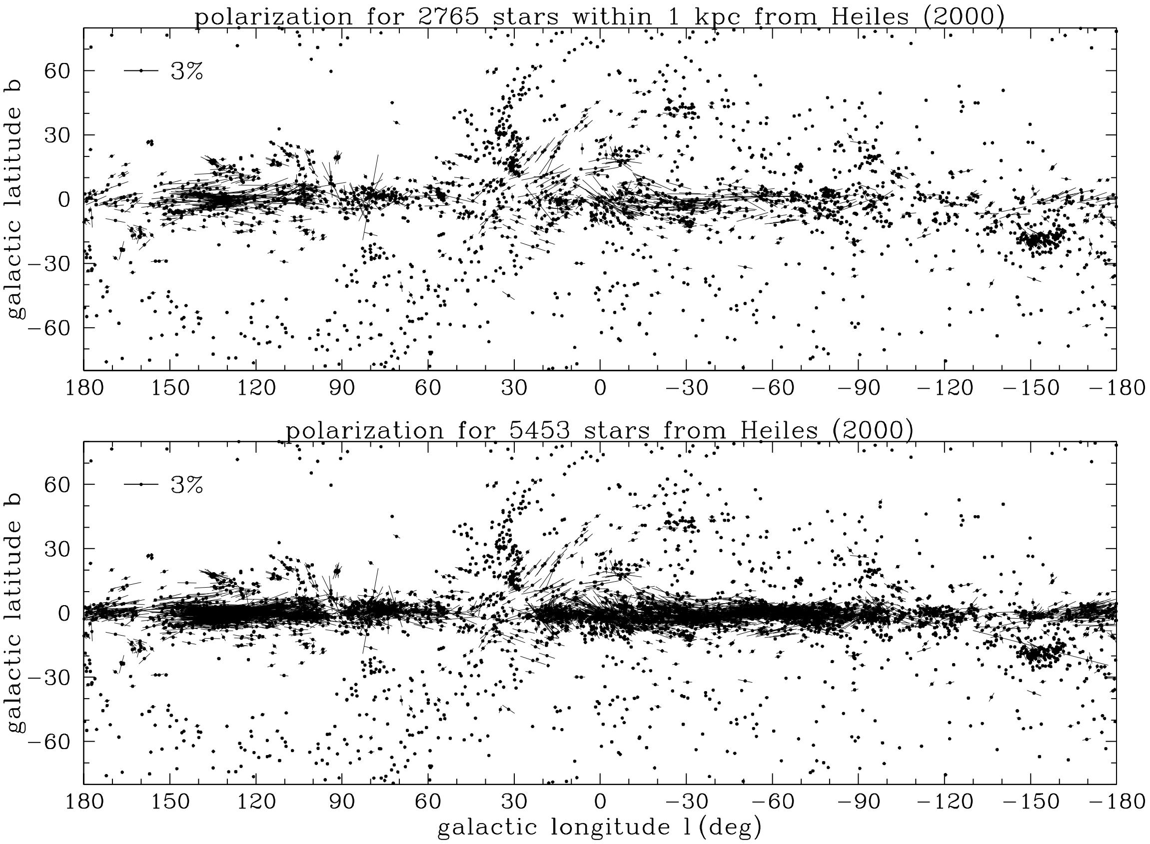

Figure 1.3: Polarization of starlight in galactic coordinates. Top: polarization for stars within 1 Kpc in Heiles (2000). Bottom: polarization of all stars in Heiles (2000). Image taken from Draine (2011).

tion, $p_{max} = p(\lambda_{max})$, varies between sources.

1.2. Dust in the ISM

1.2.1. Composition of ISM Dust

From Figure 1.2, elements with higher condensation temperature are more depleted. This depleted material is assumed to be in the solid phase and incorporated into dust grains. Considering this depletion, the amount of mass available for each element, and the chemical networks conducive to dust formation, dust grains are widely composed of C, Si, O, Mg, Fe and trace amounts of heavier elements. Common probable species of dust grains include silicates ($\mathrm{Mg}_x\mathrm{Fe}_{1-x}\mathrm{O}_3$ or $\mathrm{Mg}_{2x}\mathrm{Fe}_{2-2x}\mathrm{O}_4$), oxides ($\mathrm{SiO}_2$, MgO, $\mathrm{Fe}_3\mathrm{O}_4$), solid Fe, carbon (graphite or amorphous), carbides (SiC or TiC), and hydrocarbons such as polycyclic aromatic hydrocarbons (PAHs). Additional metals, Ti, V, Cr can exist in their solid phase, but make up a small percent of dust grains.

The features in the extinction curve give clues to the material responsible. Draine (1989) show the 2175 Å extinction feature could arise from H, C, N, O, Mg, Si, S, Fe grains, but is most likely from small C-bonded sheets due to a strong sp^2 transition around 2175 Å. The feature at 3.4 µm could also be due to carbonous material. The feature lines up with the C-H stretching mode in hydrocarbons. This feature is weaker in denser molecular clouds possibly due to destruction from cosmic radiation.

Silicates are also good candidates for these features. The 9.7 µm feature lines up with the stretching mode of Si-O around 10 µm. The 9.7 µm is seen in oxygen star outflows, but not in carbon stars where Si does not form. Another feature at 18 µm feature could be Si, the Si-O-Si bending mode of amorphous Si is near 18 µm.

1.2.2. The Size Distribution of ISM Dust

Multiple groups have attempted to produced a model of the size distribution of interstellar dust that agrees with observations. Mathis et al. (1977) looked at interstellar extinction between 0.11 µm $< \lambda <$1 µm. Using a combination of homogeneous spherical grains of uncoated graphite, enstatite $\mathrm{MgSiO_3}$, olivine $\mathrm{(Mg, Fe)_2SiO_4}$, silicon carbide SiC, iron Fe, and magnetite $\mathrm{Fe_3O_4}$, Mathis et al. (1977) fit different amounts of each substance. Mathis et al. (1977) found a power-law distribution fit well,

$$\frac{dn}{da} \propto a^{-l} \tag{1.5}$$

where n is the number of grains of size a, in the range $a_{min} < a < a_{max}$, and l is a constant. A value of $l = -3.3$ to $l = -3.6$ produced good fits with the data. Graphite was found to be essential to producing a good fit especially of the 2175 Å feature. The Si absorption feature at 10 µm was also reproduced. Sizes of graphite 0.005 µm to 1 µm and other species of 0.025 µm to 0.25 µm were found to be in agreement with observations. A value of $l = -3.5$ is colloquially accepted for this model's exponent, the MRN size distribution.

Further studies and observational data have shown issues with this model. Observations of extinction vary and depend on the ISM sight-line (Cardelli et al., 1989). Kim et al. (1994) show that for $R_V = 5.3$, the size distribution has fewer small, a <0.1 µm, grains than for $R_V = 3.1$. There is less extinction at shorter wavelengths in $R_V = 5.3$. Desert et al. (1990) point out the need to include PAHs, a population of large silicates, and small carbon grains in order to match observed emission in the infrared. Weingartner & Draine (2001), Zubko et al. (2004), and Draine & Fraisse (2009) show the extinction can be reproduced using a mixture of silicates, graphite, and PAHs using size distributions shown in Figure 1.4.

Weingartner & Draine (2001) fit the extinction well, but the dust mass used is greater than those dust masses indicated by elemental abundances and observed depletion. Zubko et al. (2004) use

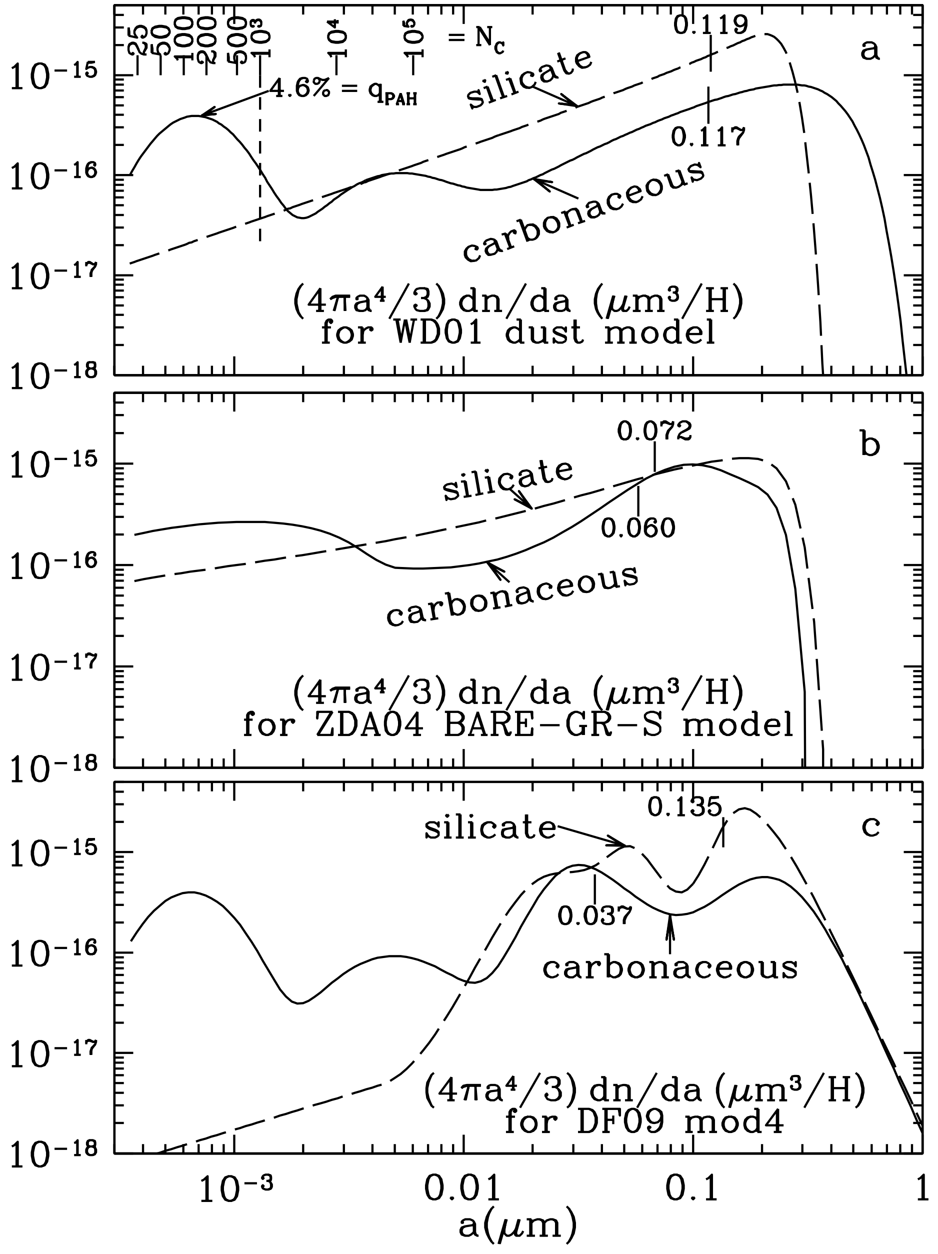

Figure 1.4: Size distributions of silicate and carbon grains from a) Weingartner & Draine (2001) b) Zubko et al. (2004) and c) Draine & Fraisse (2009). The y-axis is the grain volume per H per logarithmic interval in a Draine (2011). Image taken from Draine (2011).

fewer large grains, $a > 0.2$ µm, resulting in a poor fit of the infrared extinction. Draine & Fraisse (2009) use non-spherical dust grains to more accurately reproduce the extinction and polarization. However, this model uses significantly more Si than what is available. Determining the exact size distribution of interstellar dust remains challenging.

1.2.3. Gas-Surface Reactions: Grain Growth in the ISM

The low densities and thermal velocities of gases and molecules in the ISM significantly reduce molecular collisional frequencies and molecular binding, limiting the formation of new and complex molecules. Dust solves this issue, acting as a catalyst for new and complicated molecular formation. Dust absorbs the thermal energy of gas-phase species, binding the gas to its surface.

The rate of adsorption is given by,

$$k_{abs}(i) = \sigma_d v(i) n_i n_d \tag{1.6}$$

where σ_d is the cross-section of the dust grain, $v(i)$ is the thermal velocity of the gas species i, n_i is the number density of species i, and n_d is the number density of dust grains.

After adsorption, precursor molecules diffuse across the grain's surface through thermal or non-thermal diffusion. Upon encountering a complementary molecule, they react to synthesize a new molecular species. This process is essential in the formation of molecules such as H_2, H_2O, complex organic molecules (COMs), and polycyclic aromatic hydrocarbons (PAHs). These molecules are desorbed from the grain's surface by cosmic rays, secondary UV photons induced by cosmic ray-H_2 interactions, and far ultraviolet interstellar photons.

The rate of desorption is given by,

$$k_{des}(i) = \sqrt{\frac{2n_s E_D(i)}{\pi^2 m(i)}} \exp^{-\frac{E_D(i)}{T_g}} \tag{1.7}$$

where n_s is the surface density of sites, $E_D(i)$ is the desorption energy of species i, $m(i)$ is the mass of species i, and T_g is the temperature of the grain.

1.2.3.1. Thermal Diffusion

The process by which adsorbed species diffuse thermally across a grain's surface is through thermal hopping. This occurs when a species crosses over a potential barrier. The time for an adsorbed species to thermal hop is,

$$t_{hop} = \sqrt{\frac{2n_s E_D(i)}{\pi^2 m(i)}}^{-1} \exp\left(\frac{E_b}{T_g}\right) \tag{1.8}$$

where n_s is the surface density of sites, $E_D(i)$ is the desorption energy of species i, $m(i)$ is the mass of species i, E_b is the energy barrier between two sites, and T_g is the temperature of the grain. The square root term is the characteristic vibrational frequency for species i (Reboussin et al., 2014).

From equation 1.8, it is apparent thermal hopping is more efficient at higher temperatures and in absorped species with a low binding energy (Reboussin et al., 2014). However, sufficient energy is necessary to overcome the energy barrier between two sites.

1.2.3.2. Non-Thermal Diffusion

For some species, particularly light species, the energy needed to overcome energy barriers is significant. Penetrating a potential barrier becomes more efficient through quantum tunneling. The time for tunneling is given by,

$$t_{qt} = \sqrt{\frac{2n_s E_D(i)}{\pi^2 m(i)}}^{-1} \exp\left(\frac{2a}{\hbar}\sqrt{2mE_b}\right) \tag{1.9}$$

where a is the barrier thickness in angstroms (Reboussin et al., 2014).

Quantum tunneling depends on the mass of species i. Lighter species undergo quantum tunneling faster than more massive species. For example, for the diffusion of H, with a barrier energy E_b=225K, across a grain of radius 1 µm, takes $\sim 1.3\times10^{-4}$s for quantum tunneling and $\sim$1.7×10^3s for thermal hopping. Quantum tunneling is only efficient for light species such as H and H_2 (Reboussin et al., 2014). Minissale et al. (2013) show that quantum tunneling of heavier species may only be effective for O up to 20 K. Goumans & Andersson (2010) show the reaction rate of O+CO is faster with quantum tunneling between 10 K-20 K.

1.3. Stellar Sources of Dust

In the ISM are molecular clouds, a dense region composed of gas and dust. The kinetic energy of the gas particles within the cloud counteract and support the cloud against the internal force of gravity. If gravity exceeds the supporting forces, commonly through a compression of the cloud by shock waves, collapse begins, forming a proto-star. As the proto-star collapses, the temperature and density increase within the core, starting nuclear fusion. Hydrogen fuses into Helium and releases nuclear energy, the star enters the main sequence stage. This stage is characterized by hydrostatic equilibrium; fusion releases nuclear energy, creating an outward radiation pressure from the released nuclear energy and balancing the inward gravitational pressure. During this phase, exothermic reactions fuse lighter elements into heavier elements, increasing the core temperature while also releasing nuclear energy.

Continued fusion depends on the initial mass of the star. For stars with masses less than eight times the mass of the sun, $M_\odot$, nuclear fusion continues in the core up to carbon. The carbon core contracts until it is supported by electron degeneracy pressure. Hydrogen and Helium shell burning produces thermal instabilities and pulses. This causes the outer layers to be expelled in a planetary nebulae, leaving the compact core, a white dwarf (WD) star behind.

For massive stars ($M > 8\ M_\odot$), as fusion material is depleted in the core, fusion of a heavier species begins, leaving an outer layer of the depleted species. As heavier fusion reactions occur, an onion-like structure of elemental layers is built up until iron is produced in the core.

Iron has the lowest nuclear binding energy. Iron fusion is an endothermic reaction, energy is absorbed rather than released. As stars fuse up to iron, the core no longer produces an outward pressure from fusion and gravitational collapse begins.

During collapse, densities reach nuclear levels, causing protons and electrons to undergo inverse beta decay, combining into neutrons and producing neutrinos. The core is compressed into a neutron-rich core forming a proto-neutron star (PNS). Neutron degeneracy prevents further collapse. Infalling material rebounds off the PNS, generating an outward propagating shockwave.

This shockwave quickly stalls as it loses energy colliding with infalling material in the outer regions of the star. The neutrinos produced in the core escape, interacting with the surrounding material and depositing energy behind the stalled shock, reigniting the shock as it propagates outward. As the shockwave breaks out of the outer layers of the star, an explosion occurs: a Core-Collapse Supernova. In the ejected outflow, neutron capture generates elements heavier than iron. As the material expands, it is injected into the ISM, enriching and increasing its metallicity.

The evolutionary paths of low- and high-mass stars are shown in Figure 1.5.

1.3.1. Dust in AGB Stars

In the cool extended outer atmospheres of AGB stars, temperatures and densities reach those to molecular formation and dust grain nucleation. Convection cells, reaching into the stellar interior, bring newly formed elements to the surface. Unstable stars undergo pulsations, triggering a shock wave that lifts gas above the stellar surface, creating cool layers. In these regions, molecules may form and eventually nucleate into dust grains. Several mechanisms can then carry these grains out of the stellar envelope and into the circumstellar envelope (CSM). Radiation pressure from the star exerts force on dust grains, pushing the grains out and into the CSM. Smaller dust grains are more affected by this process due to their reduced mass. In high gas density regions, gas-dust collisions transfer momentum from the gas to the dust, accelerating it out of the stellar envelope. Line-driven winds are caused from the interaction between photons emitted by the star and the spectral lines within the stellar atmosphere. This interaction transfers momentum to the surrounding gas, which is accelerated outwards. As the gas moves, it carries the dust with it, resulting in a stellar wind. AGB mass loss from these processes can range from $10^{-8}\ M_\odot$/yr to $10^{-1}\ M_\odot$/yr and periodic

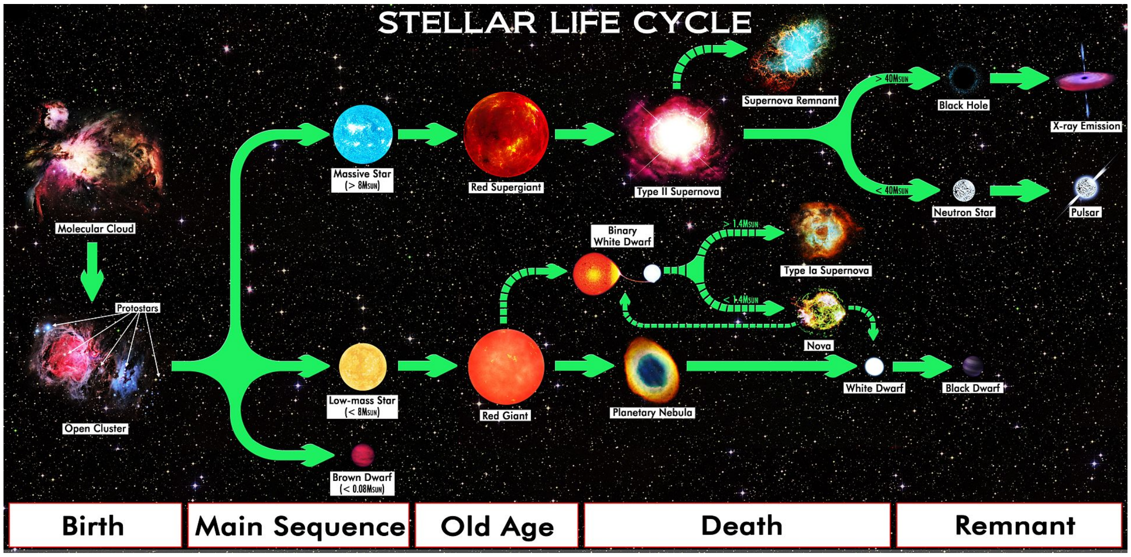

Figure 1.5: A diagram showing the stages of stellar evolution based on the progenitor mass. Image taken from Bailey (2024).

pulsations of the star can trigger episodes of increased mass loss.

1.3.2. Dust in Core-Collapse Supernovae

As the ejecta expands and cools in CCSNe, dust grains condense and nucleate in the ejecta. This newly formed dust is vulnerable to erosion from the surrounding medium. Due to the Maxwell-Boltzmann distribution of the surrounding gases' velocities, gas is constantly colliding with the dust. With high enough energies, the gas transfers energy to the grain, overcoming surface binding energies and sputtering off material. This process is called thermal sputtering. In CCSNe, it occurs at lower energies where the dust is moving along with the gas. When dust collides with gas, such as an impact with shocked material, non-thermal sputtering ejects material from the grain.

The amount of dust that survives the CCSN and is injected into the ISM depends on several factors. Higher gas temperatures cause more thermal sputtering. Strong shock velocities cause more material to break off. However, in both cases, after a maximum gas temperature and shock velocity, the impacting gas interacts more weakly with the grain, causing less erosion.

The amount of dust produced and survives the reverse shock is not well constrained. Results vary based on the assumptions of clumpiness in the ejecta, the strength of the reverse shock, the model used to produce dust, the initial size distribution of produced grains, the relative abundances of the progenitor, the equation of state of the expanding ejecta, and additional physics such as heating from radioactive decay and Compton scattering.

1.4. Additional Sources of Dust

1.4.1. AGN

Active Galactic Nuclei (AGN) consist of a supermassive black hole surrounded by an accretion disk with relativistic jets emanating from the black hole's poles, all encased in a toroid of gas and dust (Antonucci, 1993). These objects are among the most luminous in the universe. Most of the gas appears to be photoionized not by stars, but by radiation emitted by the surrounding accretion disk or by a magnetic field induced by the black hole. Some regions in the AGN exhibit high particle and energy densities.

Observations in the infrared show the surrounding toroid is dusty. The origin of the dust is not known, but the presence of the 9.7 and 18 μm spectral features in AGN winds are characteristic of Si-O bonds in dust condensation (Shi et al., 2006). This suggests dust forms within the winds of AGNs. Czerny & Hryniewicz (2011); Baskin & Laor (2017) suggest dusty winds from the outer accretion disk is captured in the region between the accretion disk and dusty torus. Elvis et al. (2002) discuss how the expansion of clouds producing broad emission lines, the area between the accretion disk and dusty torus, produce conditions resulting in the formation of dust grains.

1.4.2. Dust in Mass Loss Events

Dust formation occurs during stellar mass loss, particularly around giant, supergiant, and evolved stars. These stars expel mass through stellar winds rich in heavier elements into the surrounding circumstellar medium. In these cooler regions, dust grains nucleate and grow. Among these, Wolf-Rayet stars, which are evolved, massive, and luminous, generate intense stellar winds that strip away significant amounts of enriched material. Dust grains form from this ejected material in cooler regions around the star.

In binary systems with a White Dwarf (WD), an evolved compact star that has shed its outer layers, the WD accretes material from its companion star. This accretion continues until the WD approaches the Chandrasekhar mass limit, igniting a runaway fusion reaction resulting in a Type Ia Supernova explosion. Dust forms in the cool, expanding ejecta of these explosions.

Luminous Blue Variables (LBVs), massive and eruptive O and B type stars, also contribute to dust formation. During periods of enhanced mass loss, thick circumstellar material accumulate around LBVs. Within these dense layers, large dust clumps are formed.

1.5. Dust Nucleation Models

Nucleation is the formation of a new thermodynamic phase and growth through the attachment of additional particles (Karthika et al., 2016), the process results in a new dust grain. Thermal fluctuations drive these phase changes. Homogeneous nucleation occurs when thermal fluctuations in a stable thermal system in equilibrium causes metastability, an intermediate state other than the lowest energy state. Impurities in the source material can act as surface catalysts for phase transitions called heterogeneous nucleation. This allows for nucleation to occur at lower supersaturation than in homogeneous nucleation. Multiple theories describing nucleation are discussed below.

1.5.1. Classical Nucleation Theory (CNT)

Classical Nucleation Theory tracks the condensation of a vapor to a liquid in homogeneous mediums (Volmer & Weber, 1926; Becker & Döring, 1935; Frenkel, 1939). The formation of the new phase is influenced by the volumetric free-energy gain from the formation of the new phase and the surface free-energy cost due to the creation of the new interfaces. A diagram showing these energies is shown in Figure 1.6. The change in free energy during the nucleation of a spherical particle of radius r is,

$$\Delta G = -\frac{4\pi r^4}{3V} kT \ln(S) + 4\pi r^2 \sigma \tag{1.10}$$

where V is the volume of one molecule, k is the Boltzmann constant, T is the temperature, S is the vapor supersaturation ratio, and σ is the surface energy of interface between the vapor and the droplet (Volmer & Weber, 1926). When ΔG is at a maximum, the critical size (the size at which nucleation occurs) is given by,

$$r_{crit} = \frac{2\sigma}{kT \ln(S)} \tag{1.11}$$

a nucleus of this critical size is in metastable equilibrium with the vapor. Adding more molecules decreases the free energy making further growth energetically favorable, leading to spontaneous growth. The rate of these nuclei, the nucleation rate is given by the Arrhenius equation,

$$J = A \exp\left[-\frac{\Delta G_{crit}}{kT}\right] \tag{1.12}$$

where ΔG_{crit} is the change in Gibbs free energy with the formation of a nucleus of size r_{crit}, and A is the exponential coefficient in the Arrhenius equation accounting for molecular collisional frequency.

CNT makes several simplifying assumptions. It assumes nucleated grains are spherical. This is not true for NaCl which is square (Karthika et al., 2016). CNT assumes the nucleus and the stable phase share the same properties. It assumes the capillary approximation, where the vapor-liquid interface is treated as planar. However, for smaller clusters, the interface is curved. These assumptions cause discrepancies when compared to real data and breaks down in some systems.

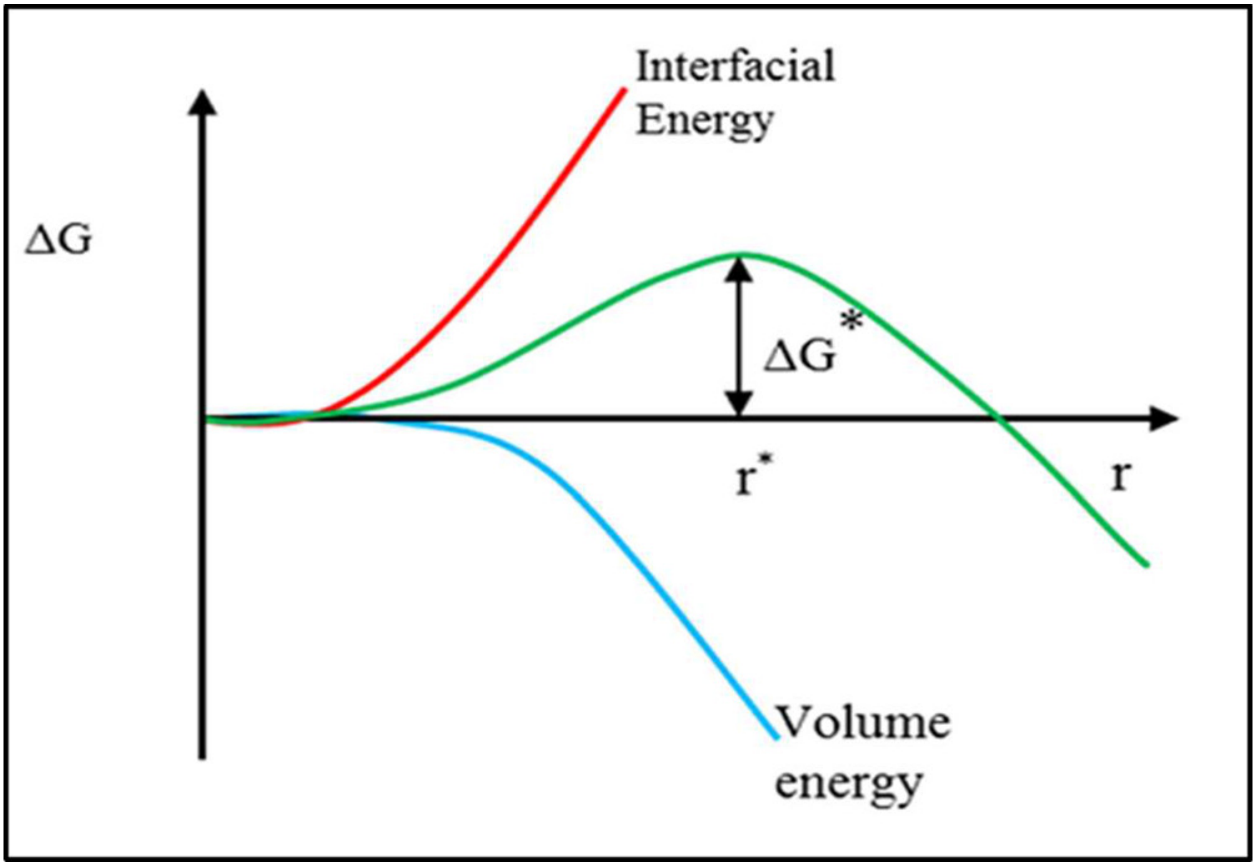

Figure 1.6: Diagram of the nucleation barrier ΔG as a function of nucleus radius. Image taken from Karthika et al. (2016).

1.5.2. Non-Classical Nucleation Theory

Density Functional Theory, also referred to as non-classical nucleation theory, is a first principle approach to nucleation based on microscopic molecular interactions that deviates from the capillary approximation of CNT. In DFT, the free energy is treated as a function of the molecular density. It assumes the free energy of the nucleus depends on the average spherical density profile, on a density functional (Karthika et al., 2016; Zeng & Oxtoby, 1991). DFT does not assume the nucleus has the same properties as the bulk of the new phase. The critical nucleus in DFT is the saddle between the vapor and liquid phase, a local maximum in the free energy, it is the point where growth in the new phase, nucleation, is favored (Zeng & Oxtoby, 1991). The nucleation rate of DFT shares the same form and exponential coefficient as in CNT (Nyquist et al., 1995), but with a different energy,

$$J_{DFT} = A \exp\left[-\frac{\Omega_{DFT}}{kT}\right] \tag{1.13}$$

where Ω_{DFT} is the free energy determined through density functional methods. The free energy is calculated from the attractive and repulsive spherical potentials describing the interactions between molecules.

1.6. Thesis Outline

Despite its importance, the mechanisms responsible for dust production, their efficacy, and the influences of the surrounding environment are poorly understood. Existing models yield varying quantities and compositions of the dust produced. These models do not account for the presence of massive grains observed in molecular clouds. The significance of dust is shown by its impact on observations, molecular evolution, and the formation and evolution of astronomical systems. Further research into dust dynamics and its origins provides an essential understanding of astrophysics.

This thesis is arranged as follows: Dust formation is discussed in Chapter 2. I setup and ran the 1-D hydrodynamical codes on half the models in Brooker et al. (2022). I refined a nucleating dust code, `nudust` (Brooker et al., 2021; Mauney & Stangl, 2022), and post processed dust formation on the models. I analyzed data and wrote part of the background in Brooker et al. (2022). The development and release of the most recent version of `nudustc++`, a nucleating dust code now including destruction, is discussed in Chapter 3. I rewrote `nudust` in `C++` starting from `starchem` (Christopher Mauney, 2017) and added dust nucleation and destruction. Dust destruction and survivability are discussed in Chapter 4. I restarted the hydrodynamical simulations on all the models in Brooker et al. (2022)until the SN shock hit the outer boundary and sent a reverse shock through the whole SN ejecta. I ran the `nudustc++` with destruction on the CCSNe models, analyzed the data, and wrote the second paper (in preparation) in the Brooker et al. (2022) series. The optical properties of dust and their modeling are discussed in Chapter 5. I wrote a Mie scattering code, `mie_scat`, in Fortran to study the contributions of dust to opacity. Observational work is discussed in Chapter 6. I compiled light curve data, detected variability, and generated plots of variable stars in Humphreys et al. (2019a). As a member of Poise (Burns et al., 2021), I provided insight into dust dynamics. Conclusion, implications, and future work are discussed in Chapter 7.

CHAPTER 2

Dust Grain Formation & Nucleation

Original Manuscript from:
Brooker et al. (2022)
Dependence of Dust Formation on the Supernova Explosion
The Astrophysical Journal, 931:85 (25pp), 2022 June 1

2.1. Abstract

We investigate the properties, composition, and dynamics of dust formation and growth for a diverse set of core-collapse supernovae (CCSNe), with 15, 20, and 25 $M_\odot$ progenitor masses, explosion energies ranging from 0.5 to 120 foe, and varied engine type. These explosions are evolved with a 1-D Lagrangian hydrodynamics code out to a minimum of 1157 days to model the ejecta as it expands and cools. A multigrain dust nucleation and growth model is applied to these results. We find that higher explosion energies lead to an earlier onset of dust formation, smaller grain sizes, and larger silicate abundances. Further, we see that nuclear burning during the explosion leads to enhanced formation of silicate dust. Finally, we build composite models from our suite to predict the efficiency of CCSNe dust production as a function of metallicity.

2.2. Introduction

Dust is ubiquitous in the interstellar medium (ISM) of most galaxies, typically in the form of carbonaceous or silicate cores with a mantle of accumulated ices. A vital component of stellar and galactic life cycles, understanding the formation of dust in different galactic environments is key to understanding the evolution of those host galaxies. Dust cools and insulates collapsing molecular clouds, allowing for more efficient star formation. Heavy elements are locked into dust grains, depleting the gas phase of these elements. In the ISM the dust grains provide a site for the formation of H_2O and other complex molecules through diffusion on the surface (Draine, 2003).

Of the many theoretical explorations of astrophysics, the transformation of stellar vapor to interstellar molecular fog is shrouded in conjecture and guesswork. While there is a substantial body of work that covers the terrestrial phenomenon, the formation, growth, and evolution of large molecular particles in the near vacuum of the environment remain a subject of intense conjecture in the stellar and galactic background. We seek to understand the dynamics of timescales and distance scales over several magnitudes ranging from the chemical reactions at the molecular scale to dynamical reactions at the stellar scale, and then back again. The scope of this study is difficult to simply encompass.

There have been several attempts at answering this extremely difficult question. Dust formation and processing have been observed in stellar winds, core-collapse supernovae (CCSNe), and the atmospheres of AGB stars. Dust from Type Ia SNe has also been suggested as a significant contributor (Gomez et al., 2012). There are also several investigations into the cold formation and growth of dust in molecular clouds (Marin et al., 2020; Mattsson, 2020). The prime producer of galactic dust must have changed over time, as galaxies at high z lack late-age producers of dust in the local galactic environment such as AGB stars and Type Ia SNe. If dust formed in the outflows of CCSNe is a significant source of ISM dust, then production in low metallicity galaxies of the early universe is likely to be dominated by CCSNe (Sadavoy et al., 2019).

Observations of local CCSNe such as 1987A (Dwek & Arendt, 2015; Wesson et al., 2015) and Cassiopeia A (Arendt et al., 2014; Priestley et al., 2019), show abundant dust masses in CCSNe ejecta prior to interacting with the ISM. Heating from post-explosion shocks will disrupt grain formation and growth, and it is argued that this will prevent any significant portion of dust grains formed in the outflow from surviving long enough to reach into the ISM (Bocchio et al., 2016). However, dust material has been seen to survive and reform after the passing of forward shocks in the ejecta of 1987A (Matsuura et al., 2019). Large dust grains capable of surviving shock destruction have been seen in abundance in SN 2010jl (Gall et al., 2014) Models of dust formation across cosmic time complicate this picture further, with an epoch of formation in stellar ejecta at $z < 2$, later overtaken by growth in the ISM as the main channel of dust production up to the present (Triani et al., 2020).

The explosion energy, explosive engine, metallicity, and progenitor mass of the CCSN will all impact the subsequent dust formation history and composition (Müller et al., 2016). Observations of the SN ejecta probe the detailed composition of the ejecta, which, in turn, can be used to probe the properties of the progenitor star and the process of the explosion. After shock breakout, the outflow expands and cools with ionized plasma recombining into the gas phase. Gas-phase reactions occur and change the initial abundance of free gas phase species into a rich mixture of compounds (Sluder et al., 2018). At densities and temperatures starting at roughly 5000 K, condensation nuclei (refractory dust grains) form from the free species available in the mixture. These dust grains can be spectrally observed, serving as a probe for nucleosynthetic yields and morphological tracers related to the explosion inside of the star.

Dust yields from progenitors with different masses and metallicities are still under active study. Understanding how CCSNe produce different dust properties and compositions can inform astrophysicists about stellar and galactic evolution. Dust formation studies of a limited number of CCSN progenitor configurations have previously been undertaken covering various contexts. For example, studies have been done of Population III stars (Nozawa & Kozasa, 2013) and the effects of metallicity and stellar rotation (Marassi et al., 2019). Molecule and dust precursor evolution across stellar masses was investigated in Sarangi & Cherchneff (2013). This work also used ^{56}Ni as a proxy for looking through explosion energies.

In this work, we extend these previous results to include profiles and yields from high-fidelity CCSNe simulations as our starting point for hydrodynamic and dust formation evolution. This suite of CCNSe includes yields of elements formed during the collapse and bounce phase of the explosion, offering more precise initial conditions. We also use active hydrodynamics to generate a more realistic temperature and density background, as well as to incorporate the thermal and compression effects of shocks arising from the explosion.

This paper is constructed as follows. In Section 2.3, we describe how our CCSNe models are constructed, as well as the dust model we use. Section 2.4 describes our results, including the distribution of dust in the ejecta; the composition, mass, and size of dust grains; and a comparison of different progenitor types. Finally, in Section 2.5 we discuss our conclusions, make comparisons to previous studies (see Table 2.2), and suggest observational applications.

2.3. Methods

Chemical activity in the ejecta environment is controlled by composition, temperature, and pressure. Our entry point into modeling this environment is an initial 1D profile of a CCSNe immediately prior to shock breakout. We proceed to map these profiles onto an extended 1D grid stretching out to a presumed terminus at the ISM, and append a stellar wind from the star's surface to the boundary. The exploding star plus wind system is then hydrodynamically evolved out to several years, enough time that all nucleation activity will cease. Using the density and temperature trajectories of these simulations, we then calculate the dust nucleation and growth histories for each grid cell.

2.3.1. Core-Collapse Supernova Models

To model dust in CCSN ejecta, we utilized a suite of 1D CCSN explosion models from Fryer et al. (2018); Andrews et al. (2020) covering a range of explosion energies ($10^{51} - 10^{53}$ erg), progenitor star masses (15, 20, and 25 $M_{\odot}$), and nucleosynthetic isotopic yields. These calculations used a one dimensional CCSN code (Herant et al., 1994; Fryer et al., 1999), referred to as FR99 hereafter, which includes a gray flux-limited diffusion scheme following three-neutrino flavors (electron, anti-electron, and μ plus τ neutrinos), a blend of equations of state to cover nuclear densities down to an ideal gas equation of state for low densities. Nuclear burning is included using a nuclear statistical equilibrium treatment at high temperatures and a small 17-isotope network at lower temperatures. Explosions are driven by injecting additional energy mixed into a predetermined convective region.

The total energy and nature of this injection (sudden energy source as expected from the convective engine vs. a prolonged source produced by a magnetar or fallback accretion) are varied to produce a broad range of explosion properties. The suite of progenitor masses and explosion energies is listed in Table A.1 in Appendix A.1 with model name designations given. We provide the complete list of isotopes in the supernova simulation data in Table A.2 in Appendix A.1. The velocity and composition of the ejecta depend both on the progenitor mass and its explosion energy. Figure 2.1 shows an example of the initial compositions of two 15, 20, and 25 $M_{\odot}$ progenitor models.

2.3.2. Late-Time Evolution

To follow the explosion to late times, we remove the compact core from our simulation and place the outflow onto a mesh extending out to 2.5×10^{19} cm. Starting from the surface of the star, we add a wind profile. The winds for our different progenitors use the formulation from Villata (1992) for a wind profile

$$\dot{M}_{wind} = 1.2 \left(\frac{D^{\delta} \dot{M}_{\alpha}^{CAK}}{1+\alpha} \right)^{1/(\alpha-\delta)} \tag{2.1}$$

where D and $\dot{M}_{CAK}$ are

$$\begin{aligned} D &= \left(\frac{1 + Z_{He} Y_{He}}{1 + 4Y_{He}} \right) \left(\frac{9.5 \times 10^{-11}}{\pi m_H R_*^2 v_\infty} \right) \\ \dot{M}_{CAK} &= \frac{4\pi G M_* \alpha}{\sigma_E v_{th}} \left[k\Gamma \left(\frac{1-\alpha}{1-\Gamma} \right)^{1-\alpha} \right] \end{aligned} \tag{2.2}$$

where Z_{He} is the free electrons from helium, Y_{He} is the helium number abundance with respect to H, m_H is the mass of hydrogen ion, σ_E is Thomson scattering absorption coefficient per mass density, $\Gamma = L/L_E$ is the ratio of stellar to Eddington luminosity, v_∞ is the escape velocity, v_{th} is thermal velocity, and k is a force multiplier. With a β velocity law

$$\begin{aligned} v(r) &= v_\infty \left(1 - \frac{r_0}{r} \right)^{\beta} \\ \beta &= 0.95\alpha + \frac{0.008}{\delta} + \frac{0.032 v_{esc}}{500} \end{aligned} \tag{2.3}$$

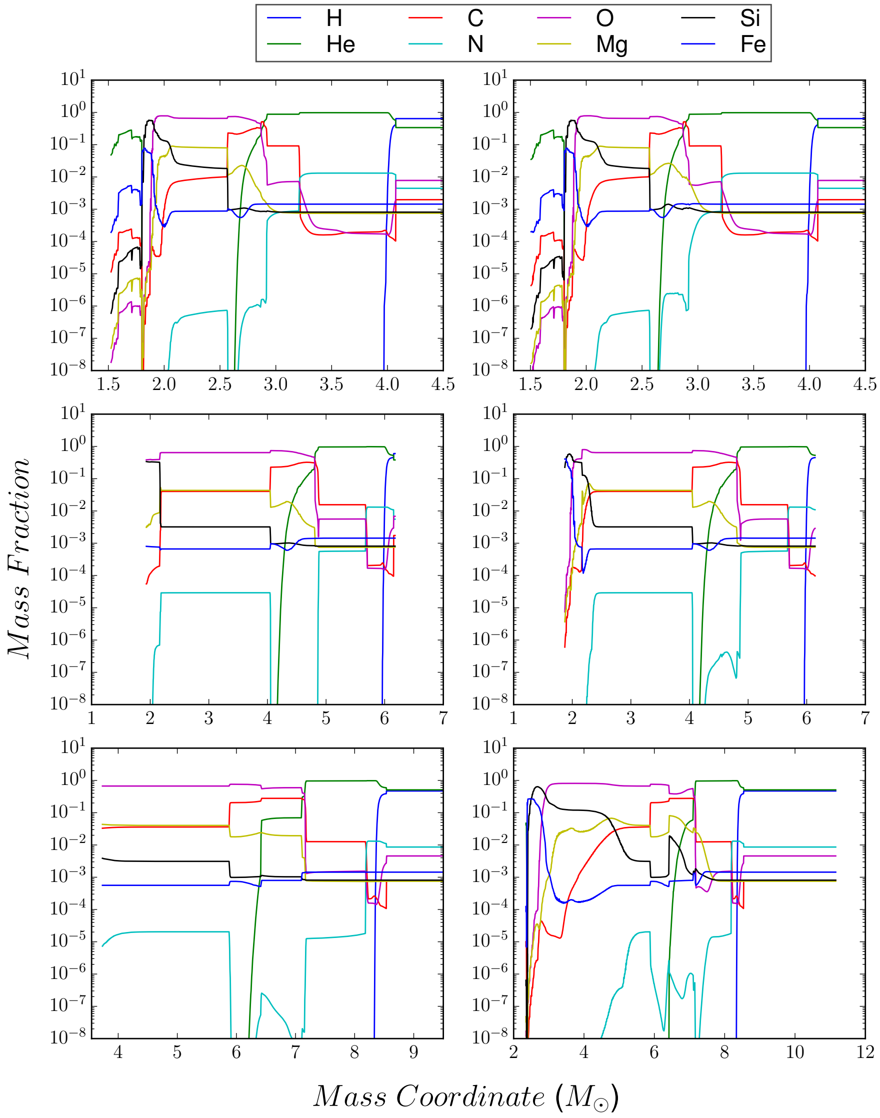

Figure 2.1: Above are plotted the abundance profiles for elements important in the formation of our selected grain species from dataset produced by Fryer et al. (2018) using Fryer et al. (1999). The top row is two 15 $M_\odot$ progenitor models (L: 1.69 Foe, R: 3.43 Foe explosion energies), the middle row is two 20 $M_\odot$ models (L: 1.39 Foe, R: 5.9 Foe), and the bottom row is two 25 $M_\odot$ models (L: 1.57 Foe, R: 14.8 Foe). Models with the same progenitor mass have similar initial abundance profiles. However, with varying explosion energies, the distribution of nitrogen and magnesium vary the largest. With very high differences in explosion energy, the higher energy model has less uniform structure as seen in the 25 $M_\odot$ models. The horizontal lines in the outer regions of the profiles are due to a stitched-on stellar wind.

where v_{esc} is the escape velocity, in km s^{-1}. For the wind parameters k, α, δ, we use the typical values: 0.17, 0.59, 0.09 respectively.

The corresponding density profile of the wind must include a transition from the stellar surface to the canonical r^{-2} profile expected in constant-velocity winds. With our wind velocity ($v(r)$) and mass-loss rate ($\dot{M}_{CAK}$), we can calculate the wind density assuming mass conservation:

$$\rho_{wind}(r) = \dot{M}_{CAK}/(4\pi r^2 v(r)) \tag{2.4}$$

We determine the specific energy by assuming a constant entropy wind profile. When the wind density drops below the ISM (we use a canonical value of $2.09 \times 10^{-24}\ g/cm^3$), the density is set to the ISM.

The subsequent late-time evolution is calculated by mapping the explosion from our core-collapse calculations into this wind density profile using a grid of 2048 Lagrangian zones. We then follow the explosion using a simplified version of our CCSN code (FR99, without neutrino transport or equations of state for dense matter).

Figure 2.2 shows the evolution of the velocity, temperature, and density profiles for a model with progenitor mass of 15 M$_\odot$ and explosion energy E_{exp} of 1.69 foe (designated M15bE1.69 in Table A.1) in Appendix A.1 at a range of times after the launch of the explosion. These calculations are typically evolved out to 1157 days. The jump in the density and temperature coincides with the shock front and is reasonably well fit by the strong shock solution (Landau & Lifshitz, 1959). As the shock propagates through the wind medium, we can see both the deceleration (comparing the velocity profiles at different times) and the subsequent reverse shock formed by this deceleration. Although we do not consider the destruction of grains from this reverse shock in this paper, our calculations provide the data to do so, and this will be studied in future work.

These calculations provide the density and temperature evolution with time for every zone (cell in the Lagrangian mesh) in the model. Figure 2.3 shows the density and temperature evolution for the zones in model M15bE1.69. With the abundances from our core-collapse models and the temperature and density trajectories from these late-time calculations, we have the full input for our dust formation models.

For simplicity, our hydrodynamics evolution does not include the effects of radioactive decay heat. We detail the potential effects of this in our discussions in Section 2.5.

2.3.3. Dust Formation

During the expansion, the ejecta material cools to conditions where the gas-phase pressure-temperature (p-T) state becomes thermodynamically *metastable*, and a phase transition is energetically favorable (Kashchiev, 2000). However, the material will last in a metastable state for an

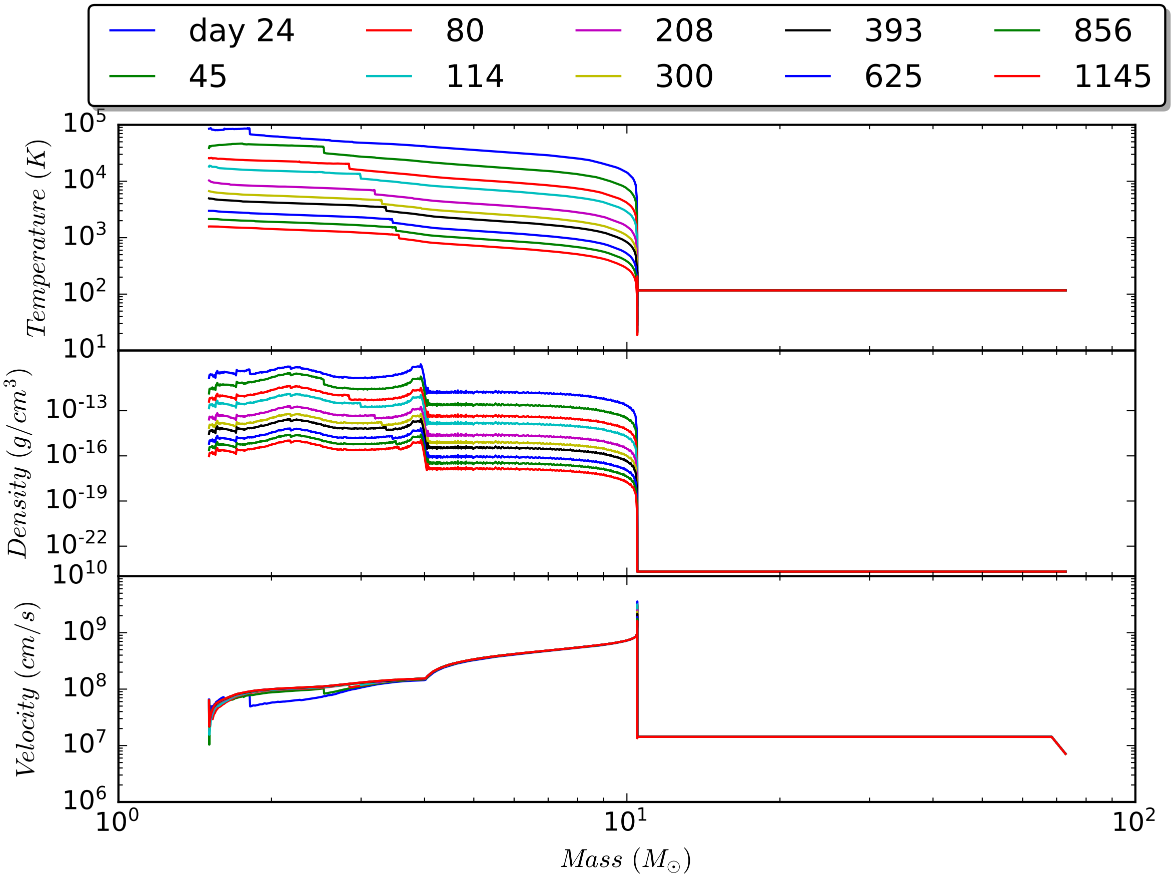

Figure 2.2: Top: temperature vs mass coordinate profiles for model M15bE1.69 at 24-1145 days after explosion. Middle: density vs mass coordinate profiles for the same model after explosion. Bottom: the velocity profile for the same model. An outward propagating shock can be seen at about 2.2-4 $M_\odot$ where the temperature and density drops off as you move out in the ejecta. The shock is most prominent in the temperature plot. The sudden drop off at about 10 $M_\odot$ indicates the interface between ejecta and the stellar wind.

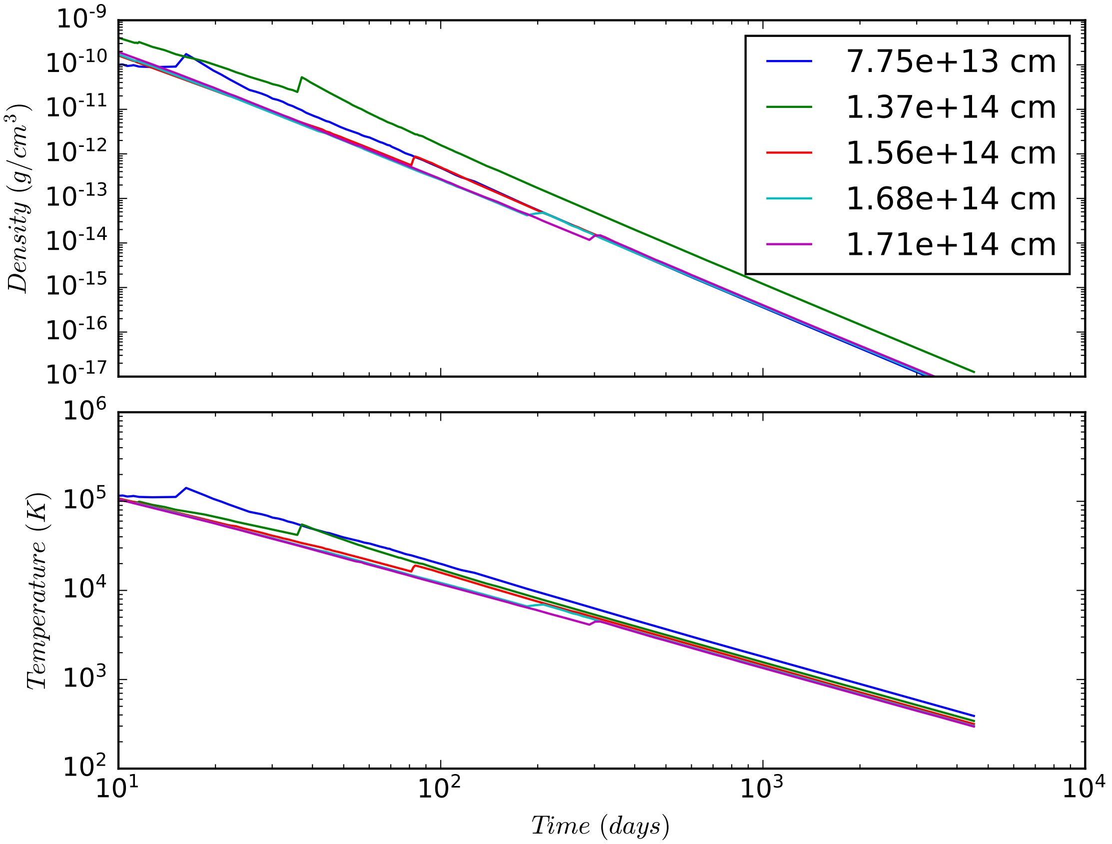

Figure 2.3: Top: The density as a function of time for various cells at different initial depths in the progenitor model M15bE1.69. Bottom: The temperature profile as a function of time for the same model and cells. A shock can be seen in all plots at about 20-300 days. It is characterized by an upwards almost vertical jump.

extended period owing to a kinetic energy barrier spanning the transient phase space. This tension is resolved through the mechanism of *nucleation*; molecules in the new phase may grow by Boltzmannic attachment and eventually form large *critical clusters* that are locally truly stable and provide a seed for spontaneous growth (Vehkamäki, 2006).

The formation of a molecular cluster of size n (n-mer) results in a decrease in free energy but introduces an interface between the phases that requires excess free energy to maintain (*surface tension*). Thus, the *driving force* of nucleation is the difference in free energy

$$\Delta G(n) = -G_V(n) + G_S(n) \tag{2.5}$$

While this formulation is straightforward, proceeding further becomes difficult. In particular, the energy required to maintain the interface is dependent on the chemical and geometric peculiarities of the molecular structure of the n-mer (Mauney et al., 2015). Kinetic nucleation theory (KNT) simplifies this state of affairs by assuming that clusters are treated as nanoscale portions of the bulk stable phase that form through attachment of monomers and minimize the free energy to maintain the interface by growing as dense spheres (the *capillary approximation*).

In KNT, the number densities of clusters c_n are explicitly tracked. At each time step, we simultaneously evolve the number densities of all component species in our nucleation reactions, and all dust products draw from the same pool of vapor material. That is, dust products are competing for the available abundances.

This approach to modeling dust formation has drawbacks. It does not include chemical reactions of forming the grain precursors. Surface tension properties of a solid bulk material are used. Our model also does not presently include coagulation or destruction. These drawbacks are currently being remedied for future work, see the discussions in Section 2.5.

We follow the revised formulation of KNT given in Appendix A of Nozawa & Kozasa (2013). This formulation has no explicit dependence on the standard pressure p_s, and incorporates the integrated kinetics of chemical reactions at the time of nucleation. Further, nucleation and growth are controlled by the abundance of the *key species*. The key species of a reaction is defined as the reactant with the lowest collisional frequency. In this reformulation, nucleation is represented as the reaction

$$Z_{n-1} + (X + \nu_1 \mathcal{A}_1 + \nu_2 \mathcal{A}_2 + \cdots + \nu_i \mathcal{A}_i) \longrightarrow Z_n + (\eta_1 \mathcal{B}_1 + \eta_2 \mathcal{B}_2 + \cdots + \eta_j \mathcal{B}_j) \tag{2.6}$$

where ν_k, η_k are the reactants/product stoichiometric coefficients, and $\mathcal{A}_k$, $\mathcal{B}_k$ are the reactant/product species, and X is the key species. In determination of reaction rates, the coefficient $\nu_{k,s}$ of the key species is taken as unity, and non-key-species coefficients ν_k, η_k are normalized to the key species.

The modified steady-state rate of this nucleation reaction Equation (2.6) is given by

$$J_s = \gamma \Omega_0 \sqrt{\frac{2\sigma}{\pi m_1}} c_1^2 \Pi \exp\left(-\frac{4}{27}\frac{\mu^3}{(\ln S)^2}\right) \tag{2.7}$$

where γ is a sticking probability (we assume $\gamma = 1$), $\Omega_0 = 4\pi a_0^3/3$ is the volume per key-species of the cluster, σ is the bulk-derived surface tension, m_1 is the mass of the attaching monomer, S is the *supersaturation ratio* (hereafter *saturation*), $\mu = 4\pi a_0^2\sigma/kT$, and Π is a correction factor defined as

$$\Pi = \left[\frac{\prod_{k=1}^{i}(c_k^{\mathcal{A}}/c_1)^{\nu_k}}{\prod_{k=1}^{j}(c_k^{\mathcal{B}}/c_1)^{\eta_k}}\right]^{\frac{1}{\omega}} \tag{2.8}$$

where c^A, c^B are the concentrations of reactants and products, respectively, c_1 is the key-species concentration in the vapor, and $w = 1 + \sum_{k=1}^{i}\nu_k - \sum_{k=1}^{j}\eta_k$. Values for parameters a_0, σ of each key species is given in Table 2.1. The details of the grain nucleation reactions are given in Table 2.1 and is taken directly from Nozawa et al. (2003). This table provides the dust grain name, the key species involved in the reaction to produce the grain, the reaction formula, and specific numerical parameters related to the free energy, grain surface tensions, and expected monomer size for grain nucleation equations we use to form dust grains.

Table 2.1. Dust grain reaction table taken from Nozawa et al. (2003).

Grain	Key Species	Formula	$A/10^4$(K)	B	$\sigma(\mathrm{erg}/\,\mathring{A}^2)$	$a_0(\,\mathring{A})$
C	C(g)	$\mathrm{C(g)} \rightarrow \mathrm{C}$	8.64726	19.0422	1400.0	1.281
SiC	Si(g), C(g)	$\mathrm{Si(g)} + \mathrm{C(g)} \rightarrow \mathrm{SiC}$	14.8934	37.3825	1800.0	1.702
TiC	Ti(g), C(g)	$\mathrm{Ti(g)} + \mathrm{C(g)} \rightarrow \mathrm{TiC}$	16.4696	37.2301	1242.0	1.689
Si	Si(g)	$\mathrm{Si(g)} \rightarrow \mathrm{Si}$	5.36975	17.4349	800.0	1.684
$\mathrm{MgSiO_3(s)}$	Mg(g), SiO(g)	$\mathrm{Mg(g)} + \mathrm{SiO(g)} + 2\mathrm{O(g)}$ $\rightarrow \mathrm{MgSiO_3(s)}$	25.0129	72.0015	400.0	2.319
$\mathrm{Mg_2SiO_4(s)}$	Mg(g)	$2\mathrm{Mg(g)} + \mathrm{SiO(g)} + 3\mathrm{O(g)}$ $\rightarrow \mathrm{Mg_2SiO_4(s)}$	18.6200	52.4336	436.0	2.055
$\mathrm{Mg_2SiO_4(s)}$	SiO(g)	$2\mathrm{Mg(g)} + \mathrm{SiO(g)} + 3\mathrm{O(g)}$ $\rightarrow \mathrm{Mg_2SiO_4(s)}$	37.2400	104.872	436.0	2.589
$\mathrm{SiO_2(s)}$	SiO(g)	$\mathrm{SiO(g)} + \mathrm{O(g)} \rightarrow \mathrm{SiO_2(s)}$	12.6028	38.1507	605.0	2.080
$\mathrm{Al_2O_3(s)}$	Al(g)	$2\mathrm{Al(g)} + 3\mathrm{O(g)} \rightarrow \mathrm{Al_2O_3(s)}$	18.4788	45.3543	690.0	1.718
MgO(s)	Mg(g)	$\mathrm{Mg(g)} + \mathrm{O(g)} \rightarrow \mathrm{MgO(s)}$	11.9237	33.1593	1100.0	1.646
FeO(s)	Fe(g)	$\mathrm{Fe(g)} + \mathrm{O(g)} \rightarrow \mathrm{FeO(s)}$	11.1290	31.9850	580.0	1.682
$\mathrm{Fe_3O_4(s)}$	Fe(g)	$3\mathrm{Fe(g)} + 4\mathrm{O(g)} \rightarrow \mathrm{Fe_3O_4(s)}$	13.2889	39.1687	400.0	1.805
FeS(s)	Fe(g), S(g)	$\mathrm{Fe(g)} + \mathrm{S(g)} \rightarrow \mathrm{FeS(s)}$	9.31326	30.7771	380.0	1.932
Ti(s)	Ti(g)	$\mathrm{Ti(g)} \rightarrow \mathrm{Ti(s)}$	5.58902	16.6071	1510.0	1.615
V(s)	V(g)	$\mathrm{V(g)} \rightarrow \mathrm{V(s)}$	6.15394	17.8702	1697.0	1.490
Cr(s)	Cr(g)	$\mathrm{Cr(g)} \rightarrow \mathrm{Cr(s)}$	4.67733	16.7596	1880.0	1.421

Table 2.1 (cont'd)

Grain	Key Species	Formula	A/10^4(K)	B	σ(erg/ $\mathring{A}^2$)	a_0(Å)
Co(s)	Co(g)	Co(g) $\rightarrow$ Co(s)	5.03880	16.8372	1936.0	1.383
Fe(s)	Fe(g)	Fe(g) $\rightarrow$ Fe(s)	4.84180	16.5566	1800.0	1.411
Ni(s)	Ni(g)	Ni(g) $\rightarrow$ Ni(s)	5.09310	17.1559	1924.0	1.377
Cu(s)	Cu(g)	Cu(g) $\rightarrow$ Cu(s)	3.97955	14.9083	1300.0	1.412

Note. — List of grain reactions. The parameters A, B are parameters for finding free energy[a]$-\Delta G/kT = -A/T + B$ σ gives experimentally determined surface tensions, and $a0$ is the expected monomer size.

[a] These values can be found using the NASA coefficients for individual species McBride (1993). In brief, $\Delta G = \Delta H - T\Delta S$. The polynomials given in McBride (1993) provide $\Delta H, \Delta S$ for the species to determine ΔG. Values presented here are fit to a simpler form $-A/T + B$, although this is not required.

The thermodynamics of phase change are determined by the saturation S, which is evaluated with respect to the key species as

$$\ln S = \ln \frac{p_1}{p_{1,s}} = -\frac{\Delta G}{kT} - \left\{ \ln \frac{p_1}{p_s} - \ln \left[\frac{\prod_{k=1}^{i} (p_k^{\mathcal{A}}/p_s)^{\nu_k}}{\prod_{k=1}^{j} (p_k^{\mathcal{B}}/p_s)^{\eta_k}} \right] \right\} \tag{2.9}$$

where $p_{1,s}$ is the vapor pressure. The thermodynamic potential ΔG of a reaction is determined using a two-parameter data fit $\Delta G/kT = -A/T + B$, where A, B are derived using the table of NASA coefficients (McBride, 1993) for the component species. The values used here are given in Table 2.1.

In a Lagrangian cell of volume $V(t)$ the concentration of grains composed of n monomers of the key-species is given by $c_n(t) = N_n(t)/V(t)$, where $N_n(t)$ is the total number of n-mers. $c_1(t)$ represents the vapor-phase concentration of key species monomers. For convenience, let us introduce the *nominal* concentration $\tilde{c}_n$ defined as the concentration of monomers that would result if no dust formation occurred. By definition, then

$$c_n(t_0)V(t_0) = \tilde{c}_n(t)V(t) \tag{2.10}$$

where t_0 is the initial value of time. Equation (2.10) simply states that, without any nucleation depletion, the number of n-mers is conserved. Mass conservation of the key species can then be written as

$$\tilde{c}_1 V - c_1 V = \sum_{n=2}^{n_*-1} n c_n V + \int_{t_0}^{t} V(t') J_{n_*}(t') \frac{a^3(t,t')}{a_0^3} dt' \tag{2.11}$$

where n_* is the *critical size*, $a(t,t')$ is the radius of the of the grain nucleated at t' measured at t, and a_0 is the monomer radius. The summation on the right-hand side counts all current n-mers formed up to the critical cluster, and the integration accounts for the nucleation of growth of all n-mers since t_0.

Instead of following the detailed kinetics of precritical n-mers, we assume that all grains form from the vapor as critical clusters and use the modified form of steady-state nucleation rate Equation (2.7). Equation (2.11) simplifies to

$$\tilde{c}_1 V - c_1 V = \int_{t_0}^{t} V(t') J_*(t') \frac{a^3(t,t')}{a_0^3} dt' \tag{2.12}$$

where $J_*(t)$ is the modified steady-state rate given by Equation (2.8), where the $*$ subscript indicates that we are nucleating critical size clusters. Letting $I_* = J_*/\tilde{c}_1$, dividing by $\tilde{c}_1(t)V(t)$ and letting

$$K_3 = \int_{t_0}^{t} I_*(t') \frac{a^3(t,t')}{a_0^3} dt' \tag{2.13}$$

we arrive at the simple equation for mass conservation

$$1 - \frac{c_1}{\tilde{c}_1} = 1 - Y_1 = K_3 \tag{2.14}$$

where $Y_1 = c_1/\tilde{c}_1$ is the normalized concentration of key species monomers.

The integral equation Equation (2.14) is solved by a transformation into a set of first-order differential equations (ODEs). Repeated differentiation of Equation (2.13) leads to

$$\frac{dK_i}{dt} = \begin{cases} I_*(t) n_*^{\frac{i}{3}} + \frac{i}{a_0}\left(\frac{da}{dt}\right) K_{i-1} & \text{for } i = 1 \ldots 3 \\ I_*(t) & \text{for } i = 0 \end{cases} \tag{2.15}$$

These equations are coupled to that of grain growth,

$$\frac{da}{dt} = \gamma \Omega_0 \sqrt{\frac{kT}{2\pi m_1}} c_1 \left(1 - \frac{1}{S}\right) \tag{2.16}$$

to allow the determination of K_3, and the grain concentration Y_1 immediately follows from Equation (2.14).

The concentrations of non-key species due to nucleation are determined by the rate of key-species as

$$\begin{aligned} Y_k^{\mathcal{A}} &= \frac{c_k^{\mathcal{A}}}{\tilde{c}_1} = \frac{\tilde{c}_k^{\mathcal{A}}}{\tilde{c}_1} - \nu_k^{\mathcal{A}}(1 - Y_1) \\ Y_k^{\mathcal{B}} &= \frac{c_k^{\mathcal{B}}}{\tilde{c}_1} = \frac{\tilde{c}_k^{\mathcal{B}}}{\tilde{c}_1} + \eta_k^{\mathcal{B}}(1 - Y_1) \end{aligned} \tag{2.17}$$

where $\mathcal{A}, \mathcal{B}$ identify reactant, product species as in the reaction given by Equation (2.6). Further, various grain properties naturally arise from inspection of the moments K_i:

$$N_{dust} = \tilde{c}_1 K_0 \tag{2.18}$$

$$c_{dust} = \tilde{c}_1 K_3 \tag{2.19}$$

$$\hat{r}_{dust} = a_0 \left(K_3/K_0\right)^{1/3} \tag{2.20}$$

where N_{dust} is the total number of grains, c_{dust} is the concentration of grains, and $\hat{r}_{dust}$ is the average grain radius.

2.3.3.1. Implementation

We have implemented the model of the previous section into a python code called *nuDust*. *nuDust* is built to use the libraries NumPy (Harris et al., 2020) and SciPy (Virtanen et al., 2020) for fast and accurate numerical algorithms. The numba (Lam et al., 2015) library is used for just-in-time (JIT) compilation of python code to produce efficient machine code, and to facilitate thread and GPU parallelization. This code takes as input a list of chemical and nucleation reactions, an initial chemical composition, and the time-series data of a prior hydrodynamics simulation. Lagrangian cells act as a 0-D box of vapor. We assume the vapor is composed of hot, inert *monomers*, with a chemical composition taken from the initial model setup.

Time-series data of the hydrodynamics of the cell are used to construct a cubic piece-wise polynomial spline (Akima, 1970) for interpolating values of temperature and density (Fig. 2.6). Before integration begins, the initial concentrations are modified by assuming the complete formation of the fast-forming molecules CO and SiO.

At the beginning of each time-step, temperature T and density ρ values are evaluated, along with their derivatives. The system of ordinary differential equations (ODEs) are simultaneously evolved for every species until all key species have been exhausted or the temperature of a cell falls below a threshold value where there will be no further chemical activity with respect to nucleation and grain growth. With $\vec{x}$ as a vector of concentrations c_i of N chemical species and $\boldsymbol{K}_j = (K_j^0, K_j^1, K_j^2, K_j^3)$ of M grain moments

$$\vec{x} = (\{c_i\}, \{\boldsymbol{K}_j\}) \quad i = 1, \ldots, N, \quad j = 1, \ldots, M \tag{2.21}$$

we solve the initial value problem

$$\begin{aligned} \frac{d\vec{x}}{dt} &= f(\vec{x}, t) + \vec{x}_c(d\rho/\rho) \\ \vec{x}_c &= (\{c_i\}, \ldots, 0, \ldots) \quad i = 1, \ldots, N \end{aligned} \tag{2.22}$$

where $f(\vec{x}, t)$ is constructed from Eqs. (2.14, 2.15, 2.16). The second term in Equation (2.22) accounts for the change in the concentrations of chemical species (though not the grain moments) due to the volume change of the Lagrangian cell.

The LSODA (Hindmarsh, 1983) integrator provided by SciPy is used for integrating Equation (2.22). This integrator uses automatic selection of non-stiff and stiff methods. The Jacobian matrix $\boldsymbol{J} = \partial f / \partial \vec{x}$ for implicit integration are determined numerically using finite-differencing. User-provided relative (E_{rel}) and absolute (E_{abs}) error tolerances adjust the time-step so that

$$\|e_i\| \leq \max(\vec{x} * E_{rel}, E_{abs}). \tag{2.23}$$

2.4. Results

To probe the dependence of dust formation on the properties of the supernova, we first constructed a large database of supernova explosion models evolved out to a minimum of 1157 days post-explosion by continuing the hydrodynamical evolution of many of the existing results obtained by Fryer et al. (2018) with the simplified FR99 code. Our database encompasses 21, 30, and 21 explosion models with M_{prog} = (15, 20, 25) $M_\odot$, respectively, for a total of 72 explosion models covering a wide range of explosion energies, $E_{exp} = (0.53 - 18.4) \times 10^{51}$ erg. As a note, seven of the 30 models with $M_{prog} = 20$ $M_\odot$ cover a range of $E_{exp} = (4.3 - 124) \times 10^{51}$ erg and are used to help represent lobes of single-lobe asymmetric supernova and double-lobe hypernova explosions. The database of the explosion models used is given in Table A.1 in Appendix A.1 . This large suite provides a wide probe of the explosion energy parameter space that we are investigating.

The temperature, density (T, ρ) trajectories from these explosion models are used as input in our dust formation code, producing a database of dust nucleation models. All of our dust models were studied out to a minimum $t = 1157$ days to provide ample time for most of the grain species modelled to nucleate and grow before the corresponding key species were fully depleted or the simulation evolved beyond a (T, ρ)-space that was amenable to dust nucleation and growth. This time period is relatively short compared to the evolutionary timescale of young supernova remnants and allows us to probe the growth of dust grains in CCSN ejecta prior to the reverse shocks that occur when the ejecta interacts with the ISM at the onset of the SNR stage.

We used the moment equations described in Section 2.3 to calculate the mass of the dust species in each model as well as the average radius of the dust grains for each grain species. Table A.3 in Appendix A.1 gives the collated results for a number of modelled grain species that contributed significantly to the dust content for each explosion model available to us. The dust grains presented in the table have been limited to carbon-, silicon-, and oxygen-based species as the Fe-group species did not produce substantial amounts of dust except for the 25 $M_\odot$ progenitors.

The models in Table A.3 in Appendix A.1 were grouped by their explosion model designations (e.g. M15a, M20b, etc) and ordered by explosion energy within these subgroups. It is clear that, within these energy-ordered subgroups and across the three separate progenitor classes, the amount of dust produced by $t = 1157$ days depends upon the explosion energy and progenitor. This trend is generally observed for all productive dust species. In this section, we review these trends focusing on the distributions and growth of the dust grains.

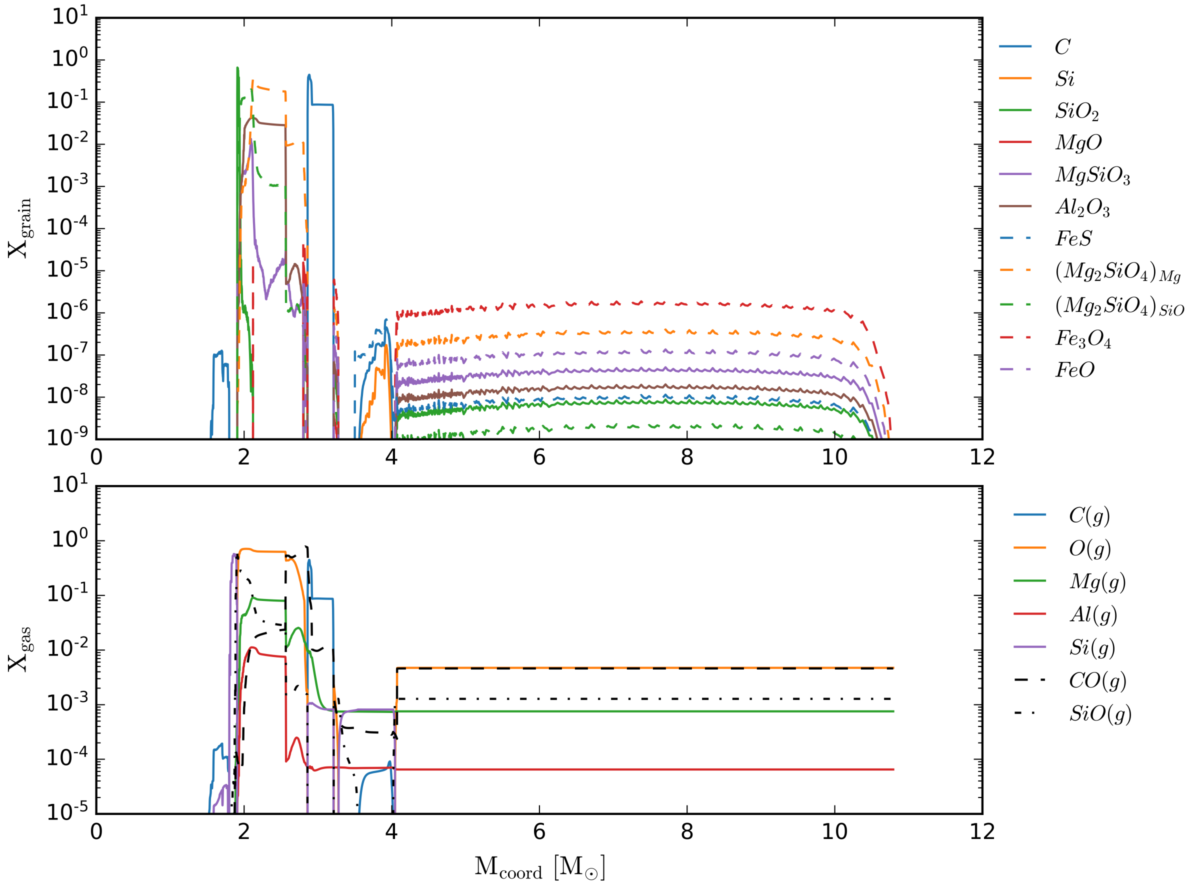

Figure 2.4: Top: Mass of select dust grains (M_{grain}) as a function of the mass coordinate of the original star given as colored lines. Bottom: Mass of gas phase elements and molecules (M_{gas}) as a function of mass coordinate. The gas-phase molecules CO(g) and SiO(g) are given as dashed and dotted black lines, respectively. The mass of free C(g), O(g), Mg(g), Al(g), and Si(g) are given as solid, colored lines. Both panels use data from model M15cE3.43, with $M_{prog} = 15 M_\odot$ and $E_{exp} = 3.42$ foe. It should be noted, the ejecta does not model material mixing.

2.4.1. Distribution of Dust in the Ejecta

Figures 2.4, 2.5, and 2.6 show the dust fractions for different dust species, at time $t \approx 1157$ days, as a function of enclosed mass for models M15cE3.43, M20bE2.6, and M25aE4.73 corresponding, respectively, to M_{prog} = (15, 20, 25) $M_\odot$ zero-age main-sequence progenitors. The energies for these three progenitors are $E_{exp} = (3.43, 2.60, 4.73) \times 10^{51}$ erg. These models were selected as examples of our three progenitor masses with large dust production and similar energies.

The figures plot the distributions of only a handful of the most abundant dust grains: C, Si, SiO_2, MgO, $MgSiO_3$, Al_2O_3, and Mg_2SiO_4 (both grain reaction variants). The plot shows the abundances of each dust species produced versus enclosed mass of the ejecta in the top panels of each figure. We also include the abundances of the CO and SiO gas phase molecules pre-formed in our simulations as well as the abundances of the free gases available to grain nucleation in the bottom panels (all references to free-gas dominant shells can be obtained from the bottom panels of Figures 2.4, 2.5, and 2.6). Additionally, the bottom panels show the abundances of free gas species at time $t \approx 0$ days. We would like to note that these results are for a strictly unmixed ejecta.

In the remainder of this subsection, we review the dust distributions of each progenitor in turn. The top panel in Figure 2.4 shows the distinct growth regions of the different dust grains. In the hydrogen envelope, $\mathrm{M_{coord}} \approx [4-11]$, the solar abundance pattern produces low abundance fractions ($\mathrm{X} \lessapprox 10^{-6}$) of a broad set of silicate and oxide grain species. Within the helium layer, $\mathrm{M_{coord}} \approx [3.25-4]$, abundance shifts produce very small amounts of C, Si, FeS dust ($\mathrm{X} \lessapprox 10^{-6}$). Significant amounts of dust are only produced in the central regions of the ejecta, corresponding to the carbon through silicon layers of the progenitor. In the free carbon-dominant shell, $\mathrm{M_{coord}} \approx [3-3.25]$, the free carbon fraction is high, producing abundant carbon dust. The abundance fraction of carbon dust in this region ranges from 0.1-0.4 in the top panel of Figure 2.4. Comparing this to the bottom panel of the same figure, we see that the abundance fraction of free carbon for this same region is nearly identical, indicating a near-total conversion of free carbon into carbonaceous grains.

Moving deeper into the ejecta, we first cross a transition region between the free carbon-dominant and free oxygen-dominant shells, where the pre-formation of CO gas molecules is very high. This transition region is nearly fully depleted in free carbon gas and shows a strong free oxygen gas depletion curve, $\mathrm{M_{coord}} \approx [2.5-3]$ with $\mathrm{X} \lessapprox [0.5-0.001]$, respectively. This C-O transition region initially contains free Mg, SiO, and Al gas abundance fractions ranging approximately within 0.01-0.03, 0.002-0.003, and 0.0001-0.0003, respectively. Subsequently, we see the modest formation of $\mathrm{Mg_2SiO_4-Mg}$, $\mathrm{X} \approx 0.01$, and limited formation of $\mathrm{MgSiO_3}$, $\mathrm{Al_2O_3}$, and $\mathrm{Mg_2SiO_4-SiO}$, $\mathrm{X} \lessapprox 10^{-5}$.

Once we are fully in the free oxygen-dominant shell ($\mathrm{M_{coord}} \approx [2-2.75]$), $\mathrm{Mg_2SiO_4}$ (both reactions combined) and $\mathrm{Al_2O_3}$ dominate the abundances with approximately 0.2-0.35 and 0.03-0.05 of the abundance fractions taken, respectively. There is also a spike of $\mathrm{MgSiO_3}$ around $\mathrm{M_{coord}} \approx 2.1$ with an abundance fraction of 0.001. Interestingly, around $\mathrm{M_{coord}} \approx [1.8-2.2]$, we see steep drop off of $\mathrm{Mg_2SiO_4-Mg}$ abundances by several orders of magnitude before vanishing to zero at $\mathrm{M_{coord}} \approx 2.1$. This feature coincides with a strong increase in $\mathrm{Mg_2SiO_4-SiO}$ abundances by a two orders of magnitude over the same region of mass coordinates. Moving minimally deeper into the ejecta, we arrive at the transition from free oxygen-dominant to free silicon-dominant shells that contains the highest abundance of free SiO gas molecules. Unsurprisingly, we see large abundances of this material go into $\mathrm{SiO_2}$ formation comprising 70 percent of the abundance fraction.

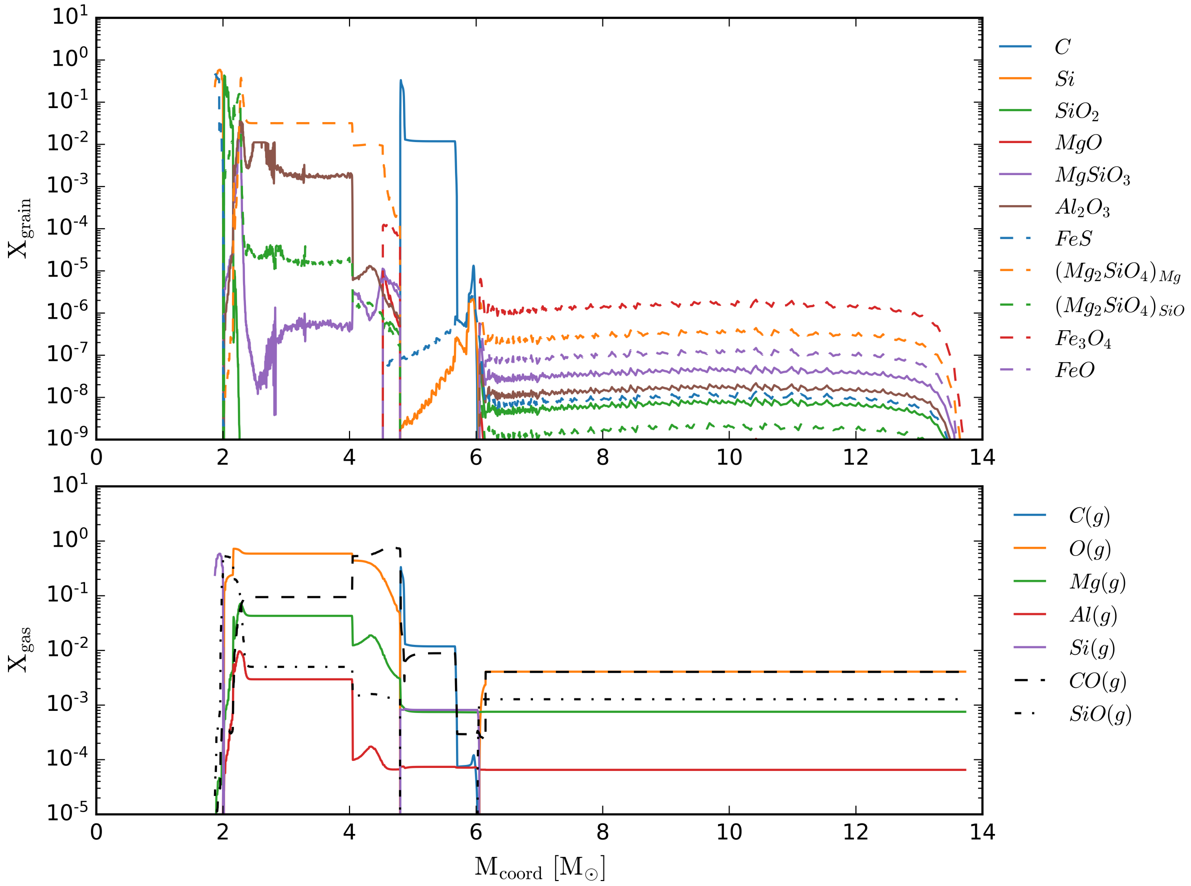

Figure 2.5: Top: Same as 2.4 top panel. Bottom: Same as 2.4 bottom panel. Both panels use data from model M20bE2.60, with $M_{prog} = 20 M_\odot$ and $E_{exp} = 2.60$ foe. It should be noted, the ejecta does not model material mixing.

Figure 2.5 shows the corresponding images for the 20 $\mathrm{M}_{\odot}$ progenitor model where the dust species follows the same trends as the 15 $\mathrm{M}_{\odot}$ progenitor dust distribution. However, there are noticeable differences between the two models, with the first difference being that the distinct regions of dust growth are extended in mass coordinate due to the larger ejecta mass and corresponding progenitor composition shells. For example, the carbon rich layer, $\mathrm{M}_{\mathrm{coord}} \approx [4.75 - 5.75]$, spans a region $\Delta\mathrm{M}_{\mathrm{coord}} \approx 1.0$ for the 20$\mathrm{M}_{\odot}$ progenitor compared to $\Delta\mathrm{M}_{\mathrm{coord}} \approx 0.5$ for the 15 $\mathrm{M}_{\odot}$ mass progenitor, resulting in a larger total carbon dust mass for this shell within the ejecta. In the O/Mg/Al region of the ejecta, $\mathrm{M}_{\mathrm{coord}} \approx [2.25 - 4.75]$, the production of $(\mathrm{Mg_2SiO_4})_{Mg}$ dominates silicate production, followed by $(\mathrm{Mg_2SiO_4})_{SiO}$ and $\mathrm{MgSiO_3}$ production. We see similar $\mathrm{Al_2O_3}$ production comprising the second largest abundance fraction of the dust species in this layer. It should be noted that while these regions are extended along mass coordinate in comparison to Figure 2.4, the abundances of each of $\mathrm{Al_2O_3}$ and the silicates shown are reduced by about one order of magnitude each for most of the region of the ejecta. We also observe the same silica abundance spikes (up to 50 percent of the abundance fraction) with an additional layer of pure silicon dust (peaking at 60 percent of the abundance fraction) at the oxygen-silicon interface occurring around $\mathrm{M}_{\mathrm{coord}} \approx [1.8 - 2.2]$. While it is not shown here, it should be noted that for models with explosion energies 2.75 $\lessapprox$ Eexp $\lessapprox$ 5 foe, the pure silicon dust spike does not occur due to insufficient free-Si remaining after SiO gas phase production. This is possibly related to the dependence of key nucleosynthetic yields on the explosion energetics.

Finally, Figure 2.6 shows the same plots but now for a 25 $\mathrm{M}_{\odot}$ progenitor. This high mass progenitor model more resembles the lowest mass progenitor model given in Figure 2.4, with the distinct regions of dust production occurring in extended mass coordinate shells because of the larger ejecta mass. These regions contain ≈3 times as much mass for the carbon, O/Mg and O/Si layers when compared to the 15 $\mathrm{M}_{\odot}$ progenitor in Figure 2.4. We see all of the same features as noted from before. One comment about the overall abundance fractions for the dominant dust species in the O/Mg layer, we see that only $(\mathrm{Mg_2SiO_4})_{SiO}$ and $\mathrm{Al_2O_3}$ have the same drop in typical abundance by about one order of magnitude as seen also in the 20 $\mathrm{M}_{\odot}$ progenitor of Figure 2.5. We also observe a large silicon dust feature in the innermost ejecta.

2.4.2. Growth of Grain Mass

With our set of models, we can also study the growth of dust in terms of mass and average radius as a function of time. Various species of dust grains will form at different regions of (T, ρ)-space which will impact the time at which these grains can be observed at post-explosion. For this analysis, we continue to partition our results by the progenitor masses of the explosion models.

We first give the results of dust production as a function of time for a select number of grain species and explosion models for each progenitor class in our database in Figure 2.7. We show the

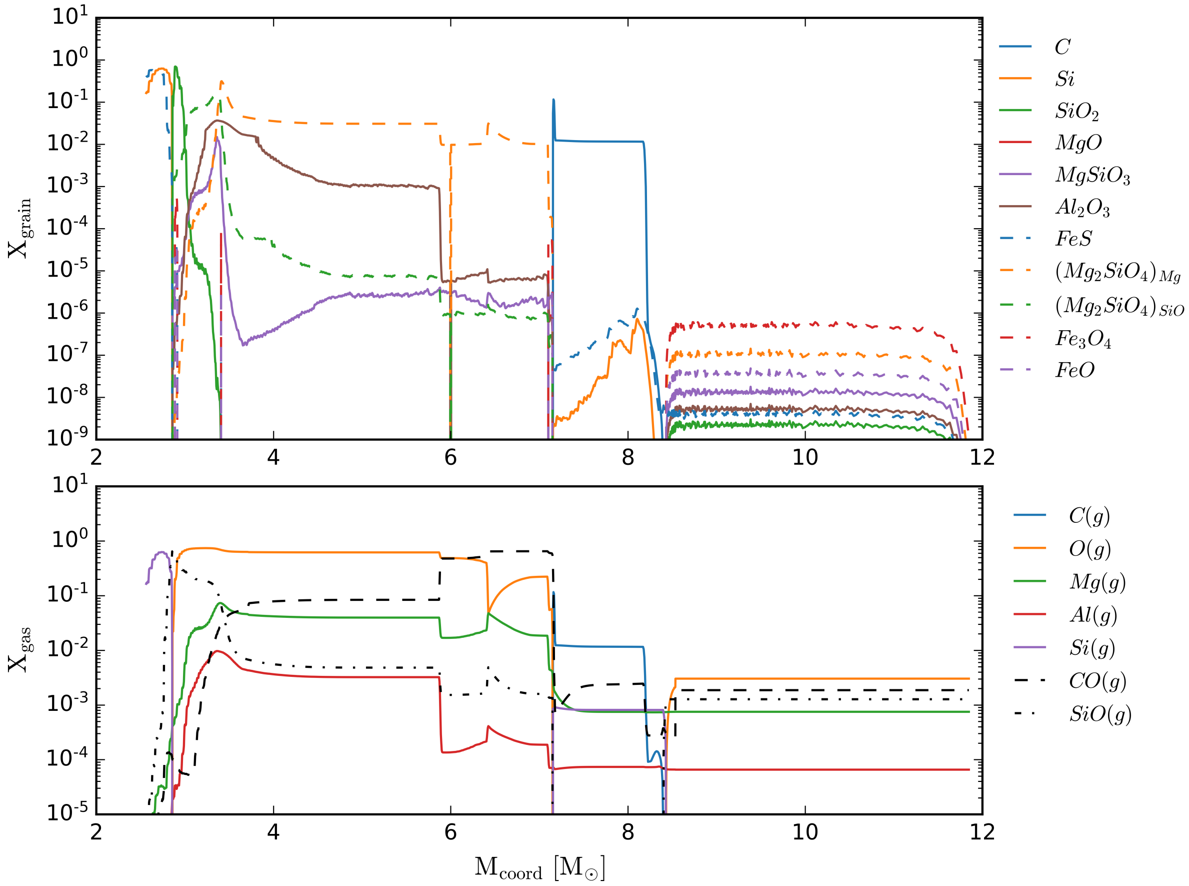

Figure 2.6: Top: Same as 2.4 top panel. Bottom: Same as 2.4 bottom panel. Both panels use data from model M25aE4.73, with $M_{prog} = 25\mathrm{M}_\odot$ and $E_{exp} = 4.73$ foe. It should be noted, the ejecta does not model material mixing.

mass of C, Al_2O_3 $MgSiO_3$, and Mg_2SiO_4 in purple, cyan, olive, and red lines, respectively as it evolves over time throughout the dust simulation from 0 to 1157 days. We note that the general trend seen in all panels of Figure 2.7 is that as explosion energy increases, the time at which bulk grain production occurs is earlier and earlier. This trend is also generally agnostic of the grain species, indicating that this result is potentially directly tied to the explosion energetics.

For example, looking at the top panel of the figure, with 15 $M_\odot$ progenitors, we see that for the 1.86 foe model, bulk carbon growth occurs around the 800 day mark, whereas this bulk growth occurs around 700 and 650 days for the 2.6 and 3.42 foe models, respectively. For the middle panel with 20 $M_\odot$ progenitors, the effect is even more pronounced with bulk carbon growth occurring at 550, 650, and 800 days for 2.6, 1.47, and 0.85 foe explosions. Going to the bottom panel with the largest 25 $M_\odot$ progenitors and the dust production bulk carbon production occurs even earlier at around 350, 375, and 500 days for 4.73, 2.78, and 0.99 foe explosions. This uncovers another trend in that progenitor mass is correlated with the time at which bulk dust production occurs, not only for carbon grains, but for the other grain species presented in Figure 2.7. That is, one requires less energetic ejecta to obtain earlier bulk dust production for various grain species as one increases the progenitor mass of the star.

Figure 2.8, reports the total dust mass for graphite, silicates and all species grouped together as a function of time for our suite of models for up to 1157 days of dust production post-explosion. The total dust mass for each model is plotted along with the left-hand column with explosion energy color-coded with the given color-bar to the side of each row of panels. For the left-hand column of panels, the models with explosion energy less than 2 foe are given as solid lines and more energetic models are presented with dashed lines. The dust masses of carbon grains and silicate grains are given in the right-hand column, denoted by solid and dashed lines, respectively. The same explosion energy color-coding applies for the right-hand column of panels. Each row of plot panels represent the 15, 20, and 25 $M_\odot$ progenitor models of each explosion for the top, middle, and bottom rows of panels, respectively. We first look to the left-hand column of panels in Figure 2.8 for each set of progenitor star models. For the 15 and 20 $M_\odot$ progenitor sets, we see the same trend that was elucidated in Figure 2.7 where explosion energy will affect the time at which bulk dust production will occur with very few exceptions. In the left-top panel, we see that earliest bulk production occurs around 625 days for a model with explosion energy around 8-10 foe and the latest bulk production occurs around 1000 days or later for all models with explosion energies less than 2 foe. The delay time for bulk dust production spans more than 500 from earliest producer to latest producer over an explosion energy range of 0.5-11 foe for these 15 $M_\odot$ progenitors. Looking to the left-middle panel with 20 $M_\odot$ progenitors, we see for an explosion energy range of $\approx$1-125 foe, the delay time in total dust production spans a range of about 60 days to 1000 days with the delay time increasing with decreasing explosion energy. Both the left-top and left-middle panels

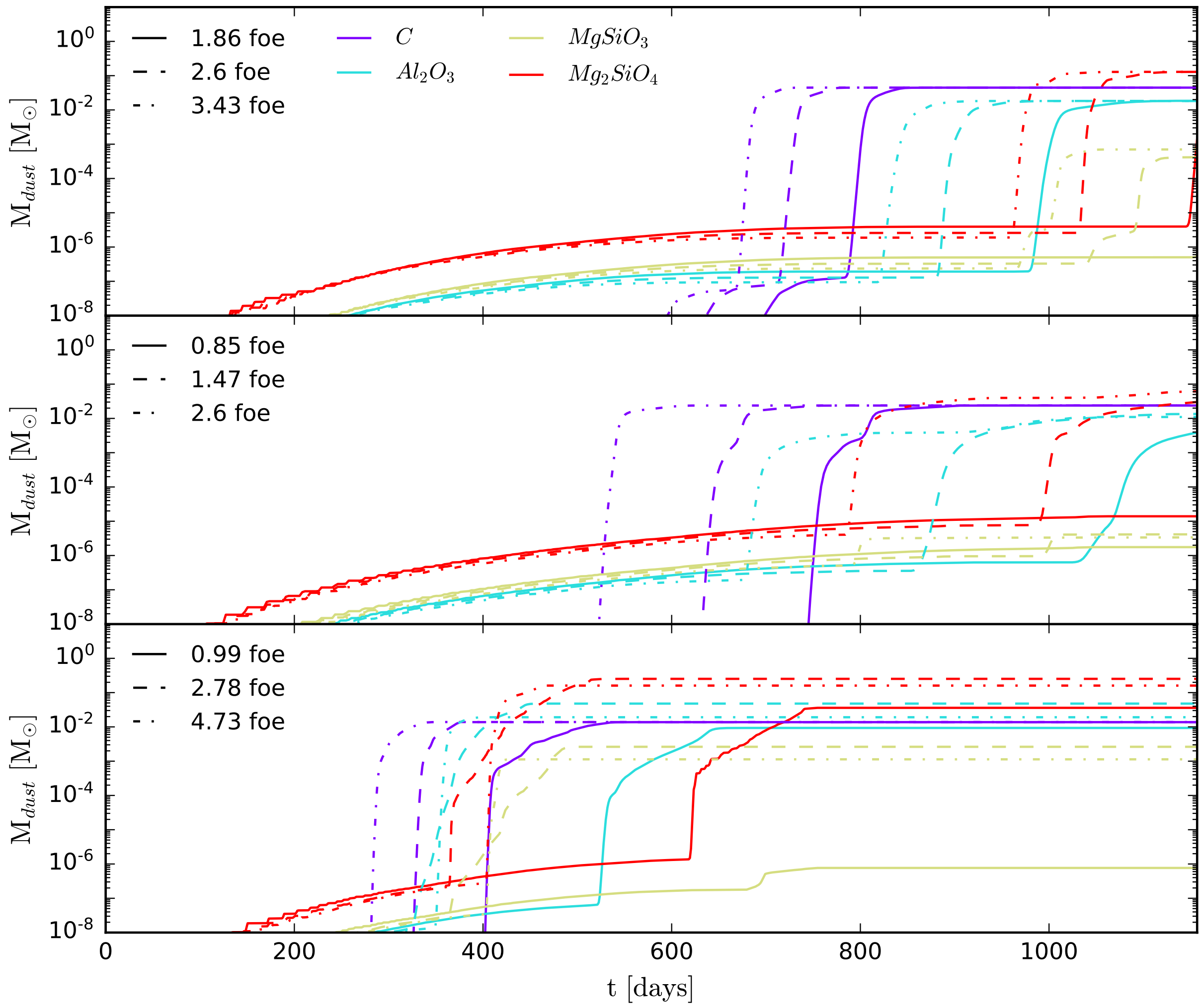

Figure 2.7: Top: The mass ($M_\odot$) of select dust grains as a function of time after shock breakout for three CCSN models, differentiated by increasing explosion energy, with $M_{prog} = 15M_\odot$. Grain species plotted are C(s), Al_2O_3(s), $MgSiO_3$(s), Mg_2SiO_4(s) as purple, cyan, gold, and red lines, respectively. The three CCSN models represented here have $E_{exp} = 1.86, 2.60, 3.43$ foe and are plotted as solid, dashed, and dash-dotted lines, respectively, for each grain species. Middle: The same as the top panel, except with three CCSN models for a $M_{prog} = 20M_\odot$ and $E_{exp} = 0.85, 1.47, 2.60$ foe plotted with solid, dashed, and dash-dotted lines, respectively, for each grain species. Bottom: Same as the top panel, except with three CCSN models for a $M_{prog} = 25M_\odot$ and $E_{exp} = 0.99, 2.78, 4.73$ foe plotted with solid, dashed, and dash-dotted lines, respectively, for each grain species.

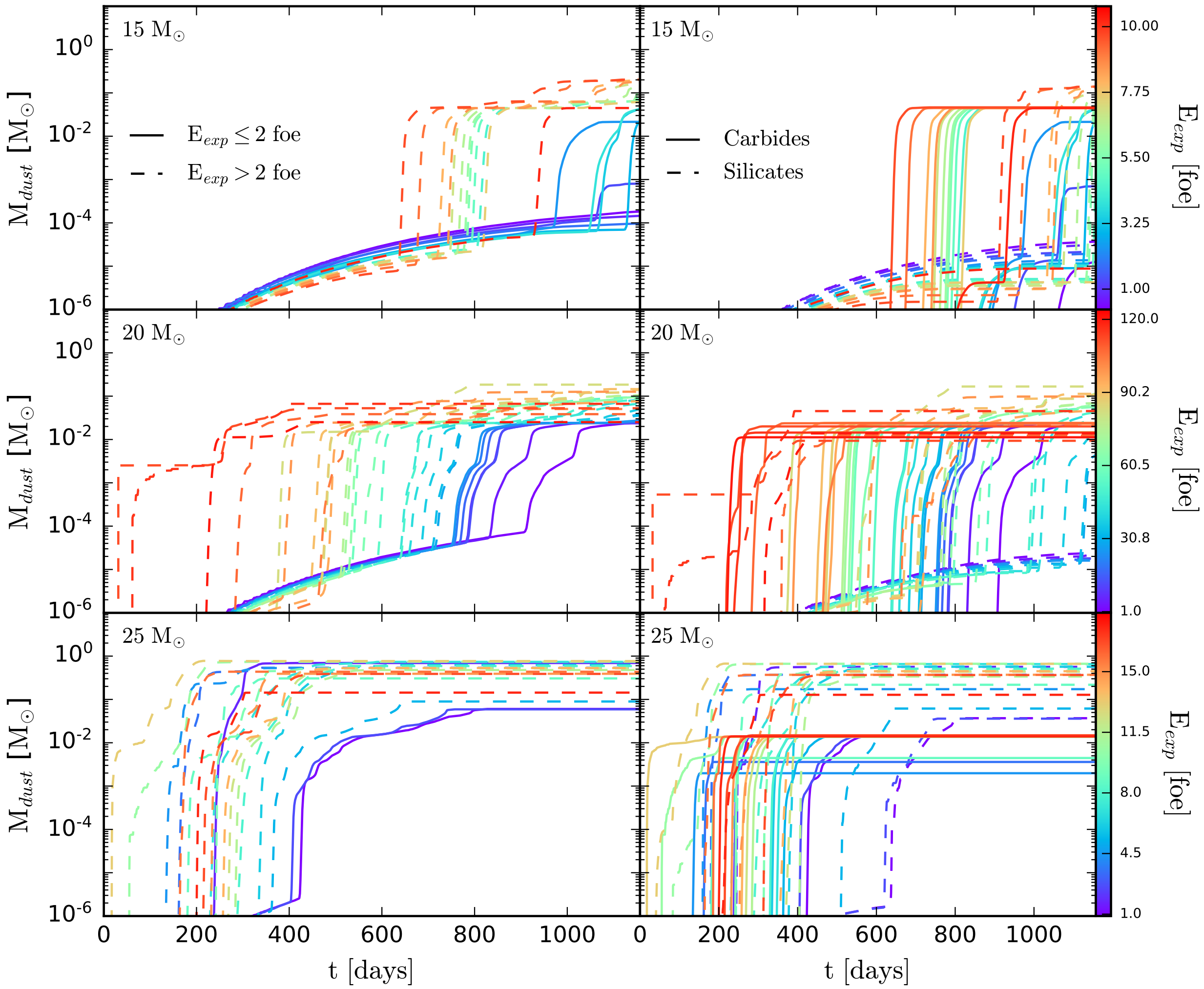

Figure 2.8: Top-left: The total amount of dust produced per model (M_{dust}), given in solar masses, as a function of time (t), given in days, for explosion models with a $15\mathrm{M}_\odot$ progenitor mass. The explosion energies (E_{exp}), in units of foe, of each model are color coated by the colorbar given adjacent to the Top-right panel. Additionally, models for $E_{exp} \leq 2$ foe and $E_{exp} > 2$ foe are given with solid and dashed lines, respectively. Top-right: Similar to the top-left panel, but now solid lines represent carbon dust grains and dashed lines represent silicate dust grains. Middle-left: Similar to top-left panel, but for $M_{prog} = 20\mathrm{M}_\odot$. Middle-right: Similar to top-right panel, but for $M_{prog} = 20\mathrm{M}_\odot$. Bottom-left: Similar to top-left panel, but for $M_{prog} = 25\mathrm{M}_\odot$. Bottom-right: Similar to top-right panel, but for $M_{prog} = 25\mathrm{M}_\odot$.

show a strong correlation between explosion energy and delay time post-explosion for the bulk production of dust grains. At 1157 days, the distribution of total dust mass ranges within 0.0001-0.2 $M_{\odot}$, with the majority of these 15 $M_{\odot}$ progenitor models having total dust masses of at least 0.02 $M_{\odot}$.

A trend more readily seen among the 20 $M_{\odot}$ progenitors, the initial bulk production occurs (middle left panel of Figure 2.8) for a longer duration of time. We see that for the explosions stronger than 2.0 foe, denoted by the dashed lines in the middle left panel, the initial bulk dust production occurs very rapidly on the order of days to perhaps a few weeks, culminating in total dust masses of 0.01-0.1 $M_{\odot}$ of dust. For the weaker explosions, this process is noticeably slower, occurring in two stages, the first stage lasting on the order of 10-100 days, with this extended first phase growing longer with decreasing explosion energy. We note here that if the effects of low ^{56}Ni mass are included, this dust would form earlier. The second phase of bulk dust production for these weaker explosion models is relatively short-lived and culminates in dust masses for individual models of 0.02 to 0.1 $M_{\odot}$. Inspecting the dust mass curves once they begin to flatten also reveals that the largest producers of dust coincide with the 20 $M_{\odot}$ progenitors with explosion energies of 5-75 foe. More powerful explosions ultimately produce less dust, similarly to the much weaker explosions, by the 1157-day post-explosion mark. At 1157 days, these models have a total dust mass evenly distributed within the range of 0.2-0.2 $M_{\odot}$, similarly to the series of 15 $M_{\odot}$ progenitor models. There appears to be no correlation between total dust mass and explosion energy for models that have mostly stopped dust production.

From the right panels of Figure 2.8, we can compare the production of carbon and silicate dust species. The carbon dust, produced farther out in the star, is synthesized prior to the total sum of silicate species. In the 20 $M_{\odot}$ progenitor, the time lag between bulk carbon and bulk silicate production increases with a decrease in explosion energy, and the time lag between carbon and silicate production is about 50-100 days for the strongest explosions ($\approx$90-125 foe), decreasing to 150-200 days or more for less energetic explosions. This trend is generally seen with the 15 solar mass models (but at later times), with silicate production generally lagging behind carbon production by about 150-200 days for most models. The range of explosion energies covered by these models is not as substantial as the 20 $M_{\odot}$ progenitor set but still elucidates the length of carbon-silicate production delay time correlation with explosion energy. Again, these trends are not as strong in the 25 $M_{\odot}$ progenitor models, except for the time lag trend occurring between bulk carbon and bulk silicate dust production. Another common feature is that silicates ultimately produce more dust by mass than the carbon species.

Finally, we come to the 25 $M_{\odot}$ progenitor set. Looking at the bottom left panel, the previously stated correlation between bulk dust production and explosion energy is much less pronounced. There seems to be a tendency for middle range explosions ($\approx$5-12) to produce bulk dust around the same time ($t \approx 200$), or even sooner by more than 100 days, as the strongest explosions (≈12-18 foe). Furthermore, there is still a production delay time between carbon and silicate dust species that generally increases with decreasing explosion energy, with the shortest delay times being as small as ≈10-20 days for highly energetic models and as large as 200 days for the weakest explosions. This series of progenitor models, however, produces more total dust than the two lower-mass progenitor sets, with the mass of total dust ranging from 0.06-0.7 $M_\odot$, with the majority of these models having total dust masses of at least 0.3 $M_\odot$.

However, it should be reiterated that the ejecta used for each model is unmixed. As the ejecta evolves in a Sedov-like trajectory, the carbon layer sits on the outermost edge of the bulk ejecta; thus, it will be the first layer to sufficiently cool by adiabatic expansion for grain nucleation to occur in earnest. With the bulk of free O, Mg, Al, and Si existing deeper in the ejecta, it will remain denser and hotter for longer than the carbon layer and will not be able to nucleate until later times. A mixed ejecta may change the timing of bulk formation for different species groups and would need to be investigated in future studies. These results can be seen more as an upper bound of sorts on dust production and ejecta tracing.

2.4.3. Growth of Average Grain Radius

Another aspect of dust grains to analyze is the grain size and is especially important when considering dust survival/ destruction. As the SN ejecta evolves into the ISM, it decelerates, producing a reverse shock that can heat the dust and destroy it. We do not currently include this destruction in our study; we are currently incorporating it into *nudust*. Figure 2.9 shows average grain sizes as a function of time for the same set of models as seen in Figure 2.7.

First, looking at the top panel of Figure 2.9, we can see that for carbon grains the average grain radius is $r_{ave} \approx (8, 6, 5)$ microns for the 15 $M_\odot$ progenitor explosions with energies $E_{exp} = (1.86, 2.6, 3.43)$ foe, respectively. Additionally, $alumina$ grains reach average radii of $r_{ave} \approx (2.8, 2.2, 2)$ microns for explosion energies $E_{exp} = (1.86, 2.6, 3.43)$ foe. The $\mathrm{MgSiO_3}$ grains are still growing at 1157 days but have all reached a minimum average radius of $\approx [3 - 4]$ microns, with the 2.6 foe model having a marginally larger average radius. Finally, we see that the $\mathrm{Mg_2SiO_4}$ grains (both pathways grouped together) reach average radii of $r_{ave} \approx (\ 14, 11)$ microns for explosion energies $E_{exp} = (1.86, 2.6, 3.43)$ foe, with the third model still growing at this time stamp. A general trend seen for these dust grains, and most strongly in the carbon grains, is that the average grain radius for a given grain species increases with decreasing explosion energy.

Moving to the middle panel of Figure 2.9, we can inspect the average dust grain radii for the select species used among three 20 $M_\odot$ progenitor models. First, the carbon grains again show substantial variation in average radii, with $r_{ave} \approx (10, 8, 5)$ microns for explosions energies $E_{exp} = (1.86, 2.6, 3.43)$ foe. It should be noted that the 20 $M_\odot$ model with $E_{exp} = 2.6$ foe

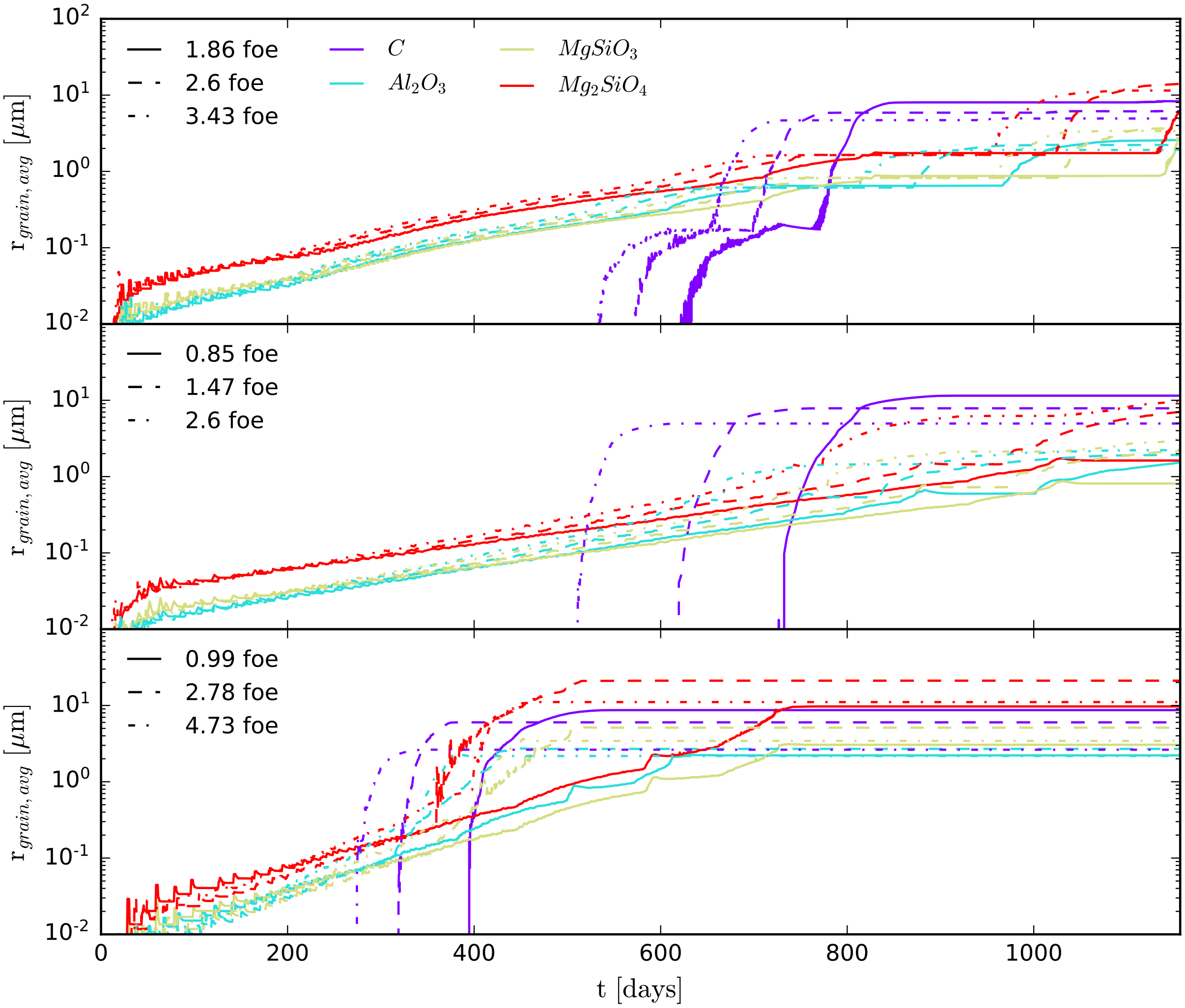

Figure 2.9: Top: The average radius (μm) of select dust grains as a function of time after shock breakout for three CCSN models, differentiated by increasing explosion energy, with a $M_{prog} = 15\mathrm{M}_\odot$. Grain species plotted are $C(s)$, $\mathrm{Al_2O_3(s)}$, $\mathrm{MgSiO_3(s)}$, $\mathrm{Mg_2SiO_4(s)}$ as purple, cyan, gold, and red lines, respectively. The three CCSN models represented here have $E_{exp} = 1.86, 2.60, 3.43$ foe and are plotted as solid, dashed, and dash-dotted lines, respectively, for each grain species. Middle: The same as the top panel, except with three CCSN models for $M_{prog} = 20\mathrm{M}_\odot$ and $E_{exp} = 0.85, 1.47, 2.60$ foe plotted with solid, dashed, and dash-dotted lines, respectively, for each grain species. Bottom: Same as the top panel, except with three CCSN models for $M_{prog} = 25\mathrm{M}_\odot$ and $E_{exp} = 0.99, 2.78, 4.73$ foe plotted with solid, dashed, and dash-dotted lines, respectively, for each grain species.

produced carbon grains with an average radius of a ≈10 microns, about 20 percent larger than the 15 $M_\odot$ progenitor of the same explosion energetics, with carbon grains of radius ≈8 microns on average. The alumina and enstatite grains for some of the models in the middle panel are still growing at time $t = 1157$ days, but we can at least inspect their average sizes at this time stamp. The enstatite grains span average radii of $r_{ave} \approx (0.8, 3, 2)$ microns for $E_{exp} = (1.86, 2.6, 3.43)$ foe, indicating no clear trend with explosion energy and dust grain radius. The alumina grains are the least interesting at the final timestamp as they are clustered around 2 µm in radius, with the lowest-energy model having slightly smaller but faster-growing grains based on the growth line slope from 1000 to 1157 days.

Finally, we have the bottom panel of Figure 2.9 showing results for a select number of grains and explosion models from the 25 $M_\odot$ progenitor group. As with Figure 2.7, the trend for these models is not as straightforward and consistent with the two lower-mass progenitor sets. However, the carbon dust carries the same trend of lower energy leading to larger average dust grains. We see that the carbon grains reach sizes of $r_{ave} \approx (9, 6, 3)$ µm for models with explosion energies, $E_{exp} = (0.99, 2.78, 4.73)$ foe. The average carbon grain size appears to mimic the carbon grain sizes for the top panel of 15 $M_\odot$ progenitor mass models for a similar span of explosion energies. Examining the forsterite grain sizes, we have $r_{ave} \approx (10, 20, 11)$ µm for $E_{exp} = (0.99, 2.78, 4.73)$ foe. The 2.78 foe explosion model produces forsterite dust grains that are about 50% larger than the 2.6 foe explosion from the top panel and 100% larger than the 2.6 foe model from the middle panel when examined at time $t = 1157$ days. The alumina grains span average radii of $r_{ave} \approx (2, 3, 2)$ microns for $E_{exp} = (0.99, 2.78, 4.73)$ foe, showing an approximately consistent size for these grains when compared to the lower progenitor models, regardless of explosion energy. And finally, the enstatite grains for these models span $r_{ave} \approx (3, 5, 3.4)$ microns for $E_{exp} = (0.99, 2.78, 4.73)$ foe, and show similar trends in average radii with the 15 $M_\odot$ progenitors in the top panel.

2.5. Conclusions

We have presented a large one-dimensional parameter study probing the affects of the SN explosion on the formation of dust in the resulting expanding ejecta. This work has been conducted as a first stage to understanding the survival of dust upon injection into the ISM and how the SN explosion may influence this survival. In our results, there are a number of trends that appear within our large set of dust formation models. The most predominant trends appear to be most correlated to the gas dynamical evolution of the expanding ejecta that is dictated by the energetics of the preceding SN explosion. As illustrated in Figures 2.7 and 2.8, time of bulk dust production, irrespective of individual grain species, is generally affected by the SN explosion energy. That is, bulk production occurs earlier for more energetic explosions, as these explosions evolve more rapidly owing to higher initial kinetic velocity.

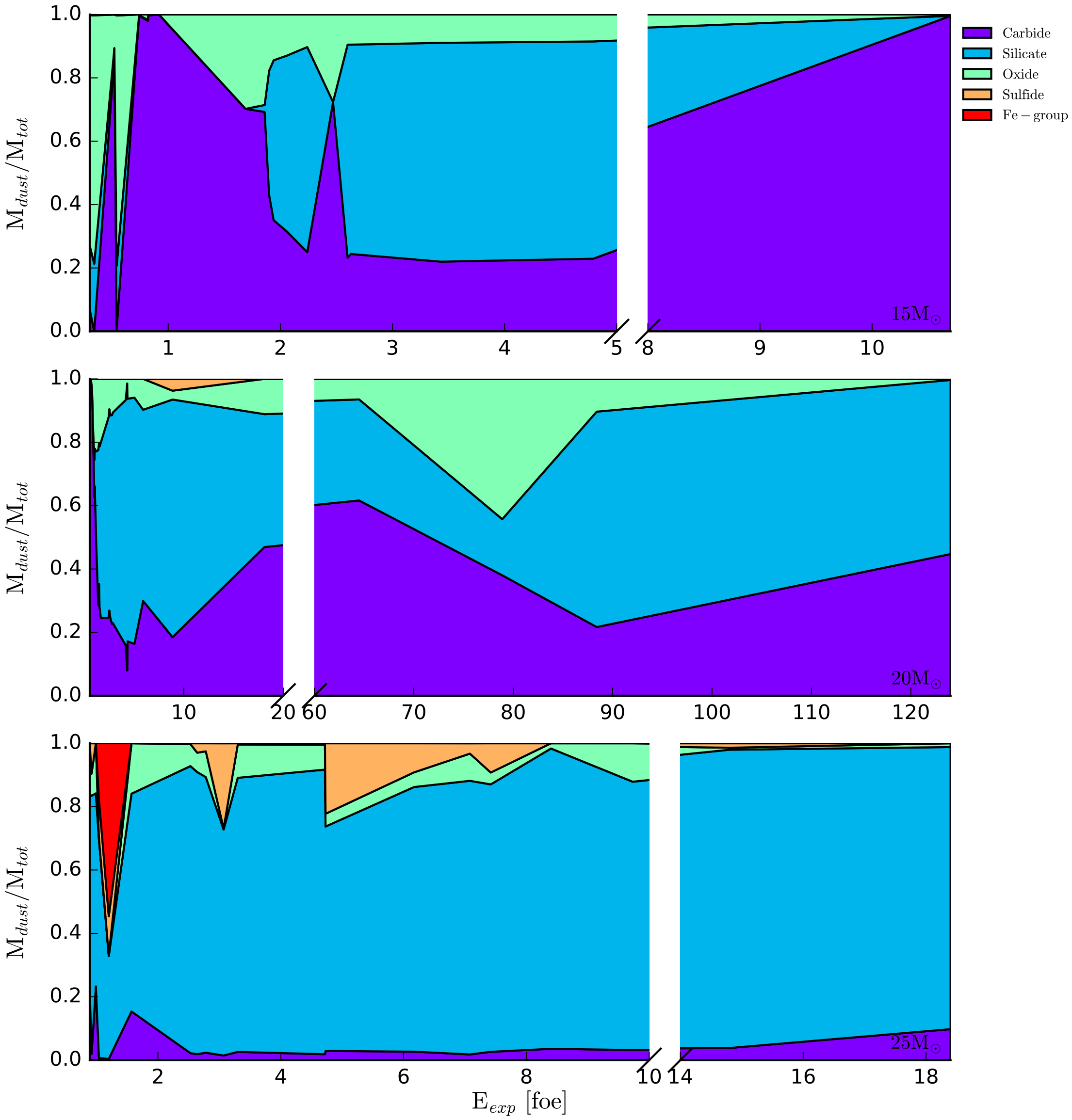

Figure 2.10: Top: Mass of carbonaceous, silicate, oxide, sulfide, and Fe-group dust formed normalized by the total dust for each model given as purple, blue, green, orange, and red shaded regions, respectively. The shaded regions give the portion of dust that each category takes of the total dust mass, as a function of E_{exp} for CCSN models with $M_{prog} = 15\text{M}_\odot$. E.g., in the top panel from 3-4 foe, carbon, silicate, and oxide grains make up $\approx 25\%$, $\approx 90 - 25 = 65\%$, and $\approx 100 - 90 = 10\%$ of the total dust mass, respectively. Middle: Same as the leftmost panel, except for all models with a$M_{prog} = 20\text{M}_\odot$. Bottom: Same as the top panel, but now for only models with $M_{prog} = 25\text{M}_\odot$. All models evolved until 1157 days.

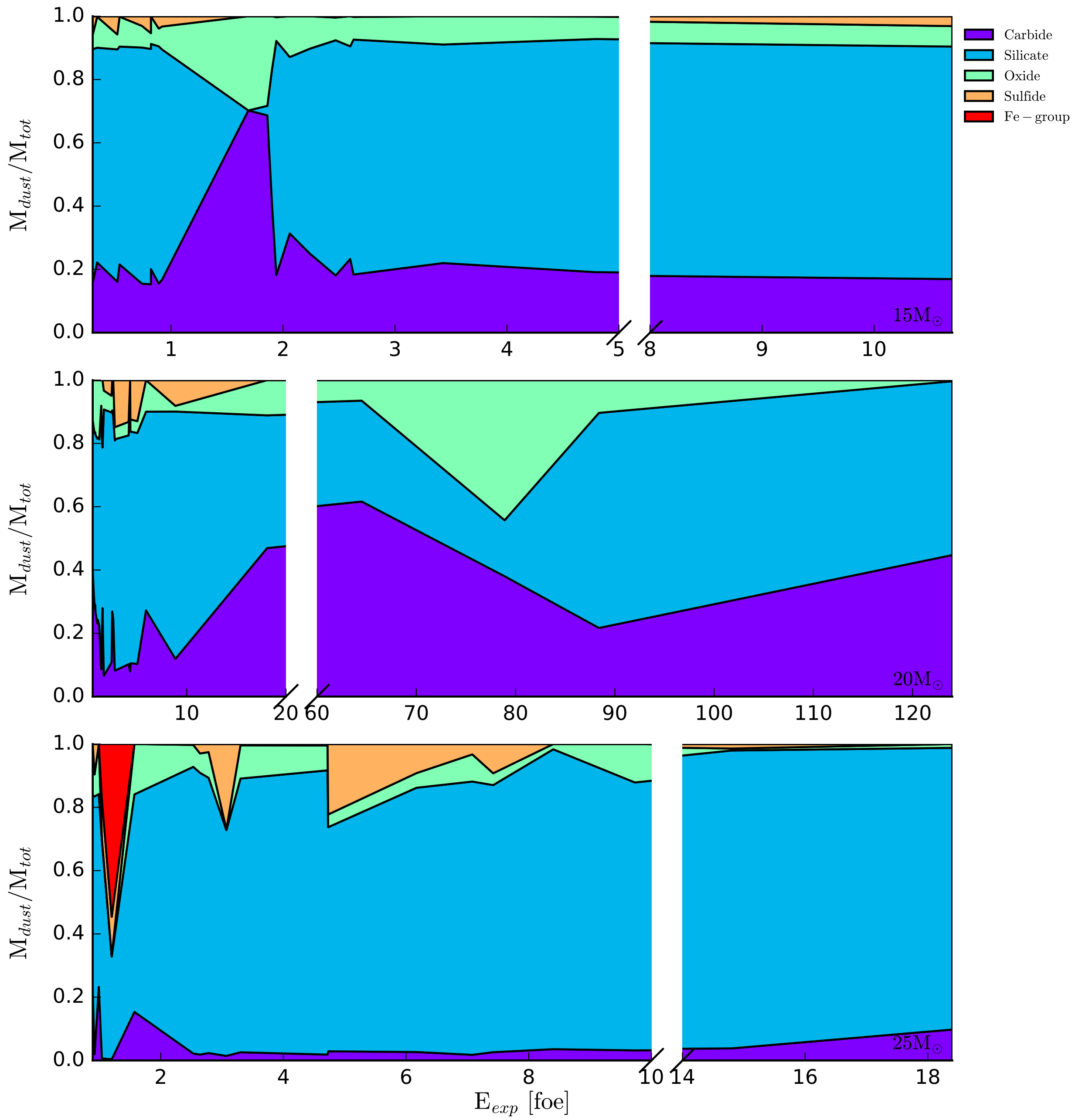

Figure 2.11: Same as Figure 2.10, except models have been evolved until dust production ceases or nearly ceases, typically between 3 and 15 years.

Furthermore, there is a correlation between time of bulk grain growth and the progenitor mass, where an increase in progenitor shortens the bulk production time when holding the explosion energetics constant. It is seen that bulk graphite production occurs typically 100-300 days before bulk production of alumina and forsterite, with the delay time of bulk production being even larger for enstatite for the 25 $M_\odot$ models.

However, there is growing evidence that the SN explosion is highly asymmetric (for a review, see Fryer et al., 2007) and additional observations continue to support this claim (Grefenstette et al., 2014). The asymmetries in the explosion will grow as the shock moves through the star and subsequent circumstellar medium, driving strong mixing. Future studies with a realistically mixed ejecta would be useful to determine whether some of the more specific trends, such as the early carbon dust formation, are a product of an unmixed ejecta or not. This motivates the need for multidimensional studies as well. The extent of mixing will alter the formation history of specific species but should not substantially impact the species agnostic gas dynamical dependence on the explosion.

We can make comparisons to previous numerical studies as a first-pass code validation. The dust evolution of 12, 15, 19, and 25 $M_\odot$ progenitors with 10^{51} ergs energetics was modeled from 100 to 1500 days in Sarangi & Cherchneff (2013) and serves as a useful starting point for comparisons. Looking at their Table 4 of results for 15 $M_\odot$ progenitor explosions at 1500 days post explosion, they report dust masses of 5.6(-3), 1.1(-4), 7.8(-3), 3.9(-4), 2.3(-2), and 6.1(-4) (using their notation in $M_\odot$) for forsterite, silica, alumina, pure silicon, pure carbon, and silicon carbide, respectively, with a total dust mass of 0.038 $M_\odot$ for the ^{56}Ni=0.075 $M_\odot$ case. For the ^{56}Ni=0.01 $M_\odot$ case, these values are 2.6(-6), 1.1(-4), 7.9(-3), 3.8(-4), 2.4(-2), 5.0(-4), for the same ordering with 0.059 for the total dust mass (all in $M_\odot$). In terms of energetics and progenitor mass, model M15bE0.92 from Table A.3 in Appendix A.1 compares best with dust masses of 8.84(-6), 2.00(-7), 4.21(-7), 0.0, 4.31(-2), 6.10(-12) for the same ordering of dust species with a total dust mass of 0.0431 $M_\odot$. It should be reiterated that these numbers are reported at 1157 days when most non-carbonaceous species are still forming at this time for low energy models.

In general, the explosion energetics for lower-energy models serves as a reasonably good parameterization of the time at which bulk dust growth occurs in our data set, and silicates ultimately form the majority of total dust for 15 $M_\odot$ progenitors with explosion energies of $\lessapprox 10^{51}$ ergs (see Figure 2.11). For higher-energy explosions for 15 $M_\odot$ progenitors, it is generally seen that carbon grain production is of the same order of magnitude, alumina and forsterite production are an order of magnitude larger, and production of all other species is several orders of magnitude (or more) smaller when compared to Table 4 of Sarangi & Cherchneff (2013). For brevity, we will comment that our 20 and 25 $M_\odot$ progenitor models share some agreement with total dust mass of the 19 and 25 $M_\odot$ models given in their Tables 6 and 7, with forsterite, alumina, silica, and carbon production generally within an order of magnitude of our models , independent of supernova explosion energy, that see dust production (mostly) resolved by our reported snapshot at 1157 days. It should be noted that Sarangi & Cherchneff (2013) used a more complex gas chemistry but a simplified explosion modeling approach based off of Nozawa et al. (2007).

There is also a clear dependence of grain size of individual species on the explosion energetics, where less energetic models ultimately produce larger dust grains as seen in Figure 2.9. The likely physical explanation here is that the cooling rate for weakly energetic explosions is lower than the cooling rate for highly energetic explosions. This means that for less bright supernovae, the ejecta traverses the (ρ,T)-space amenable to dust production over a longer period of time. This is not surprising, as the time-dependent integration of grain growth is linearly dependent on temperature as seen in Equation 2.16. We should ultimately see grains grow larger if they exist in a suitable T-space for a longer period of time.

2.5.1. Dependence of Dust Yields on Explosion Energies and Resulting Nucleosynthesis

An interesting feature of our results is the dependence of final dust abundances on the energetics and resulting nucleosynthesis of the explosion. In Figure 2.10, we see that the total dust mass of all models is dominated by silicate dust formation, followed by carbide dust, and then oxide dust. One interesting feature is the modest parabolic shape of the 20 $M_\odot$ data. It appears that the dust formation of silicates peaks around explosion energies of $4-6$ foe and decreases as explosion energy further increases to extremes. This same trend is witnessed in Figure 2.11 where we have most models evolved out to various later times (typically 5-15 yrs), such that dust formation has halted for all or at least most of the predominate species (carbides, oxides, silicates, and iron sulfide). We see that the carbon dust trend is nearly flat with explosion energy given sufficient evolution time, indicating early and efficient graphite production. We still see the parabolic peak in the silicate mass for the 20 $M_\odot$ progenitor models. There is also substantial formation of FeS for low-energy models in the 15 $M_\odot$ progenitor set. The substantial production of FeS is also seen in most models for the 20 and 25 $M_\odot$ progenitor sets, except for the 20 $M_\odot$ models with $E_{exp} < 2$ foe. Another trend seen in comparing Figures 2.10 and 2.11 is that the effects of lower explosion energy on the rate of dust production weaken with an increase in progenitor mass.

Coming back to the silicate mass peak in the 20 $M_\odot$ progenitor set, one explanation for this result is that the more energetic explosions will burn carbon into the constituents required for the nucleation of silicates. Not only does this remove carbon from the region of the ejecta that would otherwise be tied up in CO gas, but it also increases the capacity for SiO to form, a common key species of silicate nucleation, in the ejecta. This in turn allows for the increased production of silicate grain species without dramatically affecting carbon production. One important aspect to note is that there is a decrease in dust production for exceptionally energetic models. The energetics for these models is likely sufficient to further burn silicate constituents into heavier elements, such as Fe-group species, that form dust later and less efficiently. The ejecta also expands and cools the most rapidly for these particular models, and they do not stay in a (ρ, T)-space amenable to dust production for very long, reducing the overall efficiency of the dust yields. Seen throughout the unmixed ejecta of all of our 20 $M_\odot$ models, explosions with energetics $E_{exp} \lessapprox 2.75$ foe and $E_{exp} \gtrapprox 5.00$ foe have less silicon gas deep in the ejecta. The silicon gas abundance is sufficiently lower than the oxygen abundance that the silicon is entirely bound up in SiO gas. While the free silicon is dramatically reduced, it does allow for a small increase in the production of SiO-dependent dust species.

The energetics of an SN explosion sensitively impacts the resulting nucleosynthesis, affecting the isotopic yields. This sensitivity of nucleosynthetic yields should be encoded in the dust yields of the ejecta and is generally what is observed in our database of models. As discussed in Section 2.4, there is a peak in the 20 $M_\odot$ silicate mass that appears to be directly related to the final yields of intermediate-mass elements that are constituents of silicate species. Thus, it can be concluded that the final dust yields and composition of a given explosion may be dependent on the energetics. This opens up an avenue for observations, as a measure of dust yields could serve to probe the nucleosynthesis of post-explosion CCSNe and test the viability of different explosion engines.

2.5.2. Discussion

Our goal with this study was to identify dust characteristics that may arise from a large, one-dimensional parameter study of more than 70 CCNSe, varying progenitor mass, composition, and explosion energies. For simplicity, important features of stellar atmospheres and outflows, including ”clumpy” regions and energetic products produced from Ni-decay, are not components of the module we used to produce our data. Further, grain destruction through shocks has not been included in the model.

In overdense, or clumpy, regions, dust can form more efficiently and grow to larger sizes (Indebetouw et al., 2014). These regions also have been shown to produce distinct formation histories, and pure metallic grains may see increased formation in these regions. These effects are worth studying in the future.

In quantifying the effects of ^{56}Ni mass on condensation, Sarangi & Cherchneff (2013); Sarangi & Cherchneff (2015) noted that for 12 $M_\odot$ progenitors ^{56}Ni-decay products enhance the nucleation rates of silicates in the inner zones. This effect was not as strong in the 15 $M_\odot$ progenitor (see Fig. 5,7 in Sarangi & Cherchneff (2015)), and subsequently this mechanism becomes less dominant at higher explosive energies. Our lowest-mass progenitor is 15 $M_\odot$, and including ^{56}Ni-decay products would potentially modify the silicate yields and sizes of the those progenitors. At larger progenitor sizes (our 20 $M_\odot$, 25 $M_\odot$ models) ^{56}Ni-decay, while important, will likely not impact the results we present.

We would also like to make a few comments about the 25 $M_\odot$ progenitor models. The explosion data indicate that the reverse shock that occurs within the deepest layers of the ejecta at early times ($t \lessapprox 60\ days$) is weak and may not sufficiently reheat the innermost zones of the star, stalling near the proto-neutron star for some of these models. The inner layers between the stalled early reverse shock and the silicon layer of the ejecta cool at a similar rate to the outer layers of the ejecta, allowing for earlier than expected dust formation deep in the ejecta.

While we have not directly included radioactive heating from the $^{56}\mathrm{Ni} \rightarrow {}^{56}\mathrm{Co} \rightarrow {}^{56}\mathrm{Fe}$ decay chain, this heating source may alter the bulk dust formation time in the silicon layer of the ejecta. This heating may affect the timing of dust formation, as well as the size of grains that condense for every progenitor set. Inclusion of radioactive decay heating would require radiative transport for realistic, high-fidelity modeling (Sluder et al., 2018), however, this is in general difficult to do and is beyond the scope of this study. Despite this, approximations for radioactive decay heating can at least be introduced and will be included in future studies.

While not presented here, a series of simulations were performed modeling the radioactive decay chains of all unstable isotopes in the ejecta without heating or dust formation enabled. The results of these decay simulations indicated that the primary sources of dust in our models, silicate, carbonaceous, alumina, and (to a lesser extent) other oxide grains will generally be unaffected by changes in elemental abundances. One point to raise is that the production of Fe-group grains will be affected, primarily due to radioactive nickel and cobalt decaying into stable iron isotopes, increasing the abundance of free iron gas in regions with low concentrations of oxygen. The growth of iron and iron sulfide grains will likely be enhanced in these regions.

Furthermore, are our reported grain sizes realistic? A supporting example is Figure 3 of Gall et al. (2014) where it is reported that only grain size distributions with grain radii larger than 0.25 µm, with a lower limit of 0.7 µm, can reproduce observed supernova extinction curves (Zubko et al., 2004; Brandt & Draine, 2012). In general, our grain radii span from 1 to 10 µm for grains composing the majority of the dust mass fraction. This is in relatively good agreement for the early-time dust formation estimates based on reported observations for SN 2010jl. An improved physics model, including more advanced gas chemistry and chemical kinetics, could potentially improve this agreement.

Additionally, modeling weathering and shock destruction represent a more accurate representation of the grain size distribution. Early reverse shocks from gradients in the ejecta destroy small, early-forming grains. Shocks erode large grains and destroy smaller grains, shifting the size distribution toward smaller, more populous grains. Currently we are implementing sputtering and weathering of dust grains from ions in the ejecta, along with erosion and destruction from the shock fronts. These improvements are in development, along with implementing additional chemical processes such as coagulation and gas-added functionality is in preparation.

This project was conceived to explore qualitative implications of dust formation across a wide set of initial conditions in CCSNe rather than to offer precise quantitative end-to-end high fidelity for any specific CCSN environment. We do make comparison of some of our models to recent observational and computational studies; however, the particular qualities of our CCSNe limit the scope of this comparison. However, we do not find our results to be significantly dissimilar from other works in the literature (Sarangi & Cherchneff, 2013; Sarangi & Cherchneff, 2015; Biscaro & Cherchneff, 2016), which encourages us that we can indeed make some inferences from that data. This first-pass, large-scale parameter study should help to better inform future research campaigns for dust formation in SN ejecta.

2.5.3. Applications

Beyond studying the dust production as a function of energy, our broad set of explosion energies can be combined to study asymmetric explosions in a first-pass approximation. Here we approximate the asymmetries by assuming that an asymmetric explosion can be represented by the sum of fractions of one-dimensional explosions at different energies. For example, hypernovae (HNe) can be represented by a portion of the ejecta represented by a strong explosion (along the jet axis), with the rest at a normal explosion energy. In this section, we apply our models to a range of explosion scenarios of well-studied SNe and SN remnants to HNe.

For a first application, we review observations of SN 1987A arguing that this SN was not spherical. The red-shifted gammaray and iron line features (Hungerford et al., 2005) are best fit by an explosion that has a single outflow that is much stronger than the rest of the ejecta. By studying a range of stellar masses and combined components, we can study the expected variations in dust production for an asymmetric SN (see Table 2.2). Although the explosion energy is nearly the same for each of these models, varying the different component energies can vary the dust production by nearly a factor of 2. In our preliminary study, the best-fitting model is our more extreme energy 20 $M_\odot$ model.

The Cassiopeia A remnant is more complex where observations of the innermost ejecta show multiple lobes (Grefenstette et al., 2014). We mimic it by considering a series of explosive features covering a range of escape velocities from 0.5 to 5 times the symmetric velocity, corresponding to a range of ejecta energies of 0.25-25 foe from our database. Our set of explosion energies and the dust production for our simple Cassiopeia A model is shown in Table 2.2. It can be seen that our simulated results are in close agreement to Biscaro & Cherchneff (2016) for total, carbonaceous, and forsterite dust masses by at most a factor of two, with alumina production greater by almost a factor of 10 for our results. However, our results are reported at a time stamp of nearly 3000 days with a simplified general physics implementation. The reported observational results of Priestley et al. (2019); De Looze et al. (2017) are greater by 1-2 orders of magnitude. The effect of HN explosions is much greater. Here we assume bimodal explosions where we have a very strong component along the axis. These strong explosions produce very different dust signatures than normal SNe (Table 2.2).

Table 2.2. Comparisons to Observed Dust in Supernova Ejecta and Remnants

SNe Designation	$M_{total\ dust}$ $M_\odot$	$M_{C(s)}$ $M_\odot$	$M_{Mg_2SiO_4(s)}$ $M_\odot$	$M_{Al_2O_3(s)}$ $M_\odot$	$E_{out-of-cone}$ foe	$E_{in-cone}$ foe
aSN^a 15$M_\odot$	2.43×10^{-2}	6.05×10^{-3}	1.44×10^{-2}	2.00×10^{-3}	0.52	4.79
aSN^a 20$M_\odot$	3.75×10^{-2}	2.36×10^{-2}	1.02×10^{-2}	1.01×10^{-3}	0.53	$\frac{1}{2}4.33$ $\frac{1}{2}5.03$
aSN^b 15$M_\odot$	4.79×10^{-2}	4.32×10^{-2}	3.85×10^{-3}	5.46×10^{-4}	0.92	3.42
aSN^b 20$M_\odot$	3.55×10^{-2}	2.37×10^{-2}	4.53×10^{-3}	6.65×10^{-3}	$\frac{1}{2}$(0.84,1.0)	$\frac{2}{5}2.85$ $\frac{3}{5}4.15$
aSN^c 20$M_\odot$	2.45×10^{-2}	2.36×10^{-2}	6.53×10^{-4}	1.68×10^{-4}	0.53	18.1
Ref. 20$M_\odot$	3.78×10^{-2}	2.37×10^{-2}	4.44×10^{-3}	9.61×10^{-3}	1.00	-
1987A†	3.00×10^{-3}	$\geq 2.25 \times 10^{-3}$	$\leq 7.5 \times 10^{-4}$	-	-	-
HNe^d 25$M_\odot$	7.28×10^{-1}	1.37×10^{-2}	2.46×10^{-1}	5.51×10^{-2}	4.72	14.80
HNe^e 25$M_\odot$	4.71×10^{-1}	1.38×10^{-2}	1.59×10^{-1}	1.88×10^{-2}	4.73	18.40
HNe^f 25$M_\odot$	5.64×10^{-1}	1.38×10^{-2}	1.83×10^{-1}	3.73×10^{-2}	0.92	18.40
Ref. 25$M_\odot$	4.87×10^{-1}	1.38×10^{-2}	1.85×10^{-1}	2.04×10^{-2}	$\frac{3}{4}4.73, \frac{1}{4}6.17$	-
Cas A (20$M_\odot$)	3.13×10^{-2}	2.06×10^{-2}	5.89×10^{-3}	3.91×10^{-3}	0.53, 0.81, 1.0, 1.19, 5.03, 18.1	-
Cas A††	7.0×10^{-1}	$\leq 1.5 \times 10^{-1}$	6.0×10^{-1}	-	-	-
Cas A‡	3.2×10^{-2}	7.1×10^{-3}	1.1×10^{-2}	1.4×10^{-2}	-	-
Cas A‡‡	8.0×10^{-1}	0.00	8.0×10^{-1}	0.00	-	-

Table 2.2 (cont'd)

SNe Designation	$M_{total\ dust}$ $M_\odot$	$M_{C(s)}$ $M_\odot$	$M_{Mg_2SiO_4(s)}$ $M_\odot$	$M_{Al_2O_3(s)}$ $M_\odot$	$E_{out-of-cone}$ foe	$E_{in-cone}$ foe

Note. — Comparisons with Observations and other simulation results. The out-of-cone, $E_{outofcone}$, and in-cone, $E_{outofcone}$, energies correspond to the explosion energies of the models used for these dust mass estimations of aSNe, HNe, and Cas A like comparisons using our database. We give the total dust mass, $M_{total\ dust}$, carbonaceous dust mass, $M_{C(s)}$, forsterite dust mass, $M_{Mg_2SiO_4(s)}$, and alumina dust mass $M_{Al_2O_3(s)}$ to compare to some of the higher yield grains seen in both observations and simulations. It should be noted that we are using data evolved out to 1157 days.

[†] Observed dust mass at 1153 days, Wesson et al. (2015).

[††] Observed, Priestley et al. (2019).

[‡] Simulated, 4000 days, Biscaro & Cherchneff (2016).

[‡‡] De Looze et al. (2017).

[a] Parameter fit f=3,Θ=40, Hungerford et al. (2005).

[b] Parameter fit f=2,Θ=20, Hungerford et al. (2005).

[c] Parameter fit f=5,Θ=20, Hungerford et al. (2005).

[d] Θ=15, [e] Θ=10, [f] Θ=40

These studies also allow us to predict the evolution of dust production at high redshift. There is evidence that the critical proto-stellar cloud mass increases at lower metallicities (for a review, see Bromm, 2013; Rosen & Krumholz, 2020), causing the initial mass function (IMF) to flatten out. At the low metallicities expected at high redshift, these massive stars will produce more pair instability and HNe. HNe, energetic and asymmetric SN explosions (Iwamoto et al., 1999), are believed to be produced by rotating collapsing stars forming black holes. The subsequent accretion disk produces strong asymmetric explosions. Not only do these explosions produce nucleosynthetic yields that are different from those of normal SNe, but, as we see from our models, they also produce different dust signatures. If the IMF flattens out at high redshift, these HNe could dominate the number of explosions from massive stars, and observations of the dust at high redshift could constrain the amount of flattening in the IMF.

The dust production depends on both the stellar mass and explosion energy, and the flattening of the IMF can alter both of these. Using the models for IMF evolution from Fryer et al. (in preparation) and our dust yields, we are able to estimate the dust production with decreasing metallicity or increasing redshift. Figure 2.12 shows the variation in the dust production with decreasing metallicity for a variety of evolutionary models for the IMF. The increase of massive stars and HNe increases the production of dust. Comparing these model observations (Nanni et al., 2020) could be used to help constrain the IMF. The pair instability fraction will also increase at low metallicity. We have not included the production from these explosions in this study.

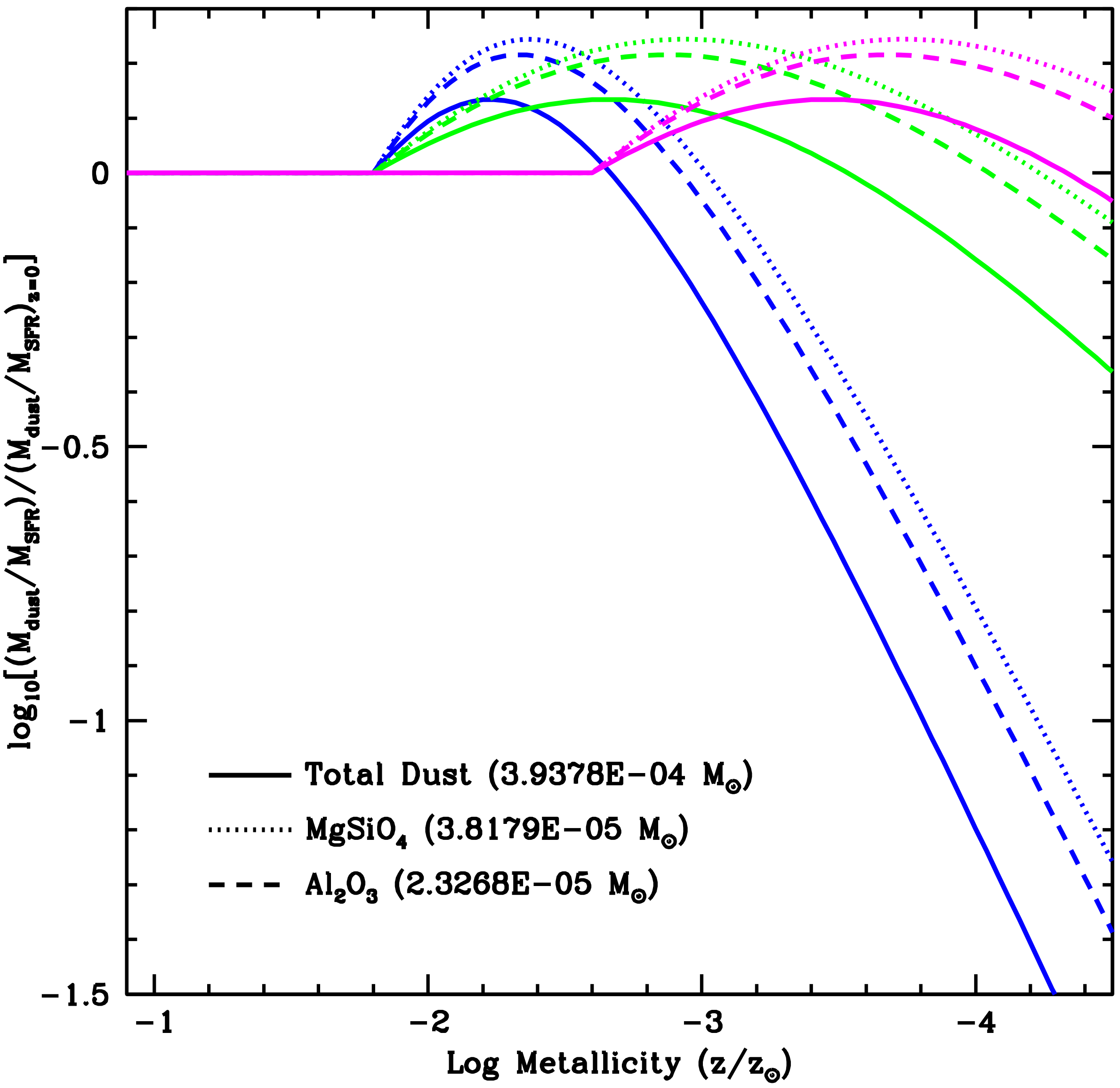

Figure 2.12: Dust production (relative to the redshift 0, solar metallicity dust production) versus metallicity for three different evolutionary models for the initial mass function. In these models, we vary the onset of the flattening of the IMF from an early evolution starting at a metallicity of 2.5% solar (roughly a redshift of 5) and late evolution at 0.3% solar metallicity (roughly a redshift of 7). For our early evolution models, we include two scenarios where the initial mass function flattens at two different rates. These models are designed to show a range of possible dust evolution scenarios. The solid, dotted and dashed curves correspond to the total, $MgSiO_4$ and Al_2O_3 dust production.

CHAPTER 3

Code Developement: `nudust` & `nudustc++`

`nudust` is the first iteration of our dust modeling codes (Brooker et al., 2021; Mauney & Stangl, 2022). It was used in the simulations of grain nucleation in the previous chapter, Chapter 2. Written in Python, it solves a system of non-linear ordinary differential equations with LSODA, an integration method that switches between the non-stiff Adams method and the stiff BDF method. Vectorization and off-loading is done using `Numba`, a library for the just-in-time (JIT) compilation of NumPy routines. Each cell in the model is self-contained and independent of its neighbors, making it highly parallelizable. Using the Python library multiprocessing POOL, nucleation calculations for each cell are started on the specified number of processors, allowing for transitions from single-process execution to large-scale parallel execution.

In order to implement destruction and sputtering calculations into `nudust`, an increase in performance was needed. After reaching the full capabilities of Python and Numba, further speedup was needed. `nudust` was rewritten in `C++` which resulted in `nudustc++`, the nucleating dust code in `C++` (Stangl, 2023). The parallelization is done using MPI and OpenMP. The calculation path is highly customizable. Users can easily change the integrator and interpolator, along with specifying the shock detection methods, the dust grain size distribution, the chemical network, and the ability to turn on/off nucleation or destruction calculations.

Original Manuscript from:

Stangl et al. (2024)

nudustc++ : C++ Code for Modeling Dust Nucleation and Destruction in Gaseous Systems

The Journal of Open Source Software (Submitted)

3.1. Summary

We introduce `nudustc++`, a **nu**cleating **dust** code in **C++** modeling dust grain formation, growth, and erosion in gaseous systems. `nudustc++` is a highly parallelizable set of code and tools for solving a system of nonlinear ordinary differential equations describing dust nucleation, growth, and erosion for user-specified grain species. It leverages OpenMP and MPI to optimize threading and distribution on available CPUs.

3.2. Statement of Need

Understanding interstellar dust is crucial for astronomical observations (Draine, 2003), offering key insights into stellar processes. These grains absorb electromagnetic radiation, re-emitting it at longer wavelengths, leading to extinction and a spectral shift towards redder wavelengths. The size and composition of dust introduce variability in opacities and distortion of incident light, resulting in molecular lines and altering the resulting data. Dust forms in asymptotic giant branch (AGB) stars, on pre-existing grains in the interstellar medium (ISM), and within the expanding, cooling ejecta of core collapse supernovae explosions (CCSNe); these grains preserve important information about the nucleosynthetic processes within their host environment, locking up their unique isotopic signatures. However, despite their importance, the quantity, composition, and size distribution of dust formed in supernovae and deposited into the ISM remain poorly constrained.

Models of the formation, growth, and weathering of dust are necessary to understand the origin and characteristics of dust in the interstellar medium, shedding light on where and what dust grains are possible in these environments. Specifically, modeling the formation and survivability of dust in CCSNe produces a population of dust grains that can be compared with observations, allowing verification of our current understanding of physical models: ISM dust origin, chemical networks, nucleation models, hydrodynamics, supernovae engines, progenitor structure, erosion physics, and stellar compositions.

This project originated from the need to track dust nucleation and destruction in Core-Collapse Supernovae Explosions. It addresses the lack of sub-grid physics associated with phase transitions, where the hydrodynamical time steps are an order of magnitude larger than those needed to capture gas vapor physics. A smaller, more refined grid with chemical networks and smaller time steps is needed. The code is structured to intake any hydro-dynamical temperature-density trajectory with vapor compositions. This allows `nudustc++` to track dust in a large range of environments: planetary atmospheres, nebulae, hydro-aerosol formations, explosions, etc. Additionally, if a time-series hydro-dynamical profile is unavailable but a dust size distribution and a profile snapshot are, `nudustc++` can calculate the evolution and survivability of the dust. The applications of `nudustc++` extend beyond Supernovae and Astronomy to include any model with thermodynamic and statistical physics.

3.3. State of the Field

In order to gain a deeper understanding of the origin and characteristics of dust in the interstellar medium, it is imperative to develop models that include the nucleation, chemistry, growth, and erosion of dust. Current methods of calculating dust formation and survival include Classical Nucleation Theory (CNT) and Kinetic Nucleation Theory (KNT).

CNT treats grain formation as a barrier-crossing problem. As atoms stick to a cluster, the free energy increases. After reaching a critical size, the free energy decreases as atoms are added. It tracks the nucleation rate by assuming a steady state between monomer attachment and detachment. However, it neglects chemical reactions of formation, destruction, growth by coagulation, and treats the grains as bulk materials. Due to these simplified assumptions, CNT is widely used, but is increasingly less so due to these limitations. Kozasa & Hasegawa (1987) and Bianchi & Schneider (2007) used CNT to model dust grain formation in SN 1987A and SN 1987A-like Supernovae. Todini & Ferrara (2001) used CNT to calculate dust formation in Core Collapse Supernovae Explosions. More recently, Paquette et al. (2023) used CNT to model dust formation in the outflows of AGB stars.

KNT tracks the number densities of clusters with more than two atoms, treating them as particles that grow as spheres. It uses size-dependent grain properties in place of bulk material properties. Grains grow by accreting atoms (condensation) through kinetic theory. Grains lose atoms through erosion (destruction) using the principle of detailed balance. While KNT does not assume a steady state between condensation and destruction, it still doesn't take into account the chemical reactions undergone or growth through coagulation. Nozawa et al. (2003) used KNT to model the nucleation and growth of dust in early Population III star supernovae. Nozawa et al. (2006) included destruction to model the effects of high-velocity shock waves on dust. Fallest (2012) predicts dust mass yields in CCSNe using KNT.

Other publicly available dust codes include `nudust`, `starchem`, `DustPy` and `astrochem`. `nudust` is described in Brooker et al. (2022) and is a post-processing dust nucleation code using KNT. `starchem` tracks the chemical network in stellar environments (Christopher Mauney, 2017). `DustPy` is a Python package used to model dust evolution in proto-planetary disks (Stammler & Birnstiel, 2022). `astrochem` computes the chemical abundances and includes gas-dust interactions in astronomical environments such as the interstellar medium, diffuse clouds, and proto-stars (Maret & Bergin, 2015).

3.4. Design Principles and Salient Features

`nudustc++` is designed as a flexible, multi-use post-processing code. It is designed to take user supplied data in ascii, binary, or text format, including initial conditions, environment variables, and dust formation networks, and calculate a solution vector. We use an initial composition and interpolated user input data to construct a rate-of-change vector supplied to an implicit integrator in each cell. The user can easily change and modify the interpolator and integrator. Three main configuration paths are currently implemented: destruction only, destruction with nucleation and growth, and nucleation and growth. This allows the reduction of total computations by removing from the solution vector parameters modeling quantities not needed for the calculation path. Output data can be written to ascci, binary, or text files.

Because of the post-processing nature of `nudustc++`, modeling grain nucleation and destruction is possible in a large range of physical environments. The user provides the hydrodynamical trajectory file and vapor compositions, which can describe Supernovae explosions to planetary atmospheres to interstellar gas clouds and any temperature-density profile extended beyond astrophysics.

Because `nudustc++` is a post-processing code where data is read in separately for each cell with no data flow between cells, there is no shared memory and each cell can be computed independently. This results in an embarrassingly parallel process, allowing for simultaneous computation of each cell and thereby reducing runtime.

3.5. Performance and Accuracy

Figure 3.1 shows a comparison between the Python `nudust` using an implicit integrator versus `nudustc++` using an explicit integrator. At shorter solution lengths, the implicit integrator has a lot of overhead, leading to an increased run time despite the shorter length. The explicit integrator in `C++` outperforms the implicit integrator even at longer solution lengths. Overall, `nudustc++` outperforms the Python version. It is also embarrassingly parallel. Utilizing OpenMP and MPI, the code can run cells in parallel.

3.6. Applications

In addition to nucleation, `nudustc++` includes an analysis of the sputtering and erosion of dust grains. It is used in Chapter 4 to calculate the erosion of dust grains in CCSNe. Chapter 4 takes the nucleated dust data from Chapter 2 and applies a reverse shock to determine the survivability of the dust grains. Further details of the sputtering methods used are discussed in Chapter 4.

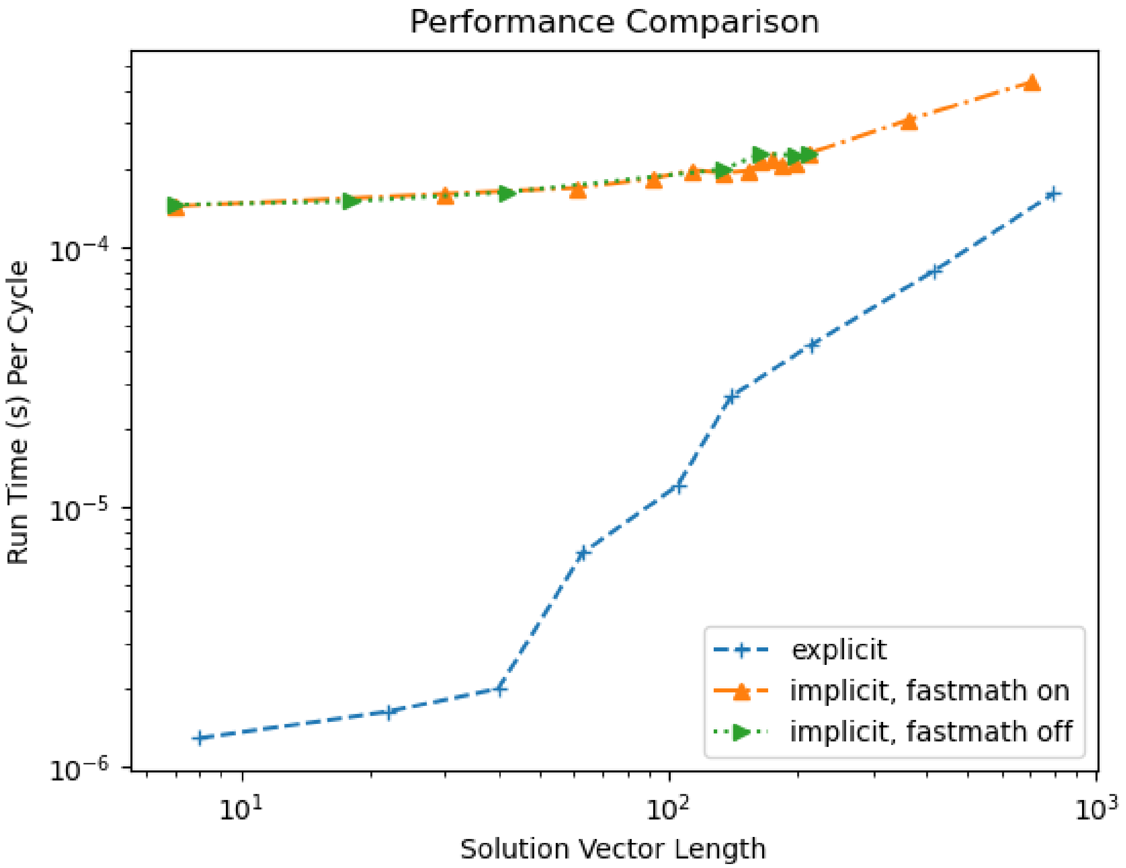

Figure 3.1: A comparison of the performance between `nudustc++` (explicit) and `snDust` (implicit) with varying solution arrays. `snDust`, implicit integration, has a large amount of overhead at shorter solution lengths leading to a longer runtime. `nudustc++`, explicit integration, performs faster at all solution lengths.

Chapter 4

Grain Destruction: Sputtering & Erosion

Original Manuscript from:
Stangl et al. 2024
Dependence of Dust Formation on the Supernova Explosion II: Dust Destruction
The Astrophysical Journal (in preparation)

4.1. Abstract

We investigate the dependence of the core-collapse supernovae (CCSNe) progenitor mass on the survivability of dust grains with 15, 20, and 25 $M_\odot$ progenitor masses. The explosion ejecta evolution is modeled with a 1-D Lagrangian code until the reverse shock has passed through the ejecta. A size distribution resulting from a multigrain dust nucleation and growth model (Brooker et al., 2022) is applied. Each model then experiences a shockwave with a temperature varying from 10^3-10^{11} K and a velocity of 10^2-10^9 Km/s. The survival rate of dust is calculated for each temperature and velocity of shocks.

4.2. Introduction

Interstellar dust, comprising only ≈1-2% of interstellar mass, significantly influences the thermal, chemical, and dynamical properties of the Interstellar Medium (ISM). Dust filters light, absorbing ultraviolet and visible radiation and re-emitting it in the infrared spectrum, thereby facilitating the cooling of the interstellar medium (ISM). Composed primarily of carbonaceous and silicate grains, interstellar dust refractory cores originate from the cooling ejecta of Core-Collapse Supernovae (CCSN) and in the cool extended envelope of Asymptotic Giant Branch (AGB) and Red Giant (RGB) stars, where high densities and low temperatures allow dust grains to condense and nucleate. These grains are injected into the ISM where they are further processed. Existing dust grains can accrete material, growing an icy mantel, and interact with cosmic rays to desorb material and form multiple grains.

Large amounts of dust (10^7 $M_\odot$) have been observed at high redshifts (Bertoldi et al., 2003; Watson et al., 2015) where AGB stars have not yet had enough time to evolve to form dust, suggest CCSNe as the source for this early dust (Sadavoy et al., 2019). Dust has been observed in SN remnants such as SN 1987A and Cas A (Dwek & Arendt, 2015; Indebetouw et al., 2014; Matsuura et al., 2019; Arendt et al., 2014; Priestley et al., 2019). Detailed analysis has confirmed the presence of supernova-derived dust in meteorites, characterized by presolar isotopic signatures and distinctive species (ex. TiC, $\mathrm{Al_2O_3}$, etc.) (Clayton & Nittler, 2004). CCSNe are sites of dust formation but also subject this dust to sputtering and erosive effects. Energetic particles in the ejecta of CCSNe collide with dust grains, removing and eroding material from or the complete destruction of dust grain. The amount of dust destruction depends on the composition, size, and amount of dust along with the energy and density of the ejecta and CCSNe reverse-shock waves.

Evidence of dust production and destruction has been observed in SN Remnants (SNR). SN 1987A is a young SNR and the first SN in which dust formation was directly observed. Early observation, at 615 days after explosion, identified thermal emission consistent with dust formation (Danziger et al., 1989; Wooden et al., 1993). The blue shift of optical lines further suggested this dust condensed in the CCSNeejecta (Lucy et al., 1989). Later observations show an increase of dust mass from 10^{-4} $M_\odot$ at 775 days (Wooden et al., 1993) to a dust mass of 0.5 $M_\odot$ at 8500-9000 days (Matsuura et al., 2011). This increase in observed dust suggests either an initially undetected large amount of optically thick dust (Dwek & Arendt, 2015) or an increase of dust mass through grain growth (Wesson et al., 2015). Currently, the reverse shock has not interacted with the newly formed dust in the ejecta, but has interacted with and eroded the dust in the equatorial rings (Dwek et al., 2008). Dust grains have also been observed to survive and grow after the forward shock of 1987A with an increased dust mass of 3-7$\times10^{-4}$ $M_\odot$ from grain growth or re-formed dust (Matsuura et al., 2019). Cas A, an approximately 340 year-old SNR (Fesen et al., 2006; Krause et al., 2008), has regions of reverse shocked and unshocked dust. De Looze et al. (2017) estimate the dust to be 0.3-0.5 $M_\odot$ of silicate or 0.4-0.6 $M_\odot$ of silicate and carbide grains. The dust mass in the cold, unshocked region is larger than in the shocked region, suggesting a dust destruction rate of $\approx$70% (De Looze et al., 2017).

Despite the significance of sputtering and erosion on the total dust surviving a CCSN to be injected into the ISM, dust destruction and its efficiency are not well understood. Challenges in accurate observations of dust amounts and survival rates are due to the difficulty in accounting for contamination from ISM and galactic dust along the line of sight and with difficulties in modeling the infra-red dust emission to determine dust compositions, masses, and size distributions (Savage & Sembach, 1996; Draine, 1981; Dwek et al., 1996; Draine, 2011; Williams & Temim, 2016). Estimating destruction rates from infrared dust emission with shock modified size distributions vary from 35-40% in LMC SNRs (Borkowski et al., 2006), 35% in the Cygnus Loop (Sankrit et al., 2010), 10-85% in SN Ia SNR Kepler (Blair et al., 2007), and 27-50% in LMC CCSNe (Williams et al., 2006).

Difficulties in calculating the dust survival arise from limitations on available sputtering data of these materials in the extreme environments of CCSNe, difficulties modeling the structure and evolution of CCSNe, and establishing progenitor scenarios with abundances and circum-stellar material. The amount of dust surviving the CCSNe reverse shock and injection into the ISM is not well constrained and depends heavily on the surrounding environment. The composition of the ejecta determines what ions bombard the grains, the temperature determines which mechanism more effectively erodes the grains, and the type of shock determines what erosion process is more efficient and how long the erosion effects occur before the relative velocity between the gas and dust is negligible. Dwek (2005) assumes the ejecta expands homogeneously in a uniform medium. However, the ejecta is observed to be clumpy and contain a large portion of the dust. The clumps reduce the reverse shock more than the surrounding low-density regions, creating a more complicated reverse shock structure. Nozawa et al. (2007); Nozawa et al. (2010) examine dust formed in Population III CCSNe, pain-instability SNe, and stripped envelope CCSNe. The temperature and density of the ejecta is evolved out to late times, 10^5-10^6 years. The dust destruction is calculated based on the temperature-density profiles. Biscaro & Cherchneff (2016) study in detail the destructive process in Cas A. They assume grain size distributions based on previous observations of IIb SNe. They calculate the survival rate of different levels of knot clumpiness and varied values of the reverse shock temperature and velocity while considering solely sputtering and solely non-thermal sputtering.

This work is a continuation of Brooker et al. (2022) and extends the study to include the erosive and destructive effects of the reverse shock on the previously formed dust grains. In our previous paper Brooker et al. (2022), we used a theoretical approach to model the dust condensation, formation, and growth in a suite of CCSNe models evolved out to a minimum of 1157 days. The models vary across a large parameter space: progenitor masses of 15, 20, & 25 $M_\odot$, explosion energy of 0.3-124$\times 10^{51}$ ergs, nucleosynthetic isotopic yields, various composition profiles, and different engine models. In this study, we analyze how different characteristics of the CCSNe affect the survivability of dust produced in the explosion. We study the effects of a range of shock velocities, 10^3-10^{10} cm/s, shock temperatures, 10^3-10^{11} K, and the progenitor model on the survivability of dust grains. We use a wide range of CCSNe models and shock characteristics to provide a suite of evolved explosions and resultant dust populations. We use these results to identify dust survivability trends and to provide a wide range of explosions and dust compositions to compare with observed CCSNeto determine dust abundances in the ISM.

The paper is structured as follows. In Section 4.3 we describe methods used to model sputtering. In Section 4.6 we present our results of the pre-reverse shock, initial size distributions and the size distributions post reverse shock. We discuss our conclusions and the observational impacts of our results in Section 4.7.

4.3. Methods

To model dust destruction in CCSNe ejecta, we evolve out the ejecta of Brooker et al. (2022) and apply a reverse shock. A suite of 72 1D CCSNe explosion models from Fryer et al. (2018); Andrews et al. (2020) are re-gridded onto a Lagrangian mesh with the removal of the compact core and a stellar wind profile is added following Villata (1992). The ejecta is evolved out to 1157 days following a simplified version of Fryer et al. (2018); Andrews et al. (2020) without neutrino transport or equations of state for dense matter. The ejecta tmperature-densitiy trajectories are post processed to simulate dust nucleation and growth following a revised formulation of Kinetic Nucleation Theory given by Nozawa & Kozasa (2013). These used to evolve the ejecta and model dust formation are described in greater detail in Brooker et al. (2022).

4.4. Late Time Evolution

Following the CCSNe and hydrodynamical methods used in Brooker et al. (2022), after bulk nucleation ceases after $\approx$ 1157 days, we assume the ejecta follows homologous expansion. We calculate the temperature and density of each model at 100 years after explosion by,

$$T(M_r, t) = T(M_r, t_0) \left(\frac{t}{t_0} \right)^{3(1-\gamma)} \tag{4.1}$$

and

$$\rho(M_r, t) = \rho(M_r, t_0) \left(\frac{t}{t_0} \right)^{-3} \tag{4.2}$$

where $T(M_r, t_0)$ and $\rho(M_r, t_0)$ are the last temperature and density values for each cell from the last time step, t_0, of the hydro data from Brooker et al. (2022), t is the time, M_r refers to the mass of the cell at the radius r, and $gamma$ is the ratio of specific heats, here we use ideal gas $5/3$.

We then inject a reverse shock into each cell at the selected time. A density scaling factor for pile up from the shock is adjustable for each cell. We use a value of 10, an increase in density of 10 times to account for pile up from the passing of the shock. The shock velocity and temperature is varied from 10^3-10^9 cm/s and 10^3-10^9 K to produce a suite of shocks.

Current work is being done to simulate a more physical, representative shock. The hydrodynamical simulations are restarted with a right reflective zone boundary. As the ejecta expands and hits the right boundary, a reverse shock is generated as the ejecta interacts with surrounding density gradients.

4.4.1. Grain Destruction

Once a dust grain has nucleated, it is susceptible to erosion through thermal and non-thermal sputtering. Thermal sputtering occurs when the surrounding hot plasma moving with the dust grain interacts with and bombards the grain. The source of non-thermal sputtering is the velocity-driven collisions between dust grains (*target*) and gas atoms (*impactor*). This primarily occurs at the point where the ejecta begins to interact with the ISM, producing a non-radiative reverse shock that propagates into the ejecta shell. These two sources of destructive interactions result in the sputtering of atoms off of the surfaces of dust grains, thereby eroding or destroying them.

We adopt the grain destruction model described in Biscaro & Cherchneff (2016) and based on models used by Nozawa et al. (2006), Nozawa et al. (2007), and Slavin et al. (2015). The erosion rate, $\frac{da_j}{dt}$, of grain species j with radius a is given as (Draine & Salpeter, 1979a; Dwek et al., 1996)

$$\frac{1}{n_{gas}}\left(\frac{da_j}{dt}\right) = -\frac{m_{sp}}{2\rho_d}\sum_{i}^{N_{species}} A_i \left(\frac{8kT}{\pi m_i}\right)^{1/2} \frac{e^{-s_i}}{2s_i}\int_{\epsilon_{th}}^{+\infty} \sqrt{\epsilon_i}e^{-\epsilon_i} sinh(2s_i\sqrt{\epsilon_i})Y_i(E=\epsilon_i kT)d\epsilon_i. \tag{4.3}$$

where n_{gas} is the number density of the gases, m_{sp} is the average mass sputtered off a grain in a collision, ρ_d is the bulk density of the grain, $N_{species}$ is the number of gas species, A_i is the **check is mass or number** abundance of gas species i, k is the Boltzmann constant, T is the gas temperature, m_i is the mass of the impactor, the quantity s_i is the ratio of the kinetic energy to the scaling factor kT and is expressed in Equation 4.4, ϵ_{th} is the ratio of the threshold energy E_{th}/kT, ϵ_i is the ratio of incident projectile energy E_i/kT, and Y_i is the yield or the dimensionless number of sputtered atoms with impacting gas i described in Equation 4.7.

The sputtering yield in the integrand is dependent on E (Dwek et al., 1996) rather than ϵ_i as given in Biscaro & Cherchneff (2016) and Nozawa et al. (2006). Additionally, the quantity s_i is given as,

$$s_i^2 = \frac{m_i v_d^2}{2kT} \tag{4.4}$$

with the limit $s_i \rightarrow \infty$ leading to Equation (4.5) and the limit of $s_i \rightarrow 0$ leading to Equation 4.6 (Draine & Salpeter, 1979a). At higher kinetic energies, $s_i \rightarrow \infty$, non-thermal sputtering dominates. While at lower kinetic energies, $s_i \rightarrow 0$, thermal sputtering dominates.

The erosion of a grain species *j* due to pure non-thermal sputtering is given by,

$$\frac{1}{n_{gas}}\left(\frac{da_j}{dt}\right)_{NTS} = -\frac{m_{sp}v_d}{2\rho_d}\sum_{i}^{N_{species}} A_i Y_i(E=0.5 m_i v_d^2), \tag{4.5}$$

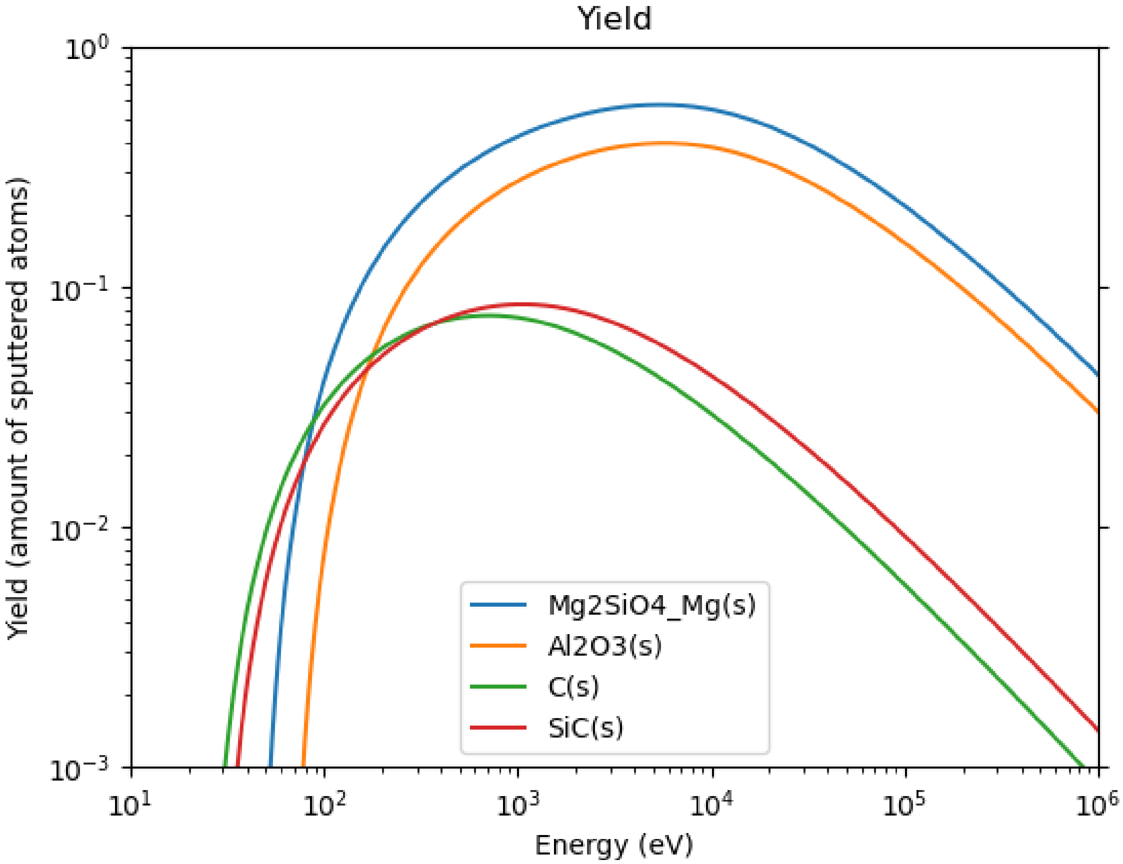

Figure 4.1: Sputtering yields of carbides and oxides. The carbides experience less sputtering of material than oxides. The oxides are sputtered by O^+ and the carbides by He^+.

the subscript NTS refers to Non-Thermal Sputtering. The erosion due to pure thermal sputtering is given by,

$$\frac{1}{n_{gas}}\left(\frac{da_j}{dt}\right)_{TS} = -\frac{m_{sp}}{2\rho_d}\sum_i^{N_{species}} A_i\left(\frac{8kT}{\pi m_i}\right)^{1/2}\int_{\epsilon_{th}}^{+\infty}\epsilon_i e^{-\epsilon_i}Y_i(\epsilon_i)d\epsilon_i. \tag{4.6}$$

where k is the Boltzmann constant, T is the gas temperature. The subscript TS refers to Thermal Sputtering.

4.4.2. Dust Sputtering Yields

The grain erosion rates are dependent on the sputtering yield, corresponding to the average number of sputtered atoms on the target dust grain per incident impacting atom or ion (Biscaro & Cherchneff, 2016) using the collision cascade theory described by Sigmund (1981). Using the common formalism and definition of backward sputtering yield at normal incidence, denoted as $Y_i(E)$ in Equation 4.6, from projectile *i* impacting a target atom on a dust grain surface with energy *E* described by Bohdansky (1984), we derive the sputtering yield equation (expressed in units of released atoms per ion),

$$Y_i(E) = 4.2\times 10^{14}\frac{S_i(E)}{U_0}\frac{\alpha_i(\mu_i)}{K\mu_i+1}\left[1-\left(\frac{E_{th}}{E}\right)^{2/3}\right]\left(1-\frac{E_{th}}{E}\right)^2, \tag{4.7}$$

. where U_0 is the surface binding energy (here, the sublimation energy is used (Behrisch & Eckstein, 2007)) in eV, the dimensionless term $\mu_i = M_d/M_i$ (M_d is the mass of the target grain and M_i is the mass of the incident particle, both in units of AMU), $\alpha_i(\mu_i)$ a dimensionless function dependent on μ_i, a free parameter K is used to adjust results to match experimental sputtering yield data, E_{th} the threshold energy required to induce sputtering, and the function for the nuclear-stopping cross-section $S_i(E)$ in units of $ergs\ cm^2$. We used the approximated threshold energies E_{th} described by Andersen & Bay (1981) and Bohdansky (1984),

$$E_{th} = \begin{cases}\frac{U_0}{g_i(1-g_i)} & \text{for } M_i/M_d \le 0.3\\ 8U_0\left(\frac{M_i}{M_d}\right)^{1/3} & \text{for } M_i/M_d > 0.3\end{cases}, \tag{4.8}$$

where $g_i = 4M_iM_d/(M_i+M_d)^2$ is the maximum fractional energy transfer in a head-on elastic collision. The nuclear-stopping cross-section $S_i(E)$ is described in Sigmund (1981) as,

$$S_i(E) = 4\pi a_{sc}Z_iZ_de^2\frac{M_i}{M_i+M_d}s_i(\epsilon_i). \tag{4.9}$$

where Z_i, Z_d are the atomic numbers of the incident ion and target grain, respectively, e is the elementary charge in CGS units, and a_{sc} is the screening length for the interaction potential between

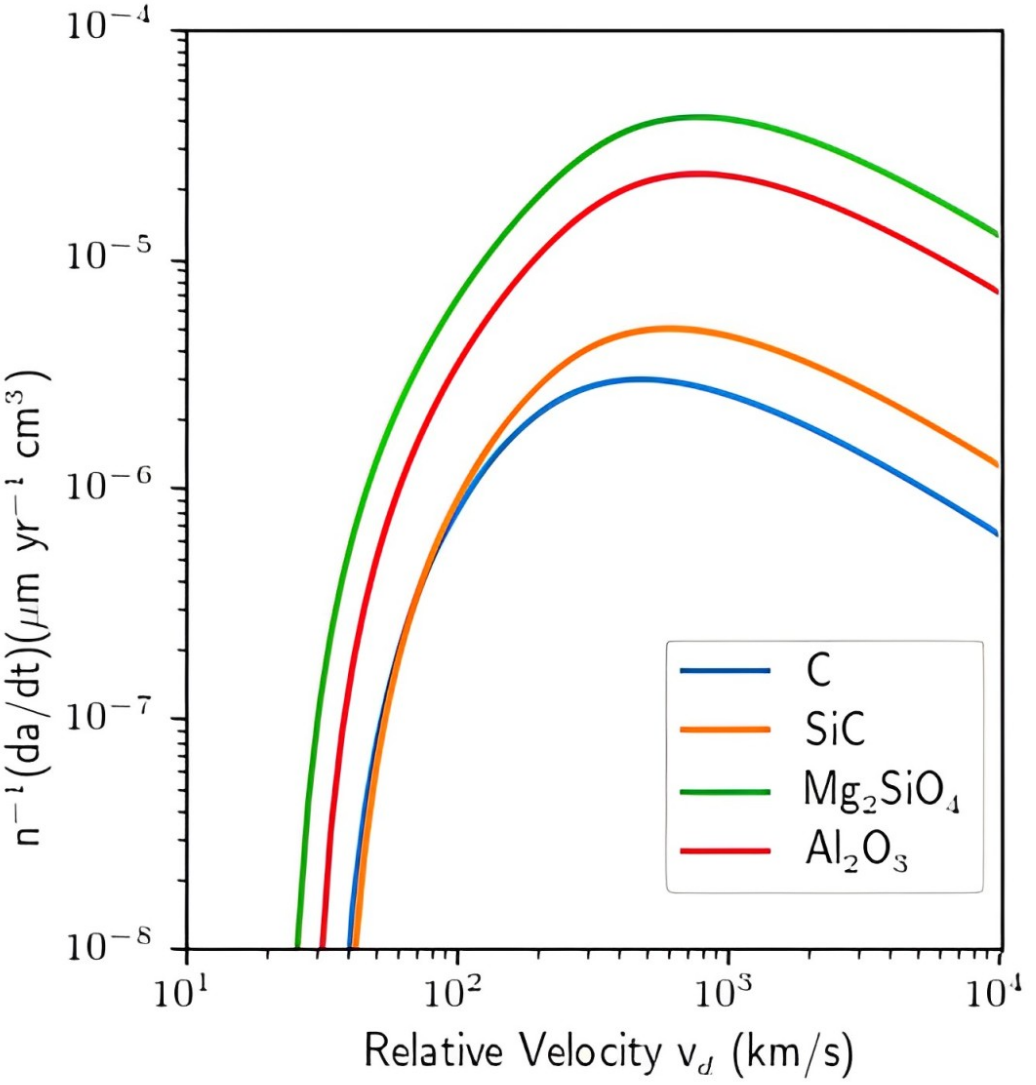

Figure 4.2: Non-thermal sputtering yields for oxides and carbides. The sputtering ions are representative of the layer the grain is produced in. The oxides are sputtered by O^+ and the carbides by He^+.

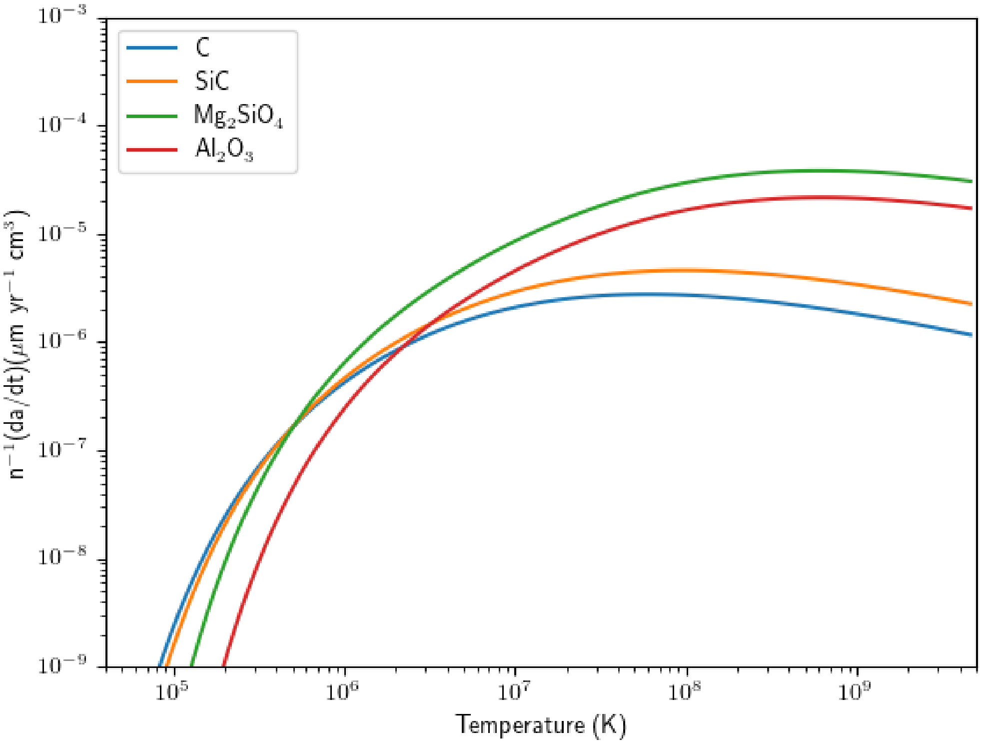

Figure 4.3: Thermal sputtering yields for oxides and carbides. The sputtering ions are representative of the layer the grain is produced in. The oxides are sputtered by O^+ and the carbides by He^+.

nuclei,

$$a_{sc} = 0.885 a_0 \left(Z_i^{2/3} + Z_d^{2/3} \right)^{-1/2}, \tag{4.10}$$

using the Bohr radius, $a_0 = 5.29 \times 10^{-9} cm$. The approximated function $s_i(\epsilon_i)$ is described by Matsunami et al. (1981),

$$s_i(\epsilon_i) = \frac{3.441\sqrt{\epsilon_i}\ln(\epsilon_i + 2.718)}{1 + 6.35\sqrt{\epsilon_i} + \epsilon_i(6.882\sqrt{\epsilon_i} - 1.708)}, \tag{4.11}$$

where ϵ_i is the reduced energy expression,

$$\epsilon_i = \frac{M_d}{M_i + M_d}\frac{a_{sc}}{Z_i Z_d e^2} E. \tag{4.12}$$

The value of $\alpha_i(\mu_i)$ depends on the approximation of the distribution of energy deposited in the target grain. From Biscaro & Cherchneff (2016), the expression of $\alpha_i(\mu_i)$ is given by,

$$\alpha_i(\mu_i) = \begin{cases} 0.2 & \text{for } \mu_i \leq 0.5 \\ 0.1\mu^{-1} + 0.25(\mu_i - 0.5)^2 & \text{for } 0.5 < \mu_i \leq 1 \\ 0.3(\mu_i - 0.6)^{2/3} & \text{for } 1 < \mu_i \end{cases}, \tag{4.13}$$

derived by Nozawa et al. (2006), starting from the first approximation made by Bohdansky (1984) and comparing sputtering data for $0.3 \leq \mu_i \leq 56$.

Finally, there is the free parameter K whose values are taken from a wide range of sources and used to adjust sputtering yields to fit available experimental data for various dust grain species. This is further explored in Biscaro & Cherchneff (2016) and references therein. The values of K we used for this paper can be found in Table 4.1 with accompanying sources.

4.4.2.1. Calculating Yield K values from Data

This study extends dust erosion to grains that haven't been studied in depth. Therefore, the fits needed for yield calculations, the K term, aren't widely known.

To determine the fitting parameter K, we used data from Rosenber & Wehner (1962). This data was fitted using SciPy's curve fit module, Equation (4.7) as the fitting function, and the K value as a free parameter. We saw that the yield results depended on the mass of the impacting ion. Figure 4.4 shows a fitted yield curve for H and He impactors on a Ni substrate. With a heavier impacting ion, a larger K value was needed. Since we tracked ions up to iron, we weighted the data of masses lower than iron more heavily when determining the K value.

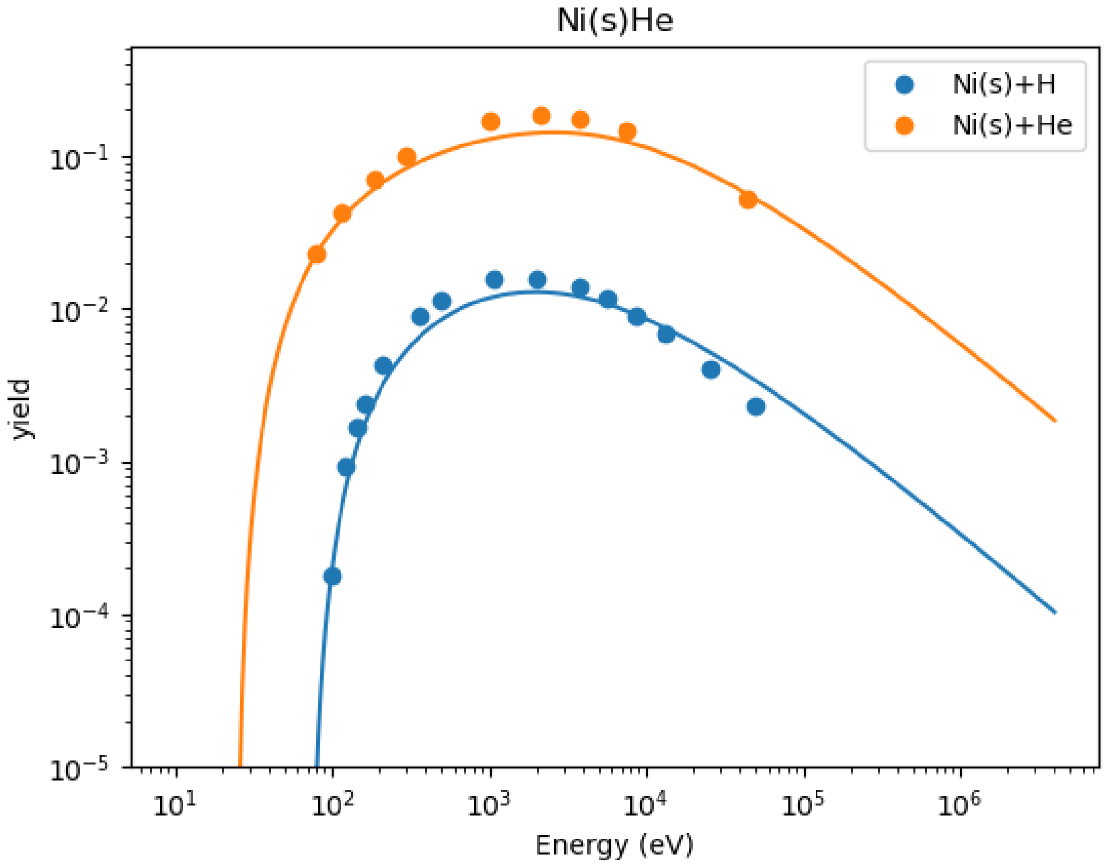

Figure 4.4: Experimental sputtering yields for Ni(s) with both H and He atoms as impactors. The line shows a fit of the data using SciPy's curve_fit package. The fit produces a fitting factor, k, used in calculating sputtering yields.

4.4.2.2. Non-Thermal Sputtering

The erosion of dust grains due to non-thermal sputtering, characterized by Equation 4.5, is dependent upon the velocity of the grains relative to the gas. This velocity is expressed as $v_d = V_d - v_{gas} = V_s - 1/4V_s \simeq 3/4V_s$, where V_d is the velocity that the dust crosses the shock front with and is equal to the shock velocity V_s. The deceleration of the dust traveling at relative velocity v_d w.r.t. the shock velocity must also be taken into account. Assuming the gas is characterized by a single temperature and the dust grains are spheres of radius a, the deceleration rate of the dust grains can be expressed as,

$$\frac{dv_d}{dt} = -\frac{3n_{gas}kT}{2a\rho_d} \sum_{i}^{N_{species}} A_i G_i(s_i) \tag{4.14}$$

where the function $G_i(s_i)$ can be approximated as,

$$G_i(s_i) \approx \frac{8s_i}{3\sqrt{\pi}} \left(1 + \frac{9\pi}{64} s_i^2\right)^{1/2} \tag{4.15}$$

and ρ_d is the bulk density of the grain and A_i is the abundance of gas species *i* (Draine & Salpeter, 1979b).

4.4.2.3. Thermal Sputtering

Thermal sputtering occurs due to the interaction of the surrounding medium and the dust grain. This is largely due to the temperature and number density of the material and the surface binding energy of the grain species.

Table 4.1 lists the grain parameters relevant in calculating thermal sputtering effects. The surface binding energy, average atomic number, and mass of the grain are intrinsic to each grain species. The K value is a free parameter used to match calculated sputtering amounts with experimental data.

Table 4.1. Sputtering Parameters

Species	U_0(eV)	M_d	Z_d	K	References
Fe	4.31	56	26	0.23	1,10,11,17,20
FeS	4.12	44	21	0.18	21
Si	4.66	28	14	0.43	1,6,8,10,12,16,17
Ti	4.90	47.867	22	0.6 **	1,18,14
V	5.33	50.942	23	0.469 **	1,18,14
Cr	4.11	51.996	24	0.203 **	1,14
Co	4.44	58.933	27	0.658 **	1,14
Ni	4.45	58.693	28	0.2 **	1
Cu	3.50	63.546	29	0.135 **	1,14
C	4.0*	12	6	0.61	1,7,11,14,15
SiC	6.3	20	10	0.3	7,5,11
TiC	6.5 **	29.939	14	0.437 **	11
Al_2O_3	8.5	20.4	10	0.08	2,13
$MgSiO_3$	6.0	20	10	0.1	4,19
$Mg_2SiO_4^{***}$	5.7	20	10	0.1	19
SiO_2	6.42	20	10	0.1	2,3,9,13
MgO	5.17	20	10	0.1	2,13
Fe_3O_4	4.98	33.1	15.7	0.06	21
FeO	-	35.922	17	-	.

Note. — (1) Lide (1997); (2) Bach (1970); (3) Bach et al. (1974); (4) Barlow (1978); (5) Behrisch et al. (1976); (6) Blank & Wittmaack (1979); (7) Bohdansky et al. (1978); (8) Coburn et al. (1977); (9) Edwin (1973); (10) EerNisse (1971); (11) Hechtl et al. (1981); (12) Laegreid & Wehner (1961); (13) Nenadović et al. (1990); (14) Rosenber & Wehner (1962); (15) Roth et al. (1976); (16) Sommerfeldt et al. (1972); (17) Southern et al. (1963); (18) Stacey et al. (1977); (19) Tielens et al. (1994); (20) Von Seefeld et al. (1976); (21) Nozawa et al. (2006)****

Sublimation energy is from: National Institute of Standards and Technology (NIST) (2023)

* Not clear what energy is used (binding: 6.67, sublimation: 7.43). Value taken from Nozawa et al. (2006).

** Our K value estimates using the cited data.

*** Mg_2SiO_4 resulting from both key species (SiO and Mg) are treated the same for the sputtering constants.

**** Results are from Nozawa et al. (2006) use of the EDDY code.

4.5. Implementation

The destruction and erosion of the grains are carried out using the Dormand Prince Runge-Kutta integrator found in the C++ library, Boost. It combines a fifth-order Runge Kutta and a fourth-order Dormand Prince integrator to solve for the time step and error. A 1-D Makima interpolator is used to interpolate temperature, density, and volume as the simulation progresses. The erosion rate at each time step is determined by the interpolated values using Equations 4.5 or 4.6. The velocity of the dust with respect to the velocity of the gas is decelerated at each time step. As the reverse shock slows and the temperature decreases with expansion, erosion stops.

4.6. Results

Figure 4.5 shows the size distribution of all dust grains considered in Brooker et al. (2022). Plotted are the 15, 20, and 25 $M_\odot$ progenitor models. Subfigure a) shows two distinct distributions of the grain sizes. Intermediate to high energy explosions produce a power-law like size distribution. Low-energy explosions produce two curves signaling two separate bulk nucleation events. Similar trends are seen in Subfigure b) and c).

Sputtering was calculated for nine shock temperatures from 10^3 to 10^{11} K and seven shock velocities from 10^3 to 10^9 cm/s for a total of 81 combinations of shock and temperature. From the thermal and non-thermal sputtering results shown in Figures 4.3 and 4.2, sputtering peaks at a grain dependent temperature and velocity before decreasing. The intersection between the peak temperature and velocity should produce a region of maximum sputtering. This is shown in Figure 4.6 for $\mathrm{Fe_3O_4}$ and 4.9 for C grains. With shock temperatures between 10^7 K to 10^9 K and shock velocities 10^8 cm/s to 10^9 cm/s the most destruction is seen. This is expected since non-thermal sputtering dominates at 10^8 cm/s to 10^9 cm/s as seen in Figure 4.2. From Figure 4.3, thermal sputtering dominates at 10^7 K to 10^9 K.

Comparing the carbides and oxides in Figures 4.3 and 4.2, carbon is more temperature sensitive. Figure 4.3 shows significant sputtering at lower temperatures near 10^5 K. This is further shown in Figure 4.8 where significant destruction begins at 10^5 K with complete destruction at temperatures higher than 10^6 K. $\mathrm{Fe_3O_4}$ and $\mathrm{SiO_2}$ in Figures 4.6 and 4.9 show survival above 10^6 K. Overall, more carbon dust is destroyed than for silicates or oxides. This could be due to the lower bonding energy of carbon and the strong $\mathrm{Si-O}$ bond in silicates.

Figure 4.7 shows the change in average grain radius. In the shock range showing maximum destruction, a minor change is shown in the average grain radius. This is because the smaller grains are destroyed with the larger grains are eroded to sizes near the initial average grain size. It also shows that thermal dominated sputtering, sputtering with shock velocities under 10^7 cm/s and temperatures greater than 10^6 K, causes a decrease of average grain sizes of about 30% while areas of non-thermal dominated sputtering, sputtering with shock velocities above 10^7 cm/s and

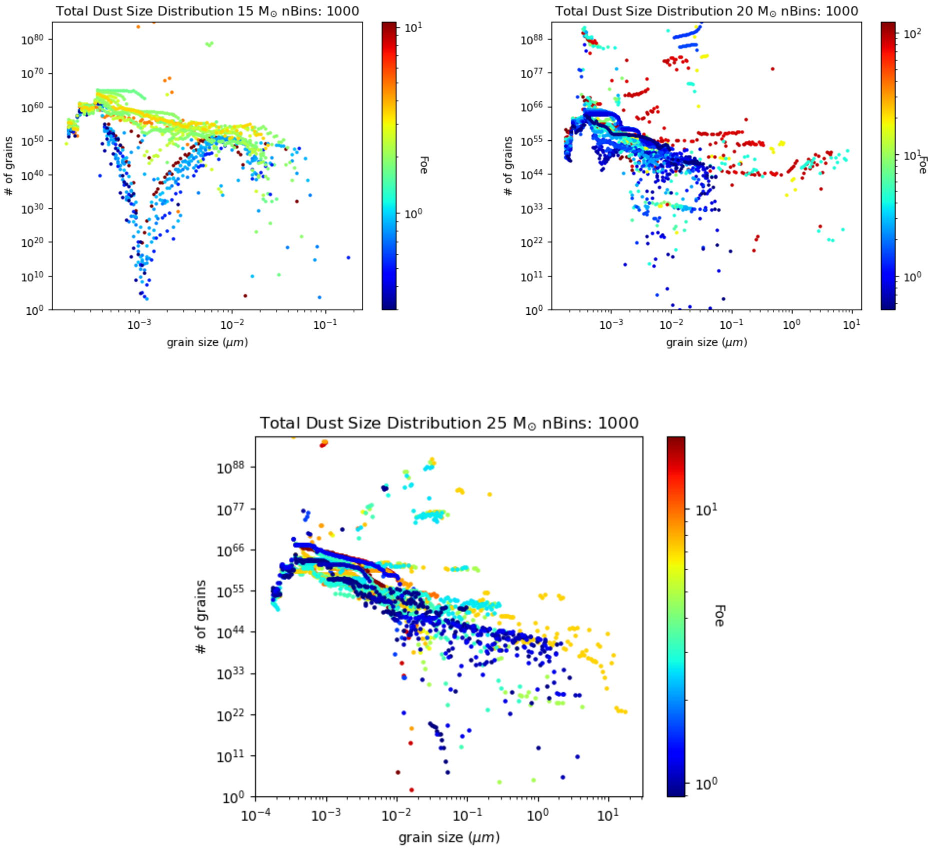

Figure 4.5: Total dust size distributions calculated for each individual model. The color of each dot corresponds to the model's explosion energy. Top left) size distributions of grains produced in 15 $M_\odot$ progenitors. Top right) 15 $M_\odot$ progenitors. Bottom) 25 $M_\odot$ progenitors.

temperatures less than 10^6 K, causes an average grain change closer to 40%.

4.7. Conclusions

Dust survival rates were calculated for a suite of shock parameters. Non-thermal and thermal sputtering was modeled for each shock temperature and velocity. The most dust destruction was seen for intermediate shock temperatures and velocities. This was attributed to the reduction of interactions between the shocked material and dust grains as the energy of the shock increased. More energetic shocks do not interact as strongly with the dust grains. This created an intermediate value for both shock temperatures and velocities where the most destruction was seen. The most destructive shocks also showed a small change in the average grain size. This was due to an obliteration of small grains and an erosion of large grains to smaller sizes. For other shock strengths, the average size of surviving dust grains was shifted towards smaller sizes. This was due to the erosion of all grain sizes. Carbon grains were more susceptible to destruction than silicate or

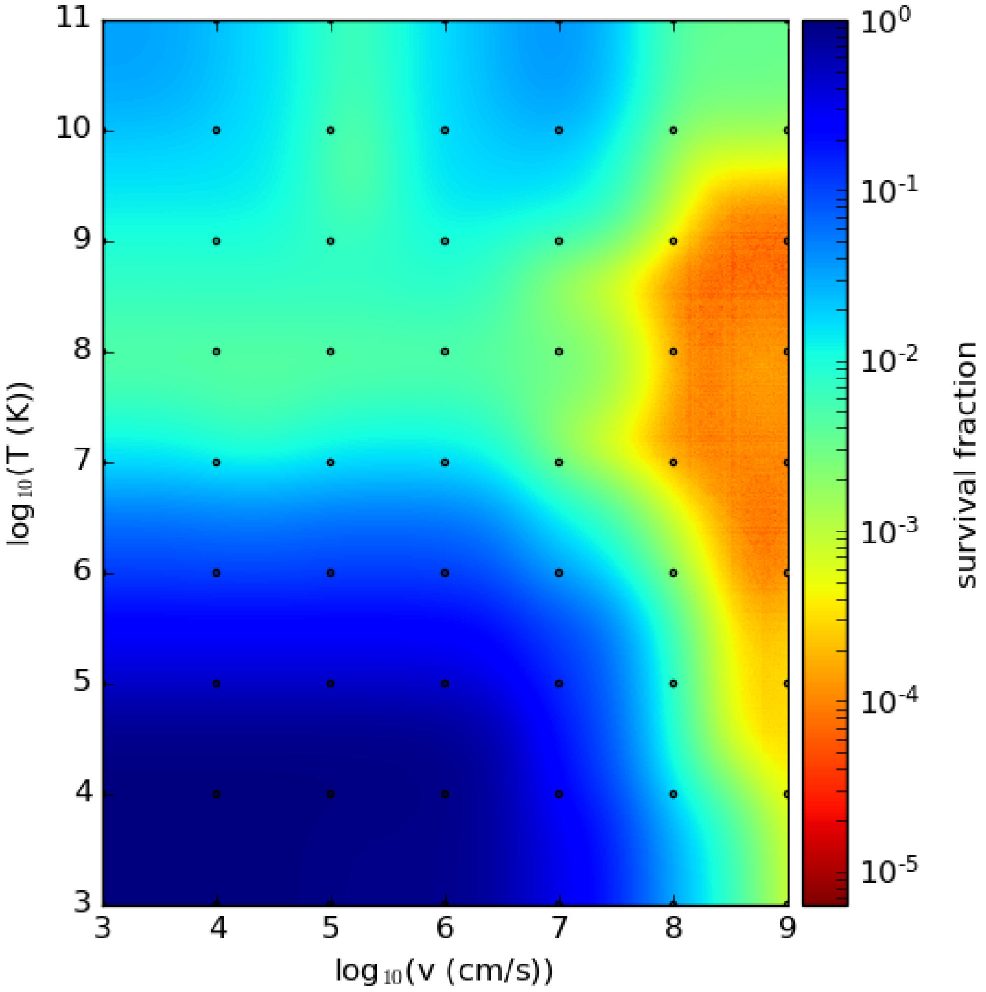

Figure 4.6: Plotted are the survival fractions of $\mathrm{Fe_3O_4}$ in a low-explosion energy, 15 $\mathrm{M_\odot}$ model. Each black dot denotes a calculated value for each combination of shock temperature and velocity. A 2-D linear interpolator is used to calculate the rest of the phase space.

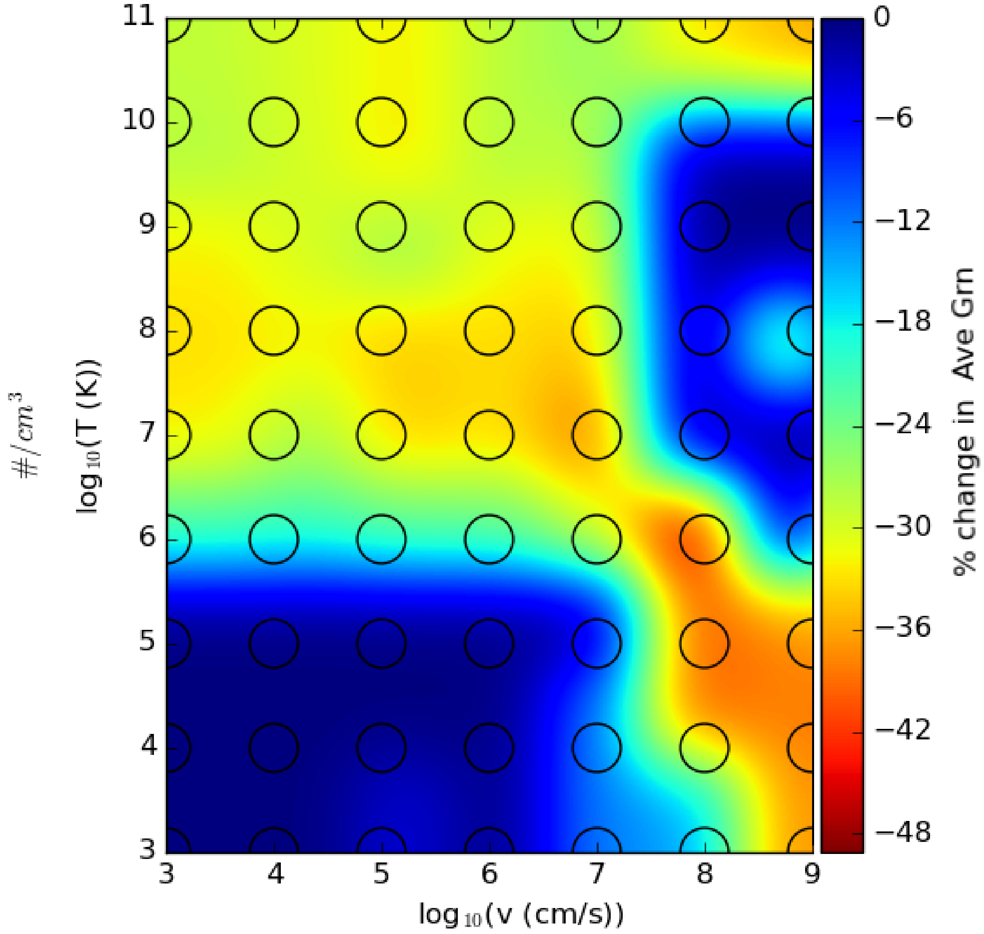

Figure 4.7: The change in average grain size of $\mathrm{Fe_3O_4}$ is plotted for a low-explosion energy, 15 $M_\odot$ model. Each black circle encases a calculated point. A 2-D linear interpolator is used to calculate the rest of the phase space.

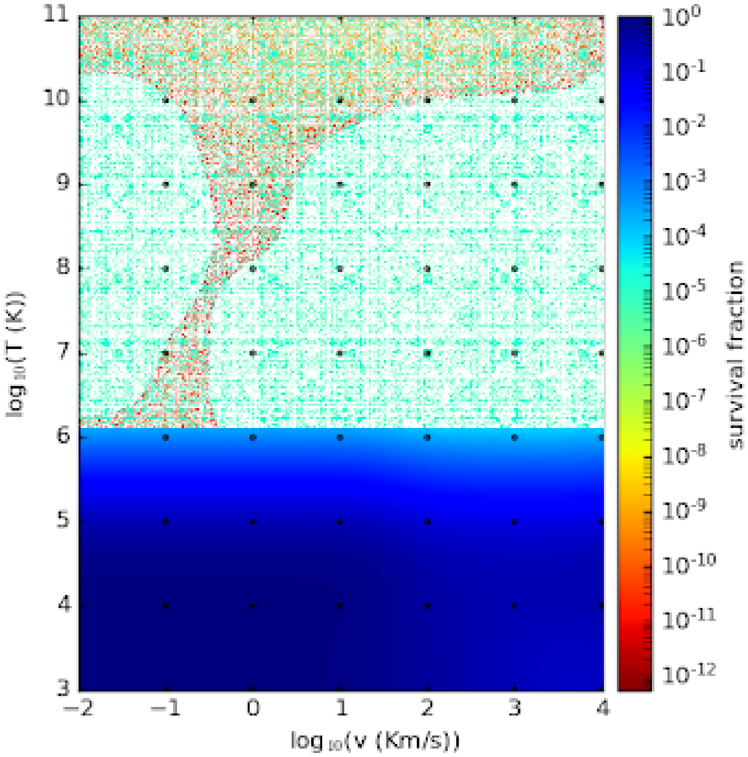

Figure 4.8: Plotted are the survival fractions of C in a low-explosion energy, 15 $M_\odot$ model. Each black dot denotes a calculated value for each combination of shock temperature and velocity. A 2-D linear interpolator is used to calculate the rest of the phase space. The interpolation fails at the top portion of the plot due to the complete destruction of carbon dust at shock temperatures higher than 10^6 K.

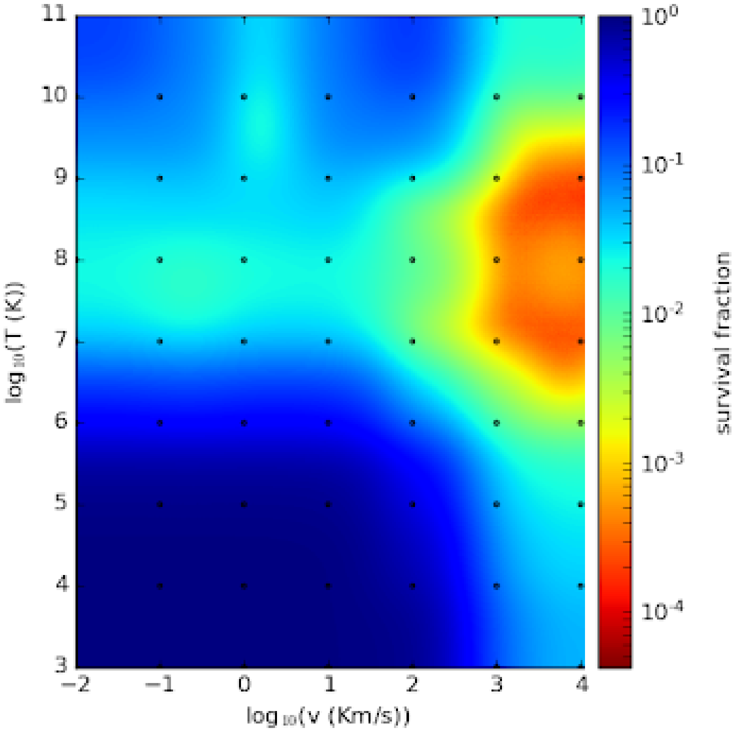

Figure 4.9: Plotted are the survival fractions of $\mathrm{SiO_2}$ in a low-explosion energy, 15 $M_\odot$ model. Each black dot denotes a calculated value for each combination of shock temperature and velocity. A 2-D linear interpolator is used to calculate the rest of the phase space.

oxide dust grains. Future work will be on modeling the reverse shock with hydrodynamical codes and the resulting destruction.

Table 4.2. Constants & Symbols

Symbol	Quantity	Units
n_{gas}	number density of gas	$\#/cm^3$
a_j	radius of grain species j	cm
m_{sp}	average mass sputtered off grain	g
rho_d	bulk density of the grain	g/cm^3
$N_{species}$	# gas species	unitless
A_i	abundance fraction of species i	# of species i/# total gas
k	Boltzmann constant ($1.38064852 \times 10^{-16}$)	erg/K
T	gas temperature	K
m_i	mass of an impactor	g
v_d	velocity of the dust w.r.t. the gas	cm/s
s_i	ratio of the kinetic energy ($\frac{m_i v_d^2}{2kT}$)	unitless
E_{th}	threshold energy	ergs
ϵ_{th}	ratio of the threshold energy (E_{th}/kT)	unitless
ϵ_i	ratio of the incident projectile energy (E_i/kT)	unitless
Y_i	yield	# sputtered atoms/impactor
E	energy	ergs
U_0	binding energy, sublimation energy is used	eV
M_i	mass of an impactor	amu
M_d	mass of target	amu
$S_i(E)$	nuclear stopping cross-section	$ergs/cm^2$
a_{sc}	interaction potential between nuclei screening length	cm
Z_i	atomic number of the impactor	unitless
Z_d	atomic number of the target	unitless
a_0	Bohr's radius (5.29×10^{-9})	cm
$s_i(\epsilon_i)$	approximation function of the reduced energy	unitless
ϵ_i	reduced energy	unitless

Note. — Further discussion on the symbols and quantities used can be found in Brooker et al. (2022); Biscaro & Cherchneff (2016); Nozawa et al. (2006); Sluder et al. (2018).

4.8. Applications

Dust formed in CCSNe are processed by the reverse shock from the expansion of the remnant. The amount of surviving dust depends on explosion parameters and the surrounding environment. This dust is injected into the ISM where it scatters light from distant objects. These scattering effects are discussed in Chapter 5.

CHAPTER 5

The Scattering of Light & Dust Opacities

5.1. Mie Scattering

Mie scattering is the scattering of incident radiation by a spherical particle. It is most dominant with scattering particles larger than or comparable to the wavelength. Mie scattering produces the glare seen when shining a light into fog. Mie scattering is important in clouds in the Earth's atmosphere, the solar system, and in exoplanets. A large portion of the light is forward scattered, with a small amount of light being scattered backwards. As the size of the particle increases, the forward scattering angle decreases and is more intense. This forward scattering behavior is shown in Figure 5.1. The amount of scattering is determined from the particle's complex index of refraction, $m = n + ik$, and size parameter, $x = 2\pi a/\lambda$, where a is the radius and λ is the wavelength.

The scattering of the incident light, represented by the four component Stokes vector $\vec{I_i}$, is described with the scattering (Müller) matrix **F**,

$$\vec{I_s} = \mathbf{F}\vec{I_i} \tag{5.1}$$

where $\vec{I_s}$ is the Stokes vector after scattering. The Müller matrix **F**,

$$\mathbf{F}(\Theta) = \begin{pmatrix} F_{11}(\Theta) & F_{12}(\Theta) & 0 & 0 \\ F_{12}(\Theta) & F_{11}(\Theta) & 0 & 0 \\ 0 & 0 & F_{33}(\Theta) & F_{34}(\Theta) \\ 0 & 0 & -F_{34}(\Theta) & F_{33}(\Theta) \end{pmatrix} \tag{5.2}$$

where Θ is the scattering angle, the angle between the incident and scattered light.

The non-zero components of the scattering matrix are:

$$
\begin{aligned}
F_{11}(\Theta) &= \frac{1}{2}\left[|S_2(\Theta)|^2 + |S_1(\Theta)|^2\right] \\
F_{12}(\Theta) &= \frac{1}{2}\left[|S_2(\Theta)|^2 - |S_1(\Theta)|^2\right] \\
F_{33}(\Theta) &= \frac{1}{2}\left[S_2^*(\Theta)S_1(\Theta) + S_2(\Theta)S_1^*(\Theta)\right] \\
F_{34}(\Theta) &= \frac{i}{2}\left[S_1(\Theta)S_2^*(\Theta) - S_2(\Theta)S_1^*(\Theta)\right]
\end{aligned}
\tag{5.3}
$$

with the amplitude functions, S, as:

$$
\begin{aligned}
S_1(\Theta) &= \sum_{n=1}^{\infty} \frac{2n+1}{n(n+1)}\left[a_n\pi_n(\Theta) + b_n\tau_n(\Theta)\right] \\
S_2(\Theta) &= \sum_{n=1}^{\infty} \frac{2n+1}{n(n+1)}\left[a_n\tau_n(\Theta) + b_n\pi_n(\Theta)\right]
\end{aligned}
\tag{5.4}
$$

the angular functions π_n and τ_n, are:

$$
\begin{aligned}
\pi_n(\Theta) &= \frac{2n-1}{n-1}\cos(\Theta)\pi_{n-1}(\Theta) - \frac{n}{n-1}\pi_{n-2}(\Theta) \\
&\quad \text{for } \pi_0 = 0 \text{ and } \pi_1 = 1 \\
\tau_n(\Theta) &= n\cos(\Theta)\pi_n(\Theta) - (n+1)\pi_{n-1}(\Theta)
\end{aligned}
\tag{5.5}
$$

following Wolf & Voshchinnikov (2004), the Mie coefficients, a_n and b_n, are defined by Bessel functions of the first and second kind (Deirmendjian et al., 1969):

$$
\begin{aligned}
a_n &= \frac{\left[\frac{A_n}{m} + \frac{n}{x}\right] J_{n+1/2}(x) - J_{n-1/2}(x)}{\left[\frac{A_n}{m} + \frac{n}{x}\right] J_{n+1/2}(x) - J_{n-1/2}(x) + i\left(\left[\frac{A_n}{m} + \frac{n}{x}\right] Y_{n+1/2}(x) - Y_{n-1/2}(x)\right)} \\
b_n &= \frac{\left[mA_n + \frac{n}{x}\right] J_{n+1/2}(x) - J_{n-1/2}(x)}{\left[mA_n + \frac{n}{x}\right] J_{n+1/2}(x) - J_{n-1/2}(x) + i\left(\left[mA_n + \frac{n}{x}\right] Y_{n+1/2}(x) - Y_{n-1/2}(x)\right)}
\end{aligned}
\tag{5.6}
$$

with,

$$
A_n = -\frac{n}{mx} + \frac{J_{n-1/2}(mx)}{J_{n+1/2}(mx)} \tag{5.7}
$$

and recursively as:

$$A_n = -\frac{n}{mx} + \left(\frac{n}{mx} - A_{n-1}\right)^{-1} \tag{5.8}$$

using the recurrence relationship between Bessel functions:

$$\begin{aligned} J_{n+1/2} &= \frac{\left[\frac{2}{\pi x} + Y_{n+1/2}(x) J_{n-1/2}(x)\right]}{Y_{n-1/2}(x)} \\ J_{1/2}(x) &= \sqrt{\frac{2}{\pi x}} \sin(x) \end{aligned} \tag{5.9}$$

$$\begin{aligned} Y_{n+5/2} &= \frac{2n+1}{x} Y_{n+3/2}(x) - Y_{n+1/2}(x) \\ Y_{1/2} &= -\sqrt{\frac{2}{\pi x}} \cos(x) \\ Y_{3/2} &= -\sqrt{\frac{2}{\pi x}} \left(-\frac{\cos(x)}{x} - \sin(x)\right) \end{aligned} \tag{5.10}$$

the scattering, back-scattering, extinction, and radiation pressure efficiency factors are given by the Mie coefficients:

$$\begin{aligned} Q_{sca} &= \frac{2}{x^2} \sum_{n=1}^{\infty} (2n+1)(|a_n|^2 + |b_n|^2) \\ Q_{bk} &= \frac{1}{x^2} \left| \sum_{n=1}^{\infty} (2n+1)(-1)^n (a_n - b_n) \right|^2 \\ Q_{ext} &= \frac{2}{x^2} \sum_{n=1}^{\infty} (2n+1) Re a_n + b_n \\ Q_{abs} &= Q_{ext} - Q_{sca} \\ Q_{pr} &= Q_{ext} - g Q_{sca} \end{aligned} \tag{5.11}$$

with asymmetry factor, g.

$$g = \frac{Q_{ext} - Q_{pr}}{Q_{sca}} \tag{5.12}$$

the asymmetry factor describes the forward and back scattering.

The corresponding cross-section can be found by:

$$C = GQ \tag{5.13}$$

with the geometric cross-section $G = \pi a^2$.

For a system with multiple grain species and a non-uniform size distribution (the grains of a species not all one size), weights of each grain species contribute differently to the opacity. The Stokes parameters and cross-section become additive. Assuming there are J species, a size distribution $n_j(a)$ with a minimum size a_{min} and maximum size a_{max}, and a fraction abundance of species f_j, the normalization is as follows,

$$\begin{aligned} &\sum_{j=1}^{J} f_i \int_{a_{min}}^{a_{max}} n(a)da = 1 \\ &\sum_{j=1}^{J} f_i = 1 \end{aligned} \tag{5.14}$$

The new weight values for cross-sections are,

$$\langle C \rangle = \sum_{j=1}^{J} f_i \int_{a_{min}}^{a_{max}} n(a) C_j da \tag{5.15}$$

The values of the Müller matrix become,

$$\langle F_{ik} \rangle = \sum_{j=1}^{J} f_i \int_{a_{min}}^{a_{max}} n(a) F_{ik,j} da \tag{5.16}$$

The asymmetry factor is,

$$\langle g \rangle = \frac{\sum_{j=1}^{J} f_i \int_{a_{min}}^{a_{max}} n(a) g_i C_{sca,j} da}{\sum_{j=1}^{J} f_i \int_{a_{min}}^{a_{max}} n(a) C_{sca,j} da} \tag{5.17}$$

5.1.1. Mie Scattering Code Development

`mie_scat` (Stangl, 2022) is a Fortran implementation of Mie scattering. It is a subroutine for calculating the Mie scattering cross-sections, absorption cross-sections, and efficiency coefficients of dust grains. It was originally designed as a wrapper function between PHOENIX and the Mie scattering calculations, but it can be used to return scattering cross-sections and efficiency factors to other programs. The user can change the number of grain species, the relative abundances, and size distributions.

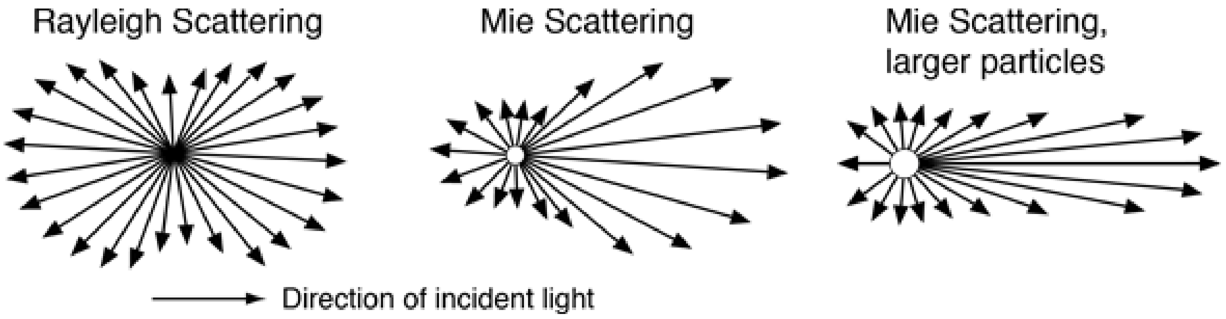

Figure 5.1: A diagram of the scattering of light by Rayleigh and Mie Scattering. When the scattering particle is much smaller than the wavelength, Rayleigh scattering produces a similar amount of forward- and back-scattering of incident light (left). When the size of the scattering particle is comparable to the wavelength, Mie scattering produces more forward scattering of light (middle). When the size of the scattering particle is larger than the wavelength, Mie scattering produces a sharper and more intense forward scattering lobe (left). Image taken from Hyperphysics (2023)

Figure 5.2 shows how the cross-sections as a function of wavelength vary as the grain size changes. As the size decreases, the cross-section overall decreases and larger wavelengths are less affected. The same trend can be seen in Figure 5.3. Figure 5.3 also shows how the efficiency factors change with a logarithmic, $a = -3.5$, distribution of Si and Si & C. This is characteristic of the size distributions found in the ISM.

5.2. Rayleigh Scattering

Rayleigh scattering is a minor contributor to the scattering of light by dust grains and is more prevalent with smaller scatterers. Rayleigh scattering is the scattering of radiation by bound systems when the wavelength of the incident light is much larger than the size of the scattering particle. Scattering particles include atoms, molecules, and very small dust grains. It dominates at shorter wavelengths. It is responsible for scattering blue light in the atmosphere, producing a blue sky. A diagram of the forward and back scattering from Rayleigh scattering is shown in Figure 5.1.

Rayleigh scattering can be represented real transitions of the scatterer with classical oscillators of strength f_{ij} and resonant frequencies ω_{ij} equal to the actual transition frequencies. For $\omega << \omega_{ij}$, the cross-section becomes,

$$\Theta(\omega) = \frac{8\pi e^4}{3m^2c^4}\frac{f_{ij}\omega^4}{(\omega_{ij}^2 - \omega^2)^2} = \Theta_e\frac{f_{ij}\omega^4}{(\omega_{ij}^2 - \omega^2)^2} \tag{5.18}$$

Far from the resonant frequency, the scattering cross-section $\Theta(\omega)$ varies as ω^4 or as λ^{-4}. Rayleigh scattering dominates when the frequency of the incident photon is close to the resonance with a bound-bound transition of the scattering particle (Hubeny & Mihalas, 2015). The amount

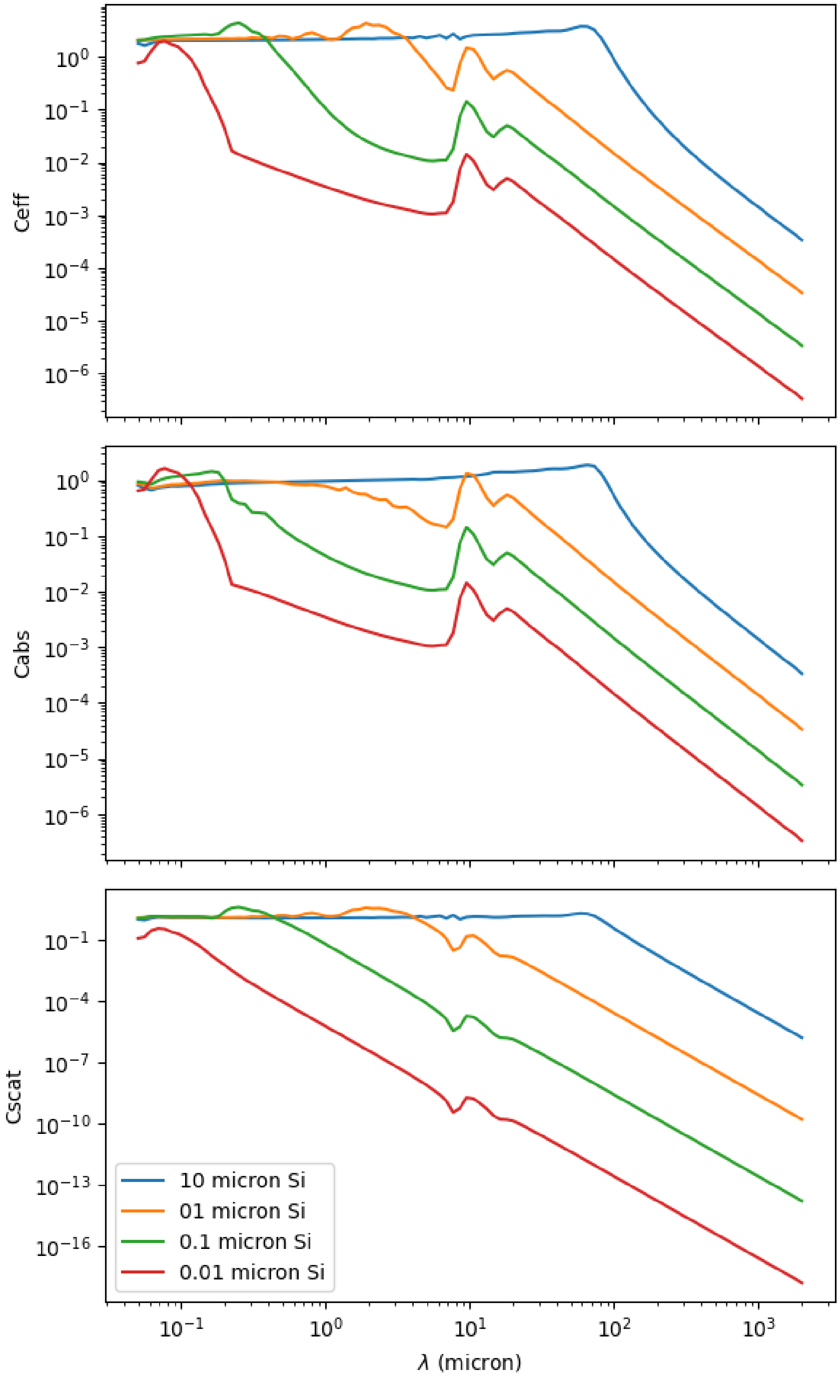

Figure 5.2: Calculated cross-sections of Si as a function of wavelength from `mie_scat`. The sizes of Si grains vary from 0.01 µm to 10 µm.

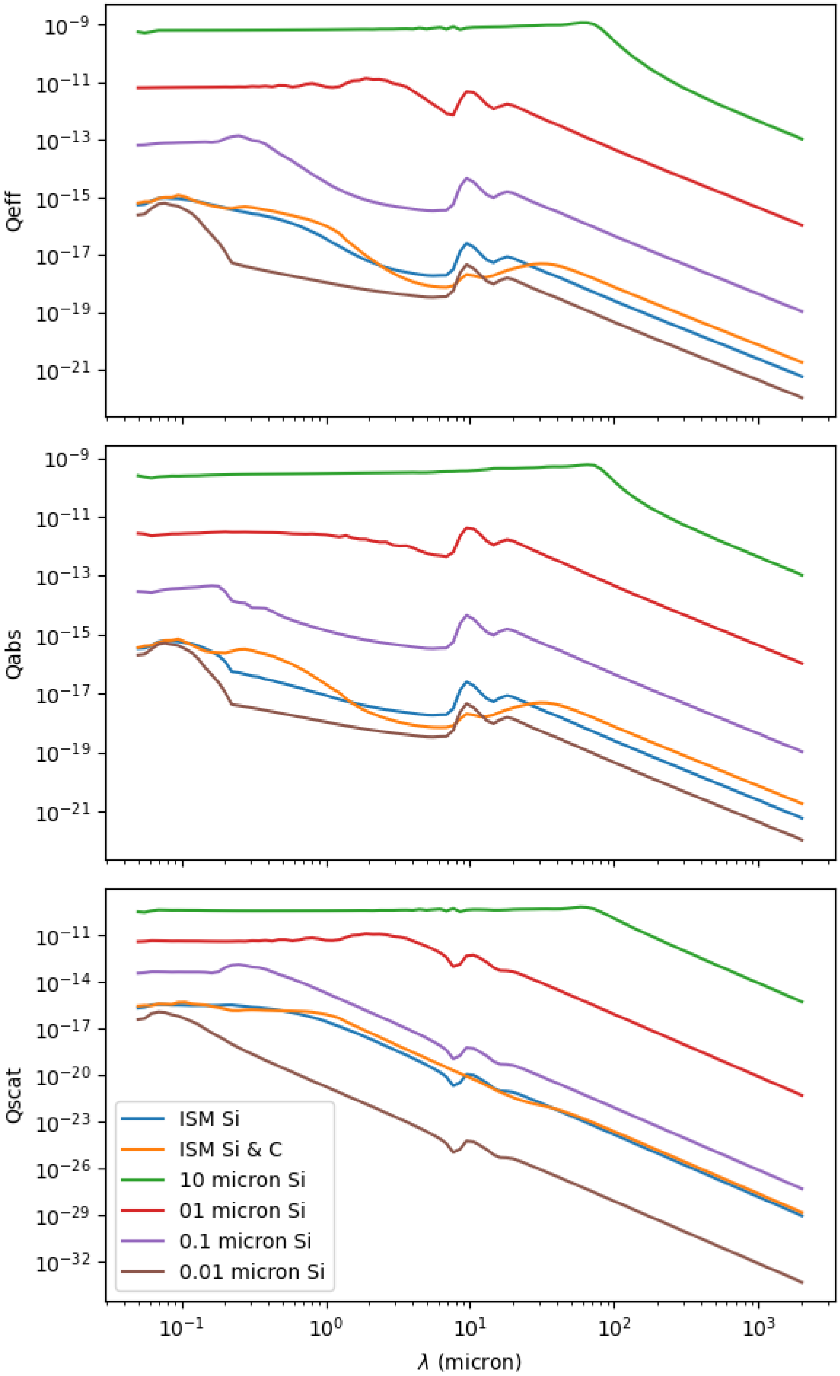

Figure 5.3: Calculated efficiency factors of Si as a function of wavelength using `mie_scat`. The sizes of Si grains vary from 0.01 μm to 10 μm.

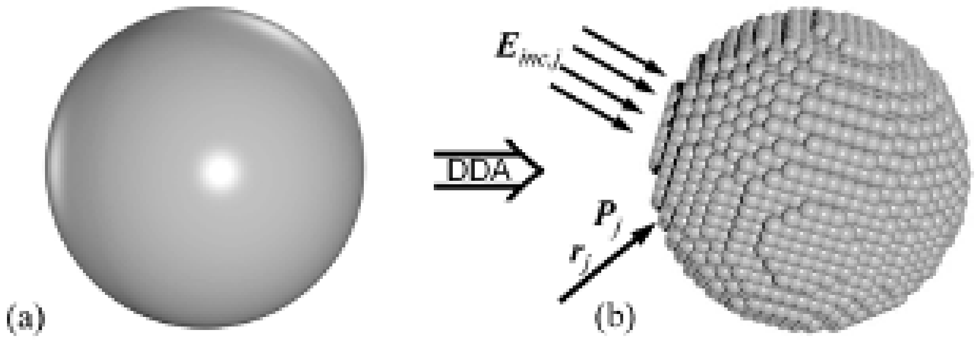

Figure 5.4: Target representation of DDA. (a) arbitrarily shaped particle and (b) approximation by discrete polarizable point dipoles. Image taken from Kies et al. (2011).

of scattering increases as the wavelength of incident light decreases, leading to a more scattering of bluer light than red light. Because of dust grains large size, only the smallest dust grains will exhibit Rayleigh scattering.

5.3. Discrete Dipole Approximation (DDA)

DDA is a useful method of computing the scattering and absorption of targets of arbitrary shape. It is accurate for targets with a lower dielectric constant, $|m| \leq 2$. Surface granularity of materials with high refractive indices reduce accuracy (Draine, 1988).

DDA first approximates the target as a finite array of N total polarizable point dipoles. Points acquire dipole moments in response to the local electric field and interactions with electric fields of other point dipoles. The complex dipole moment, P_j of each point is represented by,

$$P_j = \alpha_j E_{ext,j} \tag{5.19}$$

$E_{ext,j}$ is the complex electric field from all sources external to point j and α_j is the polarizability tensor. The polarizabilty tensors of a target can be altered to produce an isotropic or anisotropic material.

The scattering problem can then be reduced to the matrix equation,

$$\sum_{k=1}^{N} \mathbf{A_{jk}} P_k = E_{inc,j} \qquad \text{for (j=1,...N)} \tag{5.20}$$

A$_{jk}P_j$ is the contribution to the electric field at point j by the dipole at position k, A_{jk} are 3×3 symmetric matrices, and $E_{inc,j}$ is the incident planar wave at point j. After solving for the polarizability vector, it is used to determine the respective cross-sections. The efficiency factors are described by the ratio between these cross-sections and the geometric cross-section. Further discussion of these DDA calculations and methods are found in Draine & Flatau (1994); Draine

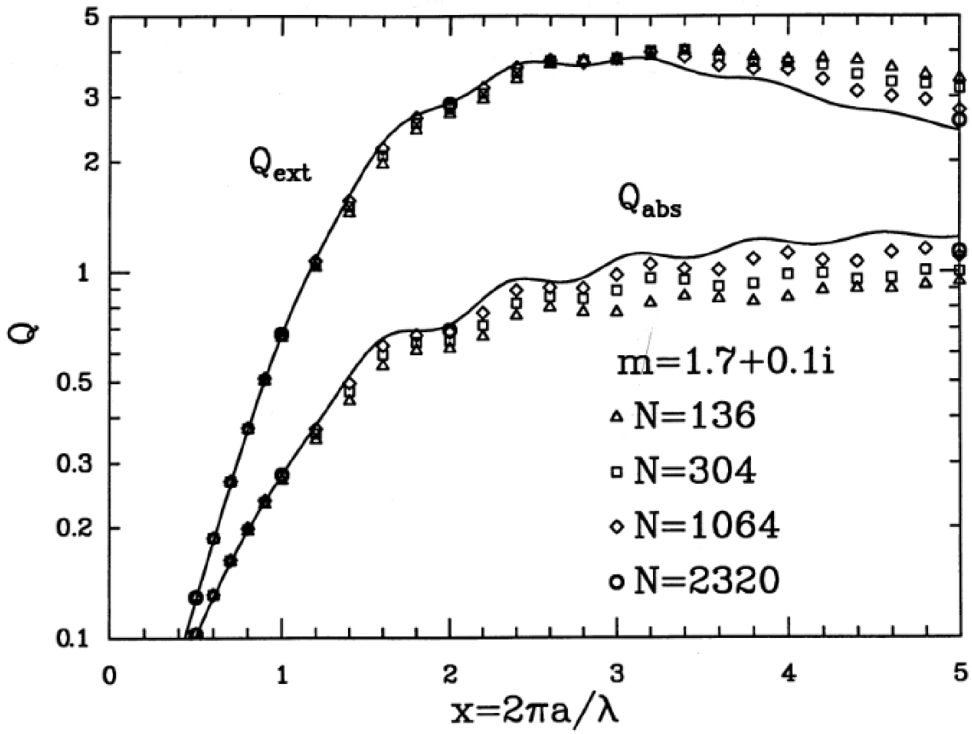

Figure 5.5: A comparison between the efficiency factors obtained by Mie scattering and DDA. The scattering material is described by the size parameter $x = 2\pi a/\lambda$ and index of refraction $m = 1.7 + 0.1i$. The results of Mie scattering are shown by the solid black line. The DDA results are shown for $N = 136$, 304, 1064, and 2320. Image taken from Draine (1988).

(1988).

DDSCAT is a Fortran implementation of DDA following the above calculations (Draine, 1988; Draine & Flatau, 1994). A comparison between the results obtained by DDASCAT and Mie scattering are shown in Figure 5.5. Materials with a low imaginary component to the refractive index produce a more accurate result. At large size parameters, DDA tends to slightly diverge from Mie scattering as seen in Figure 5.5. This suggests a reliable method of scattering non-sperical, small dust with low indices of refraction. Because dust is not believed to be perfectly spherical, DDA provides a reliable method to determine the scattering of light by dust grains.

5.4. Applications

The scattering of light by dust depends strongly on the size and composition of the dust. Mie scattering is important with dust and in planetary atmospheres. Scattered light alters observations. Chapter 6 discusses observational effects of dust in variable stars and in SN explosions. It explores observational and theoretical work related to variable stars and supernovae, focusing on their characteristics and the presence and formation of dust in their surrounding environments.

CHAPTER 6

Observational Work

6.1. Luminous and Variable Stars in NGC 2403 and M81

Spectroscopy and multi-wavelength photometry are presented for luminous and variable star candidates in the spiral galaxies NGC 2403 and M81 (Humphreys et al., 2019a). The brightest stars with signs of variability are selected from the Zickgraf & Humphreys (1991) catalogs: 124 stars from NGC 2403 and 91 stars from M81. These are assigned spectral types (Humphreys et al., 2019b). Out of these, 100 stars are found to be foreground or non-member stars. Stars of particular interest are B[e] supergiants (sgBe), Intermediate-type supergiants, and Luminous Blue Variables (LBVs). Spectra for the B[e] supergiant candidates share spectral features of other sgBe stars, namely strong Balmer emission with P Cygni profiles, distinct elemental lines, significant variability, and evidence of strong stellar winds and mass loss. Candidate supergiant spectra show high episodic mass loss and marginal variability. LBV candidate spectra share spectral features of Of or late N-rich Wolf-Rayet stars and photometry shows variability, suggesting they are LVBs in quiescent periods. Figure 6.1 shows spectral energy densities of LBVs (top), sgB[E] stars (middle), and intermediate-type supergiants (bottom). The infrared excess suggests significant circumstellar dust in the sgB[e] stars and one of the supergiants (left). The LBV infrared excess is suggested to be from free-free emission and not dust. Hertzsprung-Russell (HR) diagrams are shown for the confirmed NGC 2403 and M81 stars. Further discussion includes an analysis of two SN imposters, stars surviving extreme mass loss and eruptions, in NGC 2403 and their presented HR diagrams.

6.2. POISE

Precision Observations of Infant Supernova Explosions (POISE) is a mulit-institutional collaboration of observers and theorists that aims to develop high precision and timely observations of early supernovae (Burns et al., 2021). Much of the physics of SNe and their progenitors is gained from SN observations far past the explosion. To gain a better understanding, high-precision and rapid-cadence observations are needed within hours to days after the explosion. This allows for better estimates of explosion parameters, improving and determining the efficacy of current explosion models.

With surveys and higher cadence observations, we can observe events hours after the explosion, allowing us to pinpoint observational indicators and differentiate between competing models.

With advanced discovery surveys that delve deeper and operate with high-cadence, such as

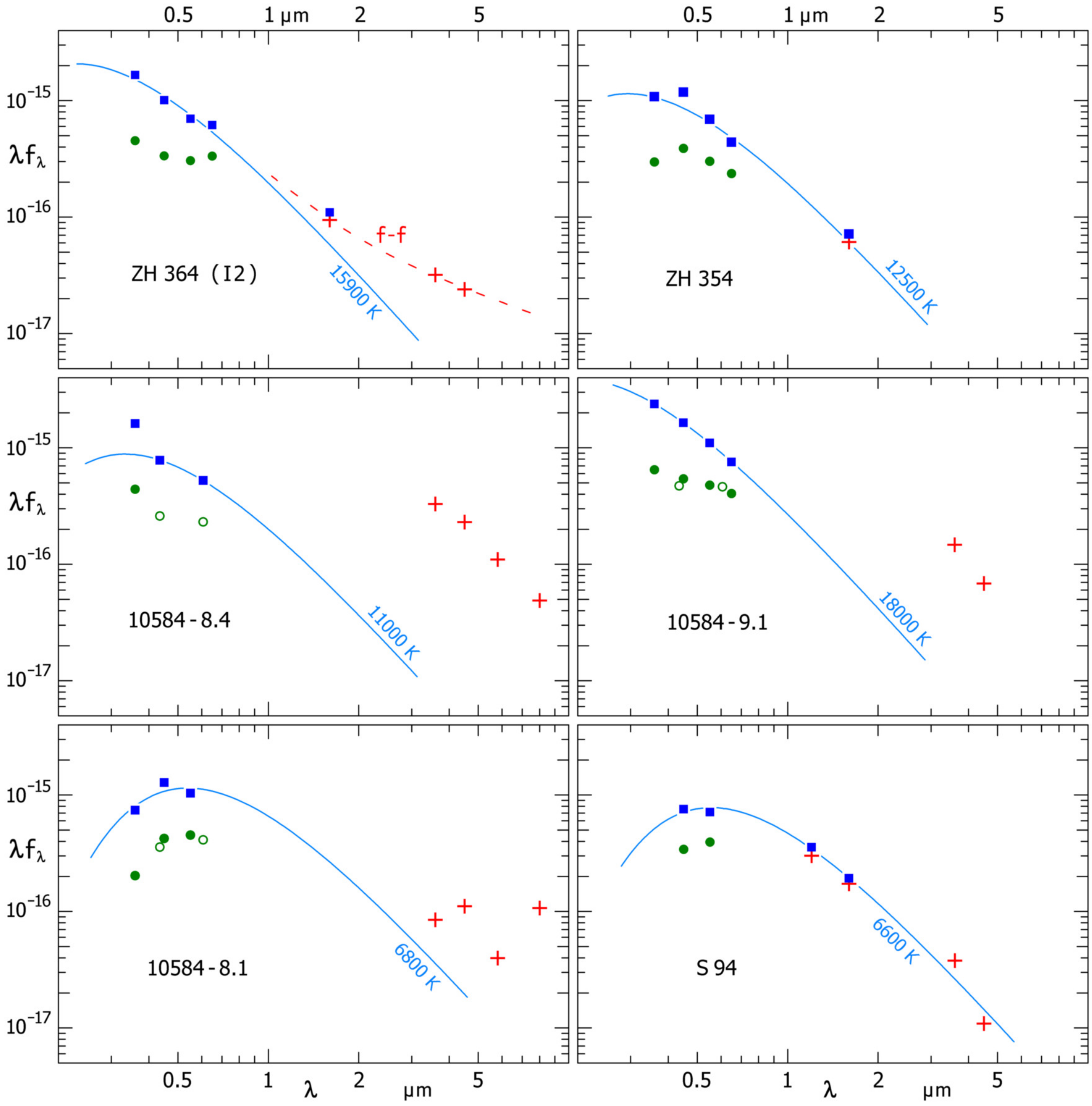

Figure 6.1: The spectral energy Distributions for six luminous stars. The presence or lack of circumstellar dust is shown in each. The green dots show the observed magnitudes from the Large Binocular Telescope and the blue squares show the same but corrected for interstellar extinction. The open green circles show magnitudes taken from the Hubble Space Telescope. The red crosses show the NIR magnitudes from the Hubble Space Telescope and Spitzer data. Image taken from Humphreys et al. (2019a).

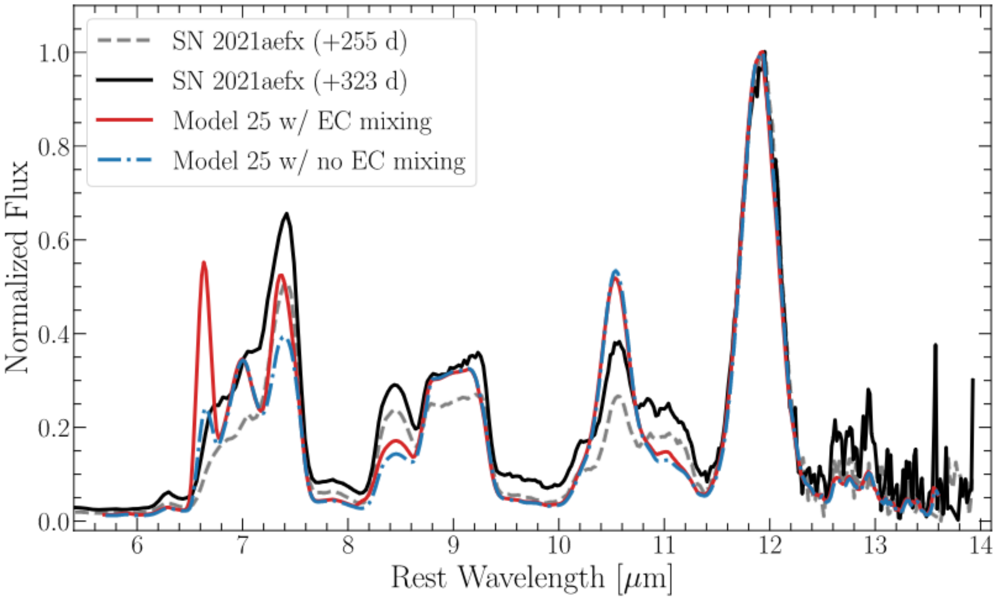

Figure 6.2: Comparison of the synthetic MIR spectrum of the off-center Model 25 from Hoeflich (2017), seen from -30°, without (blue) and with (red) mixing of the electron capture elements and the JWST/MIRI LRS spectrum of SN 2021aefx at +255 (dashed gray) and +323 (solid black) days relative to the B-band maximum. Image taken from DerKacy et al. (2023).

ASAS-SN, ATLAS, and ZTF, we can track events hours after explosion. This highlights observational indicators that determine the efficacy of and improve current, competing models.

Quick photometric follow-up with the Swope telescope is essential to gaining early optical light-curves, spectra, and to study candidates hours after discovery such as with the early detection of SN2022esa (Lu et al., 2022).

6.2.1. JWST Low-resolution MIRI Spectral Observations of SN 2021aefx: High-density Burning in a Type Ia Supernova

James Webb Space Telescope (JWST) low-resolution mid-infrared (MIR) spectroscopic observations of the normal Type Ia supernova (SN Ia) SN 2021aefx at +323 days past rest-frame B-band maximum light are analyzed (DerKacy et al., 2023). The spectrum shows many unique features: a flat-topped [Ar III] 8.991 µm profile, a strongly tilted [Co III] 11.888 µm feature, and stable Ni lines. The observations are compared to synthetic spectra from non-local thermodynamic equilibrium multidimensional models with and without electron capture elements. The comparison is shown in Figure 6.2. Similarities between the two are used to detect elements within the spectral blends and compare explosion physics. The presence of emission lines and electron capture elements are used to determine the mass of the progenitor white dwarf (WD) and chemical asymmetries in the ejecta. These observations suggest SN 2021aefx is an off-center delayed detonation explosion of a near Chandrasekhar mass WD at an angle of -30° relative to the point of the defla-

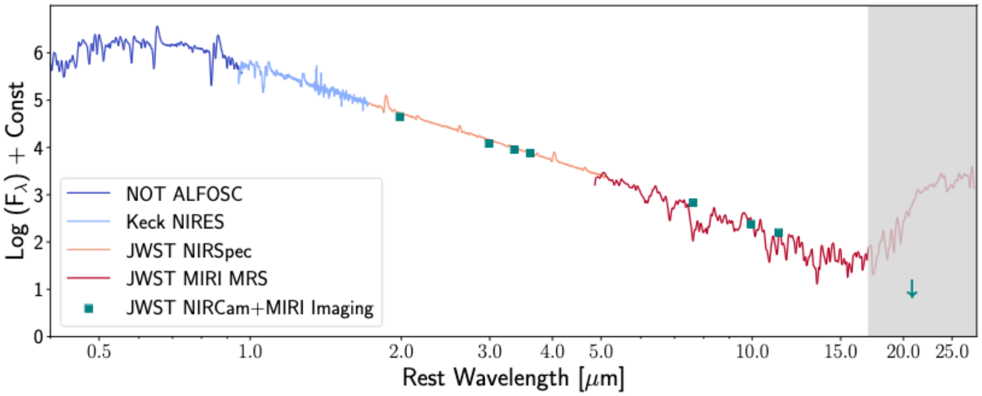

Figure 6.3: The spectral energy distribution of SN 2022acko. The Keck (NIRES) spectrum is constant shifted to match the optical and JWST spectrum. Channel 4 shows background dominated noise. Image taken from Shahbandeh et al. (2024).

gration to detonation transition. The strengths of Ni lines show there is little mixing in the ejecta's center. Stable Ni and the Ar velocity distributions suggest a lower limit 1.2 $M_\odot$ for the progenitor WD, implying most sub-Chandrasekhar Mass explosions are not characteristic of SN 2021aefx. This result shows how MIR spectra are essential to identifying viable explosion models for Type Ia SNe.

6.2.2. JWST NIRSpec+MIRI Observations of the nearby Type IIP supernova 2022acko

JWST near-infrared (NIR) and MIR spectroscopy and photometry are presented for the Type IIP SN 2022acko at 50 days past explosion (Shahbandeh et al., 2024). This is the first JWST observation of a CCSN . The goal of this project is to observe and collect data from early times to late times when CO and SiO molecules and dust form, tracking the evolution of an SN IIP. Followup ground observations of optical and additional NIR spectral bands were collected. H spectral series dominate the obtained spectrum. Spectral features of heavier elements are present. The spectrum evolves slower than other SN IIP, SN 2005a, suggesting a larger progenitor mass. A lack of CO line signatures show no formation of CO and an estimated CO mass in the CSM of less than 10^{-8} $M_\odot$. Combining all spectral data, a 0.4 to 25 µm spectral energy density (SED) was obtained at an average of 52 days post explosion. The SED of SN 2022acko is shown in Figure 6.3. The background is responsible for the MIR increase and is not caused by the SN or its environment. This suggests little-to-no pre-existing dust or molecules present in SN 2022acko.

6.2.3. JWST MIRI/Medium Resolution Spectrograph (MRS) Observations and Spectral Models of the Under-luminous Type Ia Supernova 2022xkq

JWST MIR spectrum is presented for the under-luminous Type Ia SN 2022xkq at 130 days post explosion(DerKacy et al., 2024). The spectrum is shown in Figure 6.4 with a fitted model.

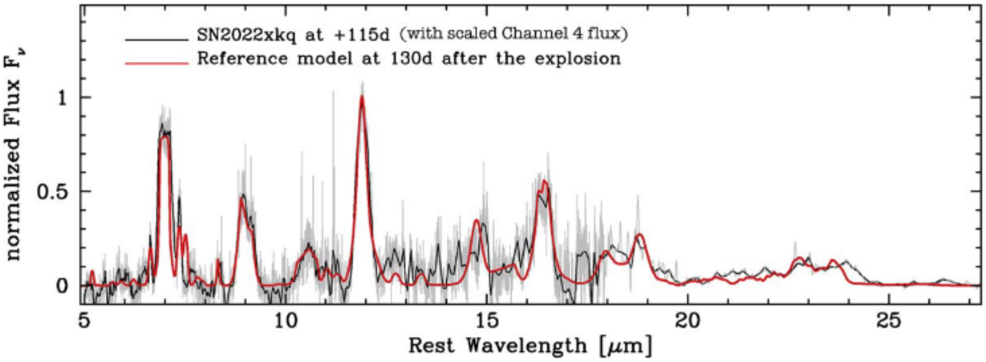

Figure 6.4: The MIR spectra of SN 2022xkq (black) with a flux calibrated channel 4 shown with a fitted synthetic spectrum from the reference model (red). Image taken from DerKacy et al. (2024).

The spectrum has features characteristic of under-luminous SNe; lower ionization states of species compared to normal luminosity SN, stable Ni lines, and blended Ti features. Non-LTE radiation-hydrodynamic simulations were used to model the SN and constrain the WD. A delayed detonation and an off-center deflagration-to-detonation transition model is used in order to reproduce the observed narrow ^{58}Ni features. The spectrum produced by the model is shown in Figure 6.4. A high central density is required to produce the observed [CoII]/[CoIII] ratio. The best fit model is consistent with an off-center delayed detonation explosion of a sub-Chandrasekhar Mass WD, 1.37 $M_\odot$, of density 2×10^9 g cm s^{-1} observed equator-on. A mass of ^{56}Ni=0.324 $M_\odot$ and ^{58}Ni=0.06 $M_\odot$ reproduce the observed line widths. The narrow stable Ni lines suggests little central mixing, leading to central carbon burning followed by an off-center deflagration-to-detonation transition.

6.3. Applications

Chapter 6 discusses variable stars and supernovae and the presence and formation of dust in the surrounding material. The presence of dusty cirecumstellar material around variable stars highlight the role of stellar winds and mass loss in dust production. POISE focuses on detailed observations of supernovae in order to understand their explosion mechanics. These observations are also able to track the early formation stages of dust in supernova ejecta. This observational data enriches the understanding of how dust forms, its composition, and how it interacts with the surrounding material.

CHAPTER 7

Discussion & Conclusions

Dust is an important component of the ISM. It locks up information such as nuclear synthesis and abundances of the formation environment. Dust influences astronomical observations through scattering and reddening light. Despite its importance, the origin of dust isn't well understood. This work has explored the nucleation, erosion, and optical properties of dust grains in CCSNe .

In Chapter 2, dust formation in CCSNe was studied in 72 different progenitor models. The progenitor star's explosion energy, mass, and abundance profile were varied. The explosions were evolved until dust formation slowed after three years. The nucleated dust showed strong dependence on the formation environment. In high energy explosions, dust formed at earlier times. The more energetic explosion caused a fast expansion and cooling which produced conditions conducive for nucleation earlier and for a shorter period of time. This resulted in smaller grain sizes in higher energy explosions. A larger amount of silicate grains were also nucleated in the higher explosion energy models. The more energetic models undergo carbon burning, producing more material needed in the formation of silicate grain species.

Once dust grains are formed, they are vulnerable to sputtering and erosion effects of the surrounding medium. The survivability of the grains is heavily dependent on the surrounding conditions. High temperature gas and shock-waves erode dust grains. Chapter 3 describes the codes used to model dust nucleation and destruction. In Chapter 4, the destruction of dust was studied in CCSNe explosion scenarios. The ejecta was expanded until it reached the grid boundaries, representing when the ejecta collides with the ISM, sending a reverse shock back towards the CCSN remnant. The amount of surviving dust material depended strongly on the strength of the reverse shock. The most destruction was seen with intermediate shock temperatures and velocities. Low energy shocks do not deposit large amounts of energy onto dust grains, leading to less erosion and sputtering. High energy shocks pass through dust grains without strongly interacting with them and so cause a reduction in shock erosion. An overall reduction of the average grain size is seen in the majority of shocks. The grains are eroded, shifting the size distribution towards smaller sizes. With shocks causing maximum destruction, the average grain size hardly changes. This is due to smaller grains being completely destroyed, and the larger grains being eroded to smaller sizes.

The surviving grains are deposited into the ISM where they influence observed light. In Chapter 5, the scattering effects of dust are explored and a homegrown Mie scattering code is introduced. The size and composition of dust grains determine the amount and wavelength dependence of scattered light. Larger dust grains affect larger wavelengths while smaller dust grains scatter smaller wavelengths.

Observations of dust and of dust-forming regions are discussed in Chapter 6. The detection of circumstellar dust around variable stars is shown through the analysis of SEDs. The evolution of SNe Ia and CCSNe are tracked to follow the advent of dust formation and to distinguish pre-existing dust.

Future work will continue this research into dust formation and destruction in extreme environments. New physics will be added to the models, such as radioactive decay, coagulation, and accretion. The nucleation of dust will be extended to 2- and 3- dimensions and in new environments, proto-planetary disks and AGNs. It will focus on determining the opacities of varying dust populations in radiation transport models.

Bibliography

Akima, H. 1970, Journal of the ACM (JACM), 17, 589

Andersen, H. H., & Bay, H. L. 1981, in Sputtering by Particle Bombardment I: Physical Sputtering of Single-Element Solids, ed. R. Behrisch, Vol. 47 (Springer), 145, doi: 10.1007/3540105212_9

Andrews, S., Fryer, C., Even, W., Jones, S., & Pignatari, M. 2020, ApJ, 890, 35, doi: 10.3847/1538-4357/ab64f8

Antonucci, R. 1993, ARA&A, 31, 473, doi: 10.1146/annurev.aa.31.090193.002353

Arendt, R. G., Dwek, E., Kober, G., Rho, J., & Hwang, U. 2014, The Astrophysical Journal, 786, 55, doi: 10.1088/0004-637x/786/1/55

Bach, H. 1970, Nuclear Instruments and Methods, 84, 4, doi: 10.1016/0029-554X(70)90728-7

Bach, H., Kitzman, I., & Schröder, H. 1974, Radiation Effects, 21, 31, doi: 10.1080/10420157408230809

Bailey, R. N. 2024, Stellar evolution. https://en.wikipedia.org/wiki/Stellar_evolution#/media/File:Star_Life_Cycle_Chart.jpg

Barlow, M. 1978, Monthly Notices of the Royal Astronomical Society, 183, 367

Barnard, E. E. 1907, ApJ, 25, 218, doi: 10.1086/141434

—. 1910, ApJ, 31, 8, doi: 10.1086/141719

Baskin, A., & Laor, A. 2017, Monthly Notices of the Royal Astronomical Society, 474, 1970, doi: 10.1093/mnras/stx2850

Becker, R., & Döring, W. 1935, Annalen der Physik, 416, 719, doi: 10.1002/andp.19354160806

Behrisch, R., Bohdansky, J., Oetjen, G. H., et al. 1976, Journal of Nuclear Materials, 60, 321, doi: 10.1016/0022-3115(76)90147-1

Behrisch, R., & Eckstein, W. 2007, Sputtering by particle bombardment: Experiments and computer calculations from threshold to MeV energies (Springer)

Bertoldi, F., Carilli, C. L., Cox, P., et al. 2003, A&A, 406, L55, doi: 10.1051/0004-6361:20030710

Bianchi, S., & Schneider, R. 2007, MNRAS, 378, 973, doi: 10.1111/j.1365-2966.2007.11829.x

Biscaro, C., & Cherchneff, I. 2016, A&A, 589, A132, doi: 10.1051/0004-6361/201527769

Blair, W. P., Ghavamian, P., Long, K. S., et al. 2007, ApJ, 662, 998, doi: 10.1086/518414

Blank, P., & Wittmaack, K. 1979, Journal of Applied Physics, 50, 1519, doi: 10.1063/1.326140

Bocchio, M., Marassi, S., Schneider, R., et al. 2016, Astronomy & Astrophysics, 587, A157, doi: 10.1051/0004-6361/201527432

Bohdansky, J. 1984, Nuclear Instruments and Methods in Physics Research B, 2, 587, doi: 10.1016/0168-583X(84)90271-4

Bohdansky, J., Bay, H. L., & Ottenberger, W. 1978, Journal of Nuclear Materials, 76-77, 163, doi: 10.1016/0022-3115(78)90130-7

Borkowski, K. J., Williams, B. J., Reynolds, S. P., et al. 2006, ApJL, 642, L141, doi: 10.1086/504472

Brandt, T. D., & Draine, B. T. 2012, ApJ, 744, 129, doi: 10.1088/0004-637X/744/2/129

Bromm, V. 2013, Reports on Progress in Physics, 76, 112901, doi: 10.1088/0034-4885/76/11/112901

Brooker, E. S., Stangl, S. M., Mauney, C. M., & Fryer, C. L. 2021, Dependence of Dust Formation on the Supernova Explosion and nuDust, doi: 10.2172/1773325

Brooker, E. S., Stangl, S. M., Mauney, C. M., & Fryer, C. L. 2022, ApJ, 931, 85, doi: 10.3847/1538-4357/ac57c3

Burns, C., Hsiao, E., Suntzeff, N., et al. 2021, The Astronomer's Telegram, 14441, 1

Cardelli, J. A., Clayton, G. C., & Mathis, J. S. 1989, ApJ, 345, 245, doi: 10.1086/167900

Christopher Mauney, D. L. 2017, StarChem. https://github.com/lazzati-astro/starchem

Clayton, D. D., & Nittler, L. R. 2004, ARA&A, 42, 39, doi: 10.1146/annurev.astro.42.053102.134022

Coburn, J. W., Winters, H. F., & Chuang, T. J. 1977, Journal of Applied Physics, 48, 3532, doi: 10.1063/1.324150

Czerny, B., & Hryniewicz, K. 2011, A&A, 525, L8, doi: 10.1051/0004-6361/201016025

Danziger, I. J., Gouiffes, C., Bouchet, P., & Lucy, L. B. 1989, IAUC, 4746, 1

De Looze, I., Barlow, M. J., Swinyard, B. M., et al. 2017, MNRAS, 465, 3309, doi: 10.1093/mnras/stw2837

Deirmendjian, D., et al. 1969, Electromagnetic scattering on spherical polydispersions, American Elsevier publishing company New York

DerKacy, J. M., Ashall, C., Hoeflich, P., et al. 2023, ApJL, 945, L2, doi: 10.3847/2041-8213/acb8a8

—. 2024, ApJ, 961, 187, doi: 10.3847/1538-4357/ad0b7b

Desert, F. X., Boulanger, F., & Puget, J. L. 1990, A&A, 237, 215

Draine, B. 1989, in Interstellar Dust, ed. L. J. Allamandola & A. G. G. M. Tielens, Vol. 135, 313

Draine, B. T. 1981, ApJ, 245, 880, doi: 10.1086/158864

—. 1988, ApJ, 333, 848, doi: 10.1086/166795

—. 2003, ARA&A, 41, 241, doi: 10.1146/annurev.astro.41.011802.094840

—. 2011, Physics of the Interstellar and Intergalactic Medium (Princeton University Press)

Draine, B. T., & Flatau, P. J. 1994, J. Opt. Soc. Am. A, 11, 1491, doi: 10.1364/JOSAA.11.001491

Draine, B. T., & Fraisse, A. A. 2009, ApJ, 696, 1, doi: 10.1088/0004-637X/696/1/1

Draine, B. T., & Salpeter, E. E. 1979a, ApJ, 231, 77, doi: 10.1086/157165

—. 1979b, ApJ, 231, 438, doi: 10.1086/157206

Dwek, E. 2005, in American Institute of Physics Conference Series, Vol. 761, The Spectral Energy Distributions of Gas-Rich Galaxies: Confronting Models with Data, ed. C. C. Popescu & R. J. Tuffs, 103–122, doi: 10.1063/1.1913921

Dwek, E., & Arendt, R. G. 2015, The Astrophysical Journal, 810, 75, doi: 10.1088/0004-637x/810/1/75

Dwek, E., Foster, S. M., & Vancura, O. 1996, ApJ, 457, 244, doi: 10.1086/176725

Dwek, E., Arendt, R. G., Bouchet, P., et al. 2008, ApJ, 676, 1029, doi: 10.1086/529038

Edwin, R. P. 1973, Journal of Physics D Applied Physics, 6, 833, doi: 10.1088/0022-3727/6/7/306

EerNisse, E. P. 1971, Journal of Applied Physics, 42, 480, doi: 10.1063/1.1659630

Elvis, M., Marengo, M., & Karovska, M. 2002, ApJL, 567, L107, doi: 10.1086/340006

Fallest, D. W. 2012, PhD thesis, North Carolina State University

Fesen, R. A., Hammell, M. C., Morse, J., et al. 2006, ApJ, 636, 859, doi: 10.1086/498092

Fitzpatrick, E. L. 1999, PASP, 111, 63, doi: 10.1086/316293

Fitzpatrick, E. L., & Massa, D. 1986, ApJ, 307, 286, doi: 10.1086/164415

Frenkel, J. 1939, The Journal of Chemical Physics, 7, 538, doi: 10.1063/1.1750484

Fryer, C., Benz, W., Herant, M., & Colgate, S. A. 1999, ApJ, 516, 892, doi: 10.1086/307119

Fryer, C. L., Andrews, S., Even, W., Heger, A., & Safi-Harb, S. 2018, ApJ, 856, 63, doi: 10.3847/1538-4357/aaaf6f

Fryer, C. L., Hungerford, A. L., & Rockefeller, G. 2007, International Journal of Modern Physics D, 16, 941, doi: 10.1142/S0218271807010523

Gall, C., Hjorth, J., Watson, D., et al. 2014, Nature, 511, 326

Gomez, H. L., Clark, C. J. R., Nozawa, T., et al. 2012, Monthly Notices of the Royal Astronomical Society, 420, 3557

Goumans, T. P. M., & Andersson, S. 2010, Monthly Notices of the Royal Astronomical Society, 406, 2213, doi: 10.1111/j.1365-2966.2010.16836.x

Grefenstette, B. W., Harrison, F. A., Boggs, S. E., et al. 2014, Nature, 506, 339, doi: 10.1038/nature12997

Hall, J. S. 1949, Science, 109, 166, doi: 10.1126/science.109.2825.166

Hall, J. S., & Mikesell, A. H. 1949, AJ, 54, 187, doi: 10.1086/106256

Harris, C. R., Millman, K. J., van der Walt, S. J., et al. 2020, Nature, 585, 357–362, doi: 10.1038/s41586-020-2649-2

Hechtl, E., Bohdansky, J., & Roth, J. 1981, Journal of Nuclear Materials, 103, 333, doi: https://doi.org/10.1016/0022-3115(82)90619-5

Herant, M., Benz, W., Hix, W. R., Fryer, C. L., & Colgate, S. A. 1994, ApJ, 435, 339, doi: 10.1086/174817

Hiltner, W. A. 1949, ApJ, 109, 471, doi: 10.1086/145151

Hindmarsh, A. C. 1983, Scientific computing, 55

Hoeflich, P. 2017, in Handbook of Supernovae, ed. A. W. Alsabti & P. Murdin (Springer), 1151, doi: 10.1007/978-3-319-21846-5_56

Hubeny, I., & Mihalas, D. 2015, Theory of stellar atmospheres: An introduction to astrophysical non-equilibrium quantitative spectroscopic analysis (Princeton University Press)

Humphreys, R. M., Stangl, S., Gordon, M. S., Davidson, K., & Grammer, S. H. 2019a, AJ, 157, 22, doi: 10.3847/1538-3881/aaf1ac

—. 2019b, VizieR Online Data Catalog, J/AJ/157/22, doi: 10.26093/cds/vizier.51570022

Hungerford, A. L., Fryer, C. L., & Rockefeller, G. 2005, ApJ, 635, 487, doi: 10.1086/497323

Hyperphysics. 2023, Blue Sky and Rayleigh Scattering. http://hyperphysics.phy-astr.gsu.edu/hbase/atmos/blusky.html

Indebetouw, R., Matsuura, M., Dwek, E., et al. 2014, The Astrophysical Journal Letters, 782, L2, doi: 10.1088/2041-8205/782/1/L2

Iwamoto, K., Umeda, H., Nakamura, T., & Nomoto, K. 1999, Astronomical Herald, 92, 87

Karthika, S., Radhakrishnan, T. K., & Kalaichelvi, P. 2016, Crystal Growth & Design, 16, 6663, doi: 10.1021/acs.cgd.6b00794

Kashchiev, D. 2000, Nucleation (Elsevier)

Kies, S., Shamim, M. Z., Gregoire, M., et al. 2011, Conference Record - IEEE Instrumentation and Measurement Technology Conference, 1, doi: 10.1109/IMTC.2011.5944117

Kim, S.-H., Martin, P. G., & Hendry, P. D. 1994, ApJ, 422, 164, doi: 10.1086/173714

Kozasa, T., & Hasegawa, H. 1987, Progress of Theoretical Physics, 77, 1402

Krause, O., Birkmann, S. M., Usuda, T., et al. 2008, Science, 320, 1195, doi: 10.1126/science.1155788

Laegreid, N., & Wehner, G. K. 1961, Journal of Applied Physics, 32, 365, doi: 10.1063/1.1736012

Lam, S. K., Pitrou, A., & Seibert, S. 2015, in Proceedings of the Second Workshop on the LLVM Compiler Infrastructure in HPC, LLVM '15 (New York, NY, USA: Association for Computing Machinery), doi: 10.1145/2833157.2833162

Landau, L. D., & Lifshitz, E. M. 1959, Fluid mechanics (Pergamon Press)

Lide, D. 1997, CRC Handbook of Chemistry and Physics, 77th edn. (CRC Press)

Lu, J., Morrell, N., Burns, C., et al. 2022, Transient Name Server Classification Report, 2022-733, 1

Lucy, L. B., Danziger, I. J., Gouiffes, C., & Bouchet, P. 1989, in IAU Colloq. 120: Structure and Dynamics of the Interstellar Medium, ed. G. Tenorio-Tagle, M. Moles, & J. Melnick, Vol. 350, 164, doi: 10.1007/BFb0114861

Marassi, S., Schneider, R., Limongi, M., et al. 2019, Monthly Notices of the Royal Astronomical Society, 484, 2587

Maret, S., & Bergin, E. A. 2015, Astrochem: Abundances of chemical species in the interstellar medium, Astrophysics Source Code Library, record ascl:1507.010. http://ascl.net/1507.010

Marin, L. G., Bejaoui, S., Haggmark, M., et al. 2020, The Astrophysical Journal, 889, 101

Mathis, J. S., Rumpl, W., & Nordsieck, K. H. 1977, ApJ, 217, 425, doi: 10.1086/155591

Matsunami, N., Yamamura, Y., Itikawa, Y., et al. 1981, Radiation Effects, 57, 15, doi: 10.1080/01422448008218676

Matsuura, M., Dwek, E., Meixner, M., et al. 2011, Science, 333, 1258, doi: 10.1126/science.1205983

Matsuura, M., De Buizer, J. M., Arendt, R. G., et al. 2019, Monthly Notices of the Royal Astronomical Society, 482, 1715

Mattsson, L. 2020, Monthly Notices of the Royal Astronomical Society, 499, 6035

Mauney, C., Nardelli, M. B., & Lazzati, D. 2015, The Astrophysical Journal, 800, 30, doi: 10.1088/0004-637x/800/1/30

Mauney, C., & Stangl, S. 2022, lanl/sndust: v2.0, 0.0.3, Zenodo, doi: 10.5281/zenodo.6111944

McBride, B. J. 1993, Coefficients for calculating thermodynamic and transport properties of individual species, Vol. 4513 (NASA Langley Research Center)

Minissale, M., Congiu, E., Baouche, S., et al. 2013, Phys. Rev. Lett., 111, 053201, doi: 10.1103/PhysRevLett.111.053201

Müller, B., Heger, A., Liptai, D., & Cameron, J. B. 2016, Monthly Notices of the Royal Astronomical Society, 460, 742

Nanni, A., Burgarella, D., Theulé, P., Côté, B., & Hirashita, H. 2020, A&A, 641, A168, doi: 10.1051/0004-6361/202037833

National Institute of Standards and Technology (NIST). 2023, NIST Chemistry WebBook. https://webbook.nist.gov/chemistry/name-ser/

Nenadović, T., Perraillon, B., Bogdanov, Ž., Djordjević, Z., & Milić, M. 1990, Nuclear Instruments and Methods in Physics Research B, 48, 538, doi: 10.1016/0168-583X(90)90178-W

Nozawa, T., & Kozasa, T. 2013, The Astrophysical Journal, 776, 24, doi: 10.1088/0004-637x/776/1/24

Nozawa, T., Kozasa, T., & Habe, A. 2006, The Astrophysical Journal, 648, 435, doi: 10.1086/505639

Nozawa, T., Kozasa, T., Habe, A., et al. 2007, The Astrophysical Journal, 666, 955, doi: 10.1086/520621

Nozawa, T., Kozasa, T., Tominaga, N., et al. 2010, ApJ, 713, 356, doi: 10.1088/0004-637X/713/1/356

Nozawa, T., Kozasa, T., Umeda, H., Maeda, K., & Nomoto, K. 2003, The Astrophysical Journal, 598, 785, doi: 10.1086/379011

Nyquist, R. M., Talanquer, V., & Oxtoby, D. W. 1995, The Journal of Chemical Physics, 103, 1175, doi: 10.1063/1.469827

Paquette, J., Nuth, J., & Ferguson, F. 2023, in American Astronomical Society Meeting Abstracts, Vol. 55, American Astronomical Society Meeting Abstracts, 234.04

Priestley, F. D., Barlow, M. J., & De Looze, I. 2019, MNRAS, 485, 440, doi: 10.1093/mnras/stz414

Reboussin, L., Wakelam, V., Guilloteau, S., & Hersant, F. 2014, MNRAS, 440, 3557, doi: 10.1093/mnras/stu462

Rosen, A. L., & Krumholz, M. R. 2020, AJ, 160, 78, doi: 10.3847/1538-3881/ab9abf

Rosenber, D., & Wehner, G. K. 1962, Journal of Applied Physics, 33, 1842

Roth, J., Bohdansky, J., Poschenrieder, W., & Sinha, M. K. 1976, Journal of Nuclear Materials, 63, 222, doi: 10.1016/0022-3115(76)90213-0

Rudnick, J. 1936, ApJ, 83, 394, doi: 10.1086/143733

Sadavoy, S., Matsuura, M., Armus, L., et al. 2019, BAAS, 51, 66. https://arxiv.org/abs/1904.10994

Sankrit, R., Williams, B. J., Borkowski, K. J., et al. 2010, ApJ, 712, 1092, doi: 10.1088/0004-637X/712/2/1092

Sarangi, A., & Cherchneff, I. 2013, The Astrophysical Journal, 776, 107, doi: 10.1088/0004-637X/776/2/107

Sarangi, A., & Cherchneff, I. 2015, A&A, 575, A95, doi: 10.1051/0004-6361/201424969

Savage, B. D., & Sembach, K. R. 1996, ARA&A, 34, 279, doi: 10.1146/annurev.astro.34.1.279

Serkowski, K. 1973, in Interstellar Dust and Related Topics, ed. J. M. Greenberg & H. C. van de Hulst, Vol. 52, 145

Shahbandeh, M., Ashall, C., Hoeflich, P., et al. 2024, arXiv e-prints, arXiv:2401.14474, doi: 10.48550/arXiv.2401.14474

Shi, Y., Rieke, G. H., Hines, D. C., et al. 2006, The Astrophysical Journal, 653, 127, doi: 10.1086/508737

Sigmund, P. 1981, Sputtering by Particle Bombardment I (Springer-Verlag Berlin Heidelberg)

Slavin, J. D., Dwek, E., & Jones, A. P. 2015, ApJ, 803, 7, doi: 10.1088/0004-637X/803/1/7

Sluder, A., Milosavljević, M., & Montgomery, M. H. 2018, Monthly Notices of the Royal Astronomical Society, 480, 5580, doi: 10.1093/mnras/sty2060

Sommerfeldt, H., Mashkova, E. S., & Molchanov, V. A. 1972, Physics Letters A, 38, 237, doi: 10.1016/0375-9601(72)90059-X

Southern, A. L., Willis, W. R., & Robinson, M. T. 1963, Journal of Applied Physics, 34, 153, doi: 10.1063/1.1729057

Stacey, W., Smith, D., Brooks, J., Bertoncini, P., & Ehst, D. 1977, ANL/FPP Technical Memorandum

Stammler, S. M., & Birnstiel, T. 2022, ApJ, 935, 35, doi: 10.3847/1538-4357/ac7d58

Stangl, S. 2022, OSTI OAI (U.S. Department of Energy Office of Scientific and Technical Information), doi: 10.11578/dc.20220729.1

—. 2023, OSTI OAI (U.S. Department of Energy Office of Scientific and Technical Information), doi: 10.11578/dc.20230922.7

Stangl, S. M., Mauney, C. M., Brooker, E. S., & Fryer, C. L. 2024, ApJ

Tielens, A. G. G. M., McKee, C. F., Seab, C. G., & Hollenbach, D. J. 1994, ApJ, 431, 321, doi: 10.1086/174488

Todini, P., & Ferrara, A. 2001, MNRAS, 325, 726, doi: 10.1046/j.1365-8711.2001.04486.x

Triani, D. P., Sinha, M., Croton, D. J., Pacifici, C., & Dwek, E. 2020, Monthly Notices of the Royal Astronomical Society, 493, 2490

Trumpler, R. J. 1930, PASP, 42, 214, doi: 10.1086/124039

Vehkamäki, H. 2006, Classical nucleation theory in multicomponent systems (Springer Science & Business Media)

Villata, M. 1992, Astronomy and Astrophysics, 257, 677

Virtanen, P., Gommers, R., Oliphant, T. E., et al. 2020, Nature Methods, 17, 261, doi: 10.1038/s41592-019-0686-2

Volmer, M., & Weber, A. 1926, Zeitschrift für Physikalische Chemie, 119U, 277, doi: doi:10.1515/zpch-1926-11927

Von Seefeld, H., Schmidl, H., Behrisch, R., & Scherzer, B. M. U. 1976, Journal of Nuclear Materials, 63, 215, doi: 10.1016/0022-3115(76)90212-9

Watson, D., Christensen, L., Knudsen, K. K., et al. 2015, Nature, 519, 327, doi: 10.1038/nature14164

Weingartner, J. C., & Draine, B. T. 2001, ApJ, 548, 296, doi: 10.1086/318651

Welty, D. E., & Fowler, J. R. 1992, ApJ, 393, 193, doi: 10.1086/171497

Wesson, R., Barlow, M., Matsuura, M., & Ercolano, B. 2015, Monthly Notices of the Royal Astronomical Society, 446, 2089, doi: 10.1093/mnras/stu2250

Williams, B. J., & Temim, T. 2016, in Handbook of Supernovae (Living Reference Work Entry, 1, doi: 10.1007/978-3-319-20794-0_94-1

Williams, B. J., Borkowski, K. J., Reynolds, S. P., et al. 2006, ApJL, 652, L33, doi: 10.1086/509876

Wolf, S., & Voshchinnikov, N. 2004, Computer Physics Communications, 162, 113, doi: https://doi.org/10.1016/j.cpc.2004.06.070

Wooden, D. H., Rank, D. M., Bregman, J. D., et al. 1993, ApJS, 88, 477, doi: 10.1086/191830

Zeng, X. C., & Oxtoby, D. W. 1991, The Journal of Chemical Physics, 95, 5940, doi: 10.1063/1.461615

Zickgraf, F.-J., & Humphreys, R. M. 1991, AJ, 102, 113, doi: 10.1086/115860

Zubko, V., Dwek, E., & Arendt, R. G. 2004, ApJS, 152, 211, doi: 10.1086/382351

CHAPTER A

Appendix

A.1. Dust Tables

In this Appendix are the data tables for Brooker et al. (2022). Data Table A.1 contains information about the supernova models Fryer et al. (2018) used in this dust formation study. The columns, in order, of Table A.1 give the model name designation, the mass of the progenitor star pre-explosion, the mass contained in the shock rebound, the injection mass, the injection time, the injection energy, the final explosion energy, and the mass of the remnant after explosion. In Table A.2, we list the nuclear isotopes provided in the supernova models for completeness. These isotopes listed in Table A.2 are summed up to provide the simple elemental abundances for our dust formation code. And finally, we have Table A.3 containing the final dust grain masses of each supernova model after 1157 days post-explosion. We only report 11 dust grain species, selecting the most abundant species at the snapshot time and a few interesting species such as SiC and TiC. We neglect to report the pure metal grains, such as V, Fe, Ni, due to a very low formation rate for most models at this time and in general these metal grains are not a primary focus of this study.

Table A.1. List of models used from Fryer et al. (2018).

Model	M_{prog} ($\mathrm{M}_\odot$)	M_{bounce} ($\mathrm{M}_\odot$)	M_{inj} ($\mathrm{M}_\odot$)	t_{inj} (s)	E_{inj} 10^{51} erg	E_{exp} 10^{51} erg	M_{rem} ($\mathrm{M}_\odot$)
M15aE0.34	15	1.30	0.3	0.1	3	0.34	1.94
M15aE0.54	15	1.30	0.3	0.1	4	0.54	1.91
M15aE0.82	15	1.30	0.3	0.1	5	0.82	1.88
M15aE2.47	15	1.30	0.3	0.1	9	2.47	1.52
M15aE4.79	15	1.30	0.3	0.4	20	4.79	1.50
M15bE0.30	15	1.30	0.02	0.4	3	0.3	1.71
M15bE0.52	15	1.30	0.02	0.2	5	0.52	1.71
M15bE0.74	15	1.30	0.02	0.4	3	0.74	1.73
M15bE0.82	15	1.30	0.02	0.2	6	0.82	1.71
M15bE0.89	15	1.30	0.02	0.2	5	0.89	1.74
M15bE0.92	15	1.30	0.02	0.3	4	0.92	1.75
M15bE1.69	15	1.30	0.02	0.2	10	1.69	1.52
M15bE2.63	15	1.30	0.02	0.2	20	2.63	1.53
M15bE10.7	15	1.30	0.02	0.2	80	10.7	1.53
M15cE2.06	15	1.30	0.1	0.3	15	2.06	1.59
M15cE1.94	15	1.30	0.1	0.3	12	1.94	1.61
M15cE1.90	15	1.30	0.1	0.3	10	1.90	1.62
M15cE1.86	15	1.30	0.1	0.3	9	1.86	1.63
M15cE2.24	15	1.30	0.1	0.3	25	2.24	1.56
M15cE2.60	15	1.30	0.1	0.3	45	2.60	1.52
M15cE3.43	15	1.30	0.1	0.3	90	3.43	1.51
M20aE0.53	20	1.56	0.1	0.50	4	0.53	3.40
M20aE0.65	20	1.56	0.1	0.12	4	0.65	3.03
M20aE0.81	20	1.56	0.1	0.12	7	0.81	2.70
M20aE0.85	20	1.56	0.1	0.50	7	0.85	2.62
M20aE1.39	20	1.56	0.1	0.12	10	1.39	1.93
M20aE1.47	20	1.56	0.1	0.50	10	1.47	2.23
M20aE2.43	20	1.56	0.1	0.12	20	2.43	1.86

Table A.1 (cont'd)

Model	M_{prog} (M$_\odot$)	M_{bounce} (M$_\odot$)	M_{inj} (M$_\odot$)	t_{inj} (s)	E_{inj} 10^{51} erg	E_{exp} 10^{51} erg	M_{rem} (M$_\odot$)
M20aE2.50	20	1.56	0.1	0.50	20	2.50	1.93
M20aE4.15	20	1.56	0.1	0.12	50	4.15	1.85
M20bE0.78	20	1.56	0.2	0.12	5	0.78	2.85
M20bE1.04	20	1.56	0.2	0.12	6	1.04	2.47
M20bE1.19	20	1.56	0.2	0.12	8	1.19	2.28
M20bE1.52	20	1.56	0.2	0.12	10	1.52	1.97
M20bE2.60	20	1.56	0.2	0.12	25	2.60	1.90
M20bE4.33	20	1.56	0.2	0.12	50	4.33	1.87
M20cE0.75	20	1.47	0.1	0.5	6	0.75	2.76
M20cE0.84	20	1.47	0.1	0.5	7	0.84	2.62
M20cE1.00	20	1.47	0.1	0.5	8	1.00	2.35
M20cE1.65	20	1.47	0.1	0.5	10	1.65	1.78
M20cE2.76	20	1.47	0.1	0.5	15	2.76	1.76
M20cE2.85	20	1.47	0.1	0.5	20	2.85	1.74
M20cE5.03	20	1.47	0.1	0.5	50	5.03	1.74
M20cE8.86	20	1.47	0.1	0.5	100	8.86	1.74
M20dE4.33	20	1.56	0.2	0.12	50	4.33	1.87
M20dE5.90	20	1.47	0.2	0.5	20	5.9	1.74
M20dE18.1	20	1.47	0.2	0.5	50	18.1	1.74
M20dE64.5	20	1.47	0.2	0.5	75	64.5	1.74
M20dE78.9	20	1.47	0.2	0.5	100	78.9	1.74
M20dE88.4	20	1.47	0.2	0.5	125	88.4	1.74
M20dE124	20	1.47	0.2	0.5	150	124	1.74
M25aE0.99	25	1.83	0.1	0.1	5.0	0.99	4.89
M25aE1.57	25	1.83	0.1	0.1	10	1.57	3.73
M25aE4.73	25	1.83	0.1	0.1	20	4.73	2.38
M25aE6.17	25	1.83	0.1	0.1	35	6.17	2.38
M25aE7.42	25	1.83	0.1	0.1	50	7.42	2.37

Table A.1 (cont'd)

Model	M_{prog} (M$_\odot$)	M_{bounce} (M$_\odot$)	M_{inj} (M$_\odot$)	t_{inj} (s)	E_{inj} 10^{51} erg	E_{exp} 10^{51} erg	M_{rem} (M$_\odot$)
M25aE14.8	25	1.83	0.1	0.1	100	14.8	2.35
M25bE8.40	25	1.83	0.02	0.28	50.0	8.40	2.38
M25bE9.73	25	1.83	0.02	0.69	100	9.73	2.35
M25bE18.4	25	1.83	0.02	0.69	200	18.4	2.35
M25d3E0.89	25	1.83	0.02	0.7	7	0.89	4.66
M25d3E0.92	25	1.83	0.02	0.7	8	0.92	1.84
M25d3E1.04	25	1.83	0.02	0.7	10	1.04	1.84
M25d3E1.20	25	1.83	0.02	0.7	50	1.20	1.84
M25d2E2.53	25	1.83	0.02	0.7	20	2.53	2.35
M25d2E2.64	25	1.83	0.02	0.7	35	2.64	2.35
M25d2E2.78	25	1.83	0.02	0.7	50	2.78	2.35
M25d2E3.07	25	1.83	0.02	0.7	100	3.07	1.83
M25d1E3.30	25	1.83	0.02	0.7	25	3.30	2.35
M25d1E4.72	25	1.83	0.02	0.7	50	4.72	2.35
M25d1E7.08	25	1.83	0.02	0.7	100	7.08	2.35

Note. — List of supernova models used organized by progenitor mass denoted by uppercase "M" with progenitor mass in the model name. For each progenitor mass, lowercase alphabetic characters denote supernova engine subgroups. Subgroups are order by increasing explosion energy denoted with uppercase "E" and the explosion energy in the model name. Table columns: 1) Model, 2) Progenitor mass, M_{prog}, 3) Shock rebound mass, M_{bounce}, 4) Injection mass, M_{inj}, 5) Injection time, t_{inj}, 6) Injection energy, E_{inj}, 7) Final explosion energy, E_{exp}, 8) Mass of remnant, M_{rem}.

Table A.2. Table of Isotopes

H 2	O 21	MG 43	P 37	CL 43	K 40	CA 72	TI 60	CR 42	MN 68
HE 3	O 22	MG 44	P 38	CL 44	K 41	CA 73	TI 61	CR 43	MN 69
HE 4	F 20	MG 45	P 39	CL 45	K 42	SC 32	TI 62	CR 44	MN 70
BE 7	F 21	MG 46	P 40	CL 46	K 43	SC 33	TI 63	CR 45	MN 71
B 8	F 22	MG 47	P 41	CL 47	K 44	SC 34	TI 64	CR 46	MN 72
LI 7	F 23	AL 21	P 42	CL 48	K 45	SC 35	TI 65	CR 47	MN 73
C 11	F 24	AL 22	P 43	CL 49	K 46	SC 36	TI 66	CR 48	MN 74
B 11	F 25	AL 23	P 44	CL 50	K 47	SC 37	TI 67	CR 49	MN 75
C 12	F 26	AL 24	P 45	CL 51	K 48	SC 38	TI 68	CR 50	MN 76
C 13	NE 17	AL 28	P 46	CL 52	K 49	SC 39	TI 69	CR 51	MN 77
N 13	NE 18	AL 29	P 47	CL 53	K 50	SC 40	TI 70	CR 52	MN 78
N 14	NE 19	AL 30	P 48	CL 54	K 51	SC 41	TI 71	CR 53	MN 79
C 14	NE 23	AL 31	P 49	CL 55	K 52	SC 42	TI 72	CR 54	MN 80
N 15	NE 24	AL 32	P 50	CL 56	K 53	SC 43	TI 73	CR 55	MN 81
O 16	NE 25	AL 33	P 51	CL 57	K 54	SC 44	TI 74	CR 56	MN 82
O 17	NE 26	AL 34	P 52	CL 58	K 55	SC 45	TI 75	CR 57	MN 83
O 18	NE 27	AL 35	P 53	CL 59	K 56	SC 46	TI 76	CR 58	MN 84
F 17	NE 28	AL 36	P 54	CL 60	K 57	SC 47	TI 77	CR 59	MN 85
F 18	NE 29	AL 37	P 55	CL 61	K 58	SC 48	TI 78	CR 60	MN 86
F 19	NE 30	AL 38	P 56	CL 62	K 59	SC 49	TI 79	CR 61	MN 87
NE 20	NE 31	AL 39	P 57	CL 63	K 60	SC 50	TI 80	CR 62	MN 88
NE 21	NE 32	AL 40	S 25	AR 27	K 61	SC 51	V 36	CR 63	MN 89
NE 22	NE 33	AL 41	S 26	AR 28	K 62	SC 52	V 37	CR 64	FE 42
NA 22	NE 34	AL 42	S 27	AR 29	K 63	SC 53	V 38	CR 65	FE 43
NA 23	NE 35	AL 43	S 28	AR 30	K 64	SC 54	V 39	CR 66	FE 44
MG 23	NE 36	AL 44	S 29	AR 31	K 65	SC 55	V 40	CR 67	FE 45
MG 24	NE 37	AL 45	S 30	AR 32	K 66	SC 56	V 41	CR 68	FE 46
MG 25	NE 38	AL 46	S 32	AR 33	K 67	SC 57	V 42	CR 69	FE 47
MG 26	NE 39	AL 47	S 33	AR 34	K 68	SC 58	V 43	CR 70	FE 48

Table A.2 (cont'd)

AL 26	NE 40	AL 48	S 34	AR 35	K 69	SC 59	V 44	CR 71	FE 49
AL 27	NE 41	AL 49	S 35	AR 36	K 70	SC 60	V 45	CR 72	FE 50
SI 27	NA 19	AL 50	S 36	AR 37	CA 30	SC 61	V 46	CR 73	FE 51
SI 28	NA 20	AL 51	S 37	AR 38	CA 31	SC 62	V 47	CR 74	FE 52
SI 29	NA 24	SI 22	S 38	AR 39	CA 32	SC 63	V 48	CR 75	FE 53
SI 30	NA 25	SI 23	S 39	AR 40	CA 33	SC 64	V 49	CR 76	FE 54
P 31	NA 26	SI 24	S 40	AR 41	CA 34	SC 65	V 50	CR 77	FE 55
S 31	NA 27	SI 25	S 41	AR 42	CA 35	SC 66	V 51	CR 78	FE 56
BE 8	NA 28	SI 26	S 42	AR 43	CA 36	SC 67	V 52	CR 79	FE 57
O 14	NA 29	SI 31	S 43	AR 44	CA 37	SC 68	V 53	CR 80	FE 58
O 15	NA 30	SI 32	S 44	AR 45	CA 38	SC 69	V 54	CR 81	FE 59
NA 21	NA 31	SI 33	S 45	AR 46	CA 39	SC 70	V 55	CR 82	FE 60
AL 25	NA 32	SI 34	S 46	AR 47	CA 40	SC 71	V 56	CR 83	FE 61
P 29	NA 33	SI 35	S 47	AR 48	CA 41	SC 72	V 57	CR 84	FE 62
P 30	NA 34	SI 36	S 48	AR 49	CA 42	SC 73	V 58	CR 85	FE 63
PB 206	NA 35	SI 37	S 49	AR 50	CA 43	SC 74	V 59	CR 86	FE 64
PB 207	NA 36	SI 38	S 50	AR 51	CA 44	SC 75	V 60	MN 40	FE 65
BI 211	NA 37	SI 39	S 51	AR 52	CA 45	SC 76	V 61	MN 41	FE 66
PO 210	NA 38	SI 40	S 52	AR 53	CA 46	TI 34	V 62	MN 42	FE 67
H 3	NA 39	SI 41	S 53	AR 54	CA 47	TI 35	V 63	MN 43	FE 68
HE 6	NA 40	SI 42	S 54	AR 55	CA 48	TI 36	V 64	MN 44	FE 69
LI 8	NA 41	SI 43	S 55	AR 56	CA 49	TI 37	V 65	MN 45	FE 70
LI 9	NA 42	SI 44	S 56	AR 57	CA 50	TI 38	V 66	MN 46	FE 71
BE 10	NA 43	SI 45	S 57	AR 58	CA 51	TI 39	V 67	MN 47	FE 72
BE 11	NA 44	SI 46	S 58	AR 59	CA 52	TI 40	V 68	MN 48	FE 73
BE 12	MG 20	SI 47	S 59	AR 60	CA 53	TI 41	V 69	MN 49	FE 74
B 12	MG 21	SI 48	S 60	AR 61	CA 54	TI 42	V 70	MN 50	FE 75
B 13	MG 22	SI 49	CL 26	AR 62	CA 55	TI 43	V 71	MN 51	FE 76
B 14	MG 27	SI 50	CL 27	AR 63	CA 56	TI 44	V 72	MN 52	FE 77

Table A.2 (cont'd)

C 15	MG 28	SI 51	CL 28	AR 64	CA 57	TI 45	V 73	MN 53	FE 78
C 16	MG 29	SI 52	CL 29	AR 65	CA 58	TI 46	V 74	MN 54	FE 79
C 17	MG 30	SI 53	CL 30	AR 66	CA 59	TI 47	V 75	MN 55	FE 80
C 18	MG 31	SI 54	CL 31	AR 67	CA 60	TI 48	V 76	MN 56	FE 81
N 11	MG 32	P 23	CL 32	K 29	CA 61	TI 49	V 77	MN 57	FE 82
N 12	MG 33	P 24	CL 33	K 30	CA 62	TI 50	V 78	MN 58	FE 83
N 16	MG 34	P 25	CL 34	K 31	CA 63	TI 51	V 79	MN 59	FE 84
N 17	MG 35	P 26	CL 35	K 32	CA 64	TI 52	V 80	MN 60	FE 85
N 18	MG 36	P 27	CL 36	K 33	CA 65	TI 53	V 81	MN 61	FE 86
N 19	MG 37	P 28	CL 37	K 34	CA 66	TI 54	V 82	MN 62	FE 87
N 20	MG 38	P 32	CL 38	K 35	CA 67	TI 55	V 83	MN 63	FE 88
N 21	MG 39	P 33	CL 39	K 36	CA 68	TI 56	CR 38	MN 64	FE 89
O 13	MG 40	P 34	CL 40	K 37	CA 69	TI 57	CR 39	MN 65	FE 90
O 19	MG 41	P 35	CL 41	K 38	CA 70	TI 58	CR 40	MN 66	FE 91
O 20	MG 42	P 36	CL 42	K 39	CA 71	TI 59	CR 41	MN 67	FE 92

Note. — List of Isotopes used in the abundances of each model

Table A.3. Dust mass for specific species and total dust mass produced per model by 1157 days after explosion.

Dust Species	Models							
	M15aE0.34	M15aE0.54	M15aE0.82	M15aE2.47	M15aE4.79	M15bE0.3	M15bE0.52	M15bE0.74
C	1.19×10^{-15}	6.96×10^{-7}	2.26×10^{-2}	4.47×10^{-2}	4.64×10^{-2}	1.27×10^{-5}	6.98×10^{-4}	2.14×10^{-2}
SiC	6.98×10^{-34}	6.17×10^{-15}	1.11×10^{-12}	2.67×10^{-12}	2.26×10^{-10}	7.34×10^{-14}	2.20×10^{-12}	3.45×10^{-12}
TiC	0	4.01×10^{-30}	1.47×10^{-12}	3.83×10^{-12}	7.53×10^{-13}	0	5.26×10^{-15}	9.95×10^{-13}
Si	0	0	0	2.77×10^{-10}	2.26×10^{-8}	0	0	0
SiO_2	5.86×10^{-7}	3.72×10^{-7}	2.28×10^{-7}	8.15×10^{-8}	1.47×10^{-2}	6.99×10^{-7}	4.18×10^{-7}	2.69×10^{-7}
$MgSiO_3$	3.43×10^{-6}	2.14×10^{-6}	1.28×10^{-6}	4.69×10^{-7}	9.30×10^{-4}	4.06×10^{-6}	2.38×10^{-6}	1.51×10^{-6}
Mg_2SiO_4	2.70×10^{-5}	1.68×10^{-5}	1.00×10^{-5}	3.71×10^{-6}	1.23×10^{-1}	3.21×10^{-5}	1.87×10^{-5}	1.19×10^{-5}
MgO	6.42×10^{-8}	4.08×10^{-8}	2.51×10^{-8}	8.78×10^{-9}	3.46×10^{-8}	7.67×10^{-8}	4.61×10^{-8}	2.95×10^{-8}
Al_2O_3	1.26×10^{-6}	7.80×10^{-7}	4.77×10^{-7}	1.70×10^{-2}	1.71×10^{-2}	1.47×10^{-6}	8.57×10^{-7}	5.59×10^{-7}
FeO	7.39×10^{-6}	5.01×10^{-6}	3.25×10^{-6}	1.23×10^{-6}	4.66×10^{-7}	8.64×10^{-6}	5.58×10^{-6}	3.76×10^{-6}
Fe_3O_4	1.05×10^{-4}	7.07×10^{-5}	4.52×10^{-5}	1.73×10^{-5}	7.01×10^{-6}	1.22×10^{-4}	7.84×10^{-5}	5.27×10^{-5}
Total	1.45×10^{-4}	9.69×10^{-5}	2.26×10^{-2}	6.18×10^{-2}	2.02×10^{-1}	1.83×10^{-4}	8.05×10^{-4}	2.14×10^{-2}
	M15bE0.82	M15bE0.89	M15bE0.92	M15bE1.69	M15bE2.63	M15bE10.7	M15cE2.06	M15cE1.94
C	3.87×10^{-3}	4.34×10^{-2}	4.31×10^{-2}	4.47×10^{-2}	4.48×10^{-2}	4.47×10^{-2}	4.47×10^{-2}	4.47×10^{-2}
SiC	3.37×10^{-12}	5.84×10^{-12}	6.10×10^{-12}	2.11×10^{-12}	3.56×10^{-10}	6.54×10^{-12}	1.13×10^{-12}	1.24×10^{-12}
TiC	1.28×10^{-12}	3.97×10^{-12}	4.89×10^{-12}	2.61×10^{-12}	1.96×10^{-12}	9.59×10^{-12}	1.17×10^{-12}	1.29×10^{-12}
Si	0	0	0	2.87×10^{-11}	7.98×10^{-8}	3.66×10^{-28}	6.31×10^{-10}	1.20×10^{-10}
SiO_2	3.12×10^{-7}	2.07×10^{-7}	2.00×10^{-7}	9.71×10^{-8}	5.74×10^{-8}	1.72×10^{-7}	7.36×10^{-8}	7.90×10^{-8}
$MgSiO_3$	1.75×10^{-6}	1.16×10^{-6}	1.12×10^{-6}	5.57×10^{-7}	5.54×10^{-4}	9.74×10^{-7}	1.83×10^{-6}	1.47×10^{-6}

Table A.3 (cont'd)

Dust Species	Models							
Mg_2SiO_4	1.37×10^{-5}	9.17×10^{-6}	8.84×10^{-6}	4.82×10^{-6}	1.20×10^{-1}	7.65×10^{-6}	7.90×10^{-2}	6.43×10^{-2}
MgO	3.43×10^{-8}	2.29×10^{-8}	2.21×10^{-8}	1.05×10^{-8}	6.11×10^{-9}	1.89×10^{-8}	7.90×10^{-9}	8.49×10^{-9}
Al_2O_3	6.42×10^{-7}	4.36×10^{-7}	4.21×10^{-7}	1.89×10^{-2}	1.74×10^{-2}	1.57×10^{-4}	1.83×10^{-2}	1.84×10^{-2}
FeO	4.30×10^{-6}	2.99×10^{-6}	2.89×10^{-6}	1.46×10^{-6}	8.85×10^{-7}	2.51×10^{-6}	1.12×10^{-6}	1.20×10^{-6}
Fe_3O_4	6.02×10^{-5}	4.14×10^{-5}	3.99×10^{-5}	2.04×10^{-5}	1.25×10^{-5}	3.48×10^{-5}	1.58×10^{-5}	1.68×10^{-5}
Total	3.96×10^{-3}	4.34×10^{-2}	4.31×10^{-2}	6.37×10^{-2}	1.83×10^{-1}	4.49×10^{-2}	1.42×10^{-1}	1.27×10^{-1}
	M15cE1.90	M15cE1.86	M15cE2.24	M15cE2.60	M15cE3.43	M20aE0.53	M20aE0.65	M20aE0.81
C	4.47×10^{-2}	4.47×10^{-2}	4.47×10^{-2}	4.47×10^{-2}	4.48×10^{-2}	2.36×10^{-2}	2.37×10^{-2}	2.37×10^{-2}
SiC	1.26×10^{-12}	1.34×10^{-12}	1.21×10^{-12}	4.86×10^{-10}	3.61×10^{-10}	3.72×10^{-12}	5.40×10^{-12}	6.39×10^{-12}
TiC	1.32×10^{-12}	1.41×10^{-12}	1.06×10^{-12}	8.59×10^{-13}	6.09×10^{-13}	4.57×10^{-17}	6.76×10^{-13}	1.03×10^{-11}
Si	5.04×10^{-11}	1.40×10^{-11}	2.67×10^{-9}	1.40×10^{-8}	1.29×10^{-8}	0	0	0
SiO_2	8.09×10^{-8}	8.60×10^{-8}	6.66×10^{-8}	5.70×10^{-8}	1.11×10^{-2}	4.53×10^{-7}	3.84×10^{-7}	3.34×10^{-7}
$MgSiO_3$	1.08×10^{-6}	5.49×10^{-7}	1.46×10^{-4}	4.15×10^{-4}	7.02×10^{-4}	2.68×10^{-6}	2.35×10^{-6}	1.85×10^{-6}
Mg_2SiO_4	4.06×10^{-2}	1.41×10^{-3}	1.15×10^{-1}	1.28×10^{-1}	1.28×10^{-1}	2.11×10^{-5}	1.88×10^{-5}	1.47×10^{-5}
MgO	8.71×10^{-9}	9.27×10^{-9}	7.13×10^{-9}	6.03×10^{-9}	2.75×10^{-7}	4.88×10^{-8}	4.16×10^{-8}	3.42×10^{-8}
Al_2O_3	1.84×10^{-2}	1.84×10^{-2}	1.83×10^{-2}	1.82×10^{-2}	1.82×10^{-2}	1.00×10^{-6}	8.24×10^{-7}	1.83×10^{-3}
FeO	1.22×10^{-6}	1.30×10^{-6}	1.02×10^{-6}	8.61×10^{-7}	6.86×10^{-7}	5.91×10^{-6}	5.17×10^{-6}	4.36×10^{-6}
Fe_3O_4	1.72×10^{-5}	1.82×10^{-5}	1.43×10^{-5}	1.24×10^{-5}	1.04×10^{-5}	8.39×10^{-5}	7.28×10^{-5}	6.31×10^{-5}
Total	1.03×10^{-1}	6.46×10^{-2}	1.78×10^{-1}	1.92×10^{-1}	2.03×10^{-1}	2.37×10^{-2}	2.38×10^{-2}	2.56×10^{-2}
	M20aE0.85	M20aE1.39	M20aE1.47	M20aE2.43	M20aE2.50	M20aE4.15	M20bE0.78	M20bE1.04

Table A.3 (cont'd)

Dust Species	Models							
C	2.37×10^{-2}	2.37×10^{-2}	2.37×10^{-2}	2.37×10^{-2}	2.37×10^{-2}	2.38×10^{-2}	2.37×10^{-2}	2.37×10^{-2}
SiC	6.53×10^{-12}	6.17×10^{-12}	4.88×10^{-12}	3.55×10^{-12}	3.57×10^{-12}	2.60×10^{-12}	6.52×10^{-12}	6.19×10^{-12}
TiC	1.10×10^{-11}	1.41×10^{-11}	9.82×10^{-12}	8.09×10^{-12}	7.95×10^{-12}	5.89×10^{-12}	1.08×10^{-11}	1.36×10^{-11}
Si	0	1.34×10^{-15}	1.86×10^{-11}	5.35×10^{-7}	3.15×10^{-7}	2.85×10^{-7}	0	1.12×10^{-30}
SiO_2	3.18×10^{-7}	3.23×10^{-7}	3.20×10^{-7}	2.51×10^{-7}	2.47×10^{-7}	2.90×10^{-2}	3.34×10^{-7}	2.52×10^{-7}
$MgSiO_3$	1.75×10^{-6}	4.36×10^{-6}	4.14×10^{-6}	3.40×10^{-6}	3.48×10^{-6}	8.33×10^{-4}	1.94×10^{-6}	5.05×10^{-6}
Mg_2SiO_4	1.39×10^{-5}	4.06×10^{-2}	3.00×10^{-2}	6.10×10^{-2}	5.62×10^{-2}	8.59×10^{-2}	1.54×10^{-5}	4.28×10^{-3}
MgO	3.31×10^{-8}	1.96×10^{-7}	5.85×10^{-7}	6.71×10^{-7}	6.93×10^{-7}	8.43×10^{-7}	3.55×10^{-8}	2.78×10^{-8}
Al_2O_3	3.88×10^{-3}	1.85×10^{-2}	1.34×10^{-2}	1.15×10^{-2}	8.38×10^{-3}	9.92×10^{-3}	1.27×10^{-3}	7.87×10^{-3}
FeO	4.24×10^{-6}	2.63×10^{-6}	4.40×10^{-6}	3.31×10^{-6}	3.27×10^{-6}	2.37×10^{-6}	4.51×10^{-6}	3.60×10^{-6}
Fe_3O_4	6.02×10^{-5}	6.80×10^{-5}	6.75×10^{-5}	5.26×10^{-5}	5.24×10^{-5}	3.89×10^{-5}	6.49×10^{-5}	4.88×10^{-5}
Total	2.77×10^{-2}	8.30×10^{-2}	6.73×10^{-2}	9.64×10^{-2}	8.84×10^{-2}	1.49×10^{-1}	2.51×10^{-2}	3.59×10^{-2}
	M20bE1.19	M20bE1.52	M20bE2.60	M20bE4.33	M20cE0.75	M20cE0.84	M20cE1.00	M20cE1.65
C	2.37×10^{-2}	2.37×10^{-2}	2.37×10^{-2}	2.38×10^{-2}	2.37×10^{-2}	2.37×10^{-2}	2.37×10^{-2}	2.37×10^{-2}
SiC	5.75×10^{-12}	5.55×10^{-12}	3.28×10^{-12}	2.46×10^{-12}	6.45×10^{-12}	6.73×10^{-12}	5.41×10^{-12}	5.72×10^{-12}
TiC	1.24×10^{-11}	1.27×10^{-11}	7.34×10^{-12}	5.61×10^{-12}	9.94×10^{-12}	1.13×10^{-11}	1.07×10^{-11}	1.45×10^{-11}
Si	2.23×10^{-19}	2.46×10^{-13}	4.49×10^{-7}	2.64×10^{-7}	0	0	7.82×10^{-35}	3.11×10^{-9}
SiO_2	2.15×10^{-7}	3.14×10^{-7}	2.41×10^{-7}	1.81×10^{-2}	3.37×10^{-7}	3.24×10^{-7}	2.70×10^{-7}	3.02×10^{-7}
$MgSiO_3$	4.63×10^{-6}	4.11×10^{-6}	3.37×10^{-6}	1.02×10^{-3}	1.97×10^{-6}	1.78×10^{-6}	5.22×10^{-6}	3.92×10^{-6}
Mg_2SiO_4	1.47×10^{-2}	4.30×10^{-2}	6.13×10^{-2}	8.71×10^{-2}	1.57×10^{-5}	1.41×10^{-5}	4.44×10^{-3}	5.35×10^{-2}

Table A.3 (cont'd)

Dust Species	Models							
MgO	2.36×10^{-8}	6.02×10^{-7}	6.99×10^{-7}	8.22×10^{-7}	3.60×10^{-8}	3.33×10^{-8}	2.98×10^{-8}	6.08×10^{-7}
Al_2O_3	1.14×10^{-2}	1.80×10^{-2}	1.09×10^{-2}	8.66×10^{-3}	5.62×10^{-4}	3.46×10^{-3}	9.61×10^{-3}	1.92×10^{-2}
FeO	3.11×10^{-6}	4.33×10^{-6}	3.18×10^{-6}	2.27×10^{-6}	4.56×10^{-6}	4.26×10^{-6}	3.81×10^{-6}	4.14×10^{-6}
Fe_3O_4	4.25×10^{-5}	6.67×10^{-5}	5.08×10^{-5}	3.72×10^{-5}	6.56×10^{-5}	6.12×10^{-5}	5.16×10^{-5}	6.40×10^{-5}
Total	4.99×10^{-2}	8.49×10^{-2}	9.62×10^{-2}	1.38×10^{-1}	2.43×10^{-2}	2.72×10^{-2}	3.78×10^{-2}	9.66×10^{-2}
	M20cE2.76	M20cE2.85	M20cE5.03	M20cE8.86	M20dE4.3	M20dE5.9	M20dE18.1	M20dE64.5
C	2.37×10^{-2}	2.37×10^{-2}	2.38×10^{-2}	2.42×10^{-2}	1.47×10^{-2}	2.30×10^{-2}	2.37×10^{-2}	2.36×10^{-2}
SiC	3.30×10^{-12}	3.30×10^{-12}	9.78×10^{-11}	3.02×10^{-10}	5.73×10^{-13}	2.50×10^{-13}	3.16×10^{-13}	7.28×10^{-14}
TiC	7.45×10^{-12}	6.80×10^{-12}	4.97×10^{-12}	3.49×10^{-12}	1.59×10^{-12}	6.30×10^{-13}	5.01×10^{-13}	1.47×10^{-13}
Si	4.72×10^{-7}	4.29×10^{-7}	2.02×10^{-7}	5.47×10^{-4}	3.11×10^{-12}	4.39×10^{-11}	5.86×10^{-9}	3.58×10^{-9}
SiO_2	2.33×10^{-7}	7.95×10^{-7}	2.50×10^{-2}	3.21×10^{-3}	1.02×10^{-1}	9.35×10^{-8}	1.64×10^{-7}	1.45×10^{-7}
$MgSiO_3$	2.41×10^{-5}	2.32×10^{-5}	1.02×10^{-3}	6.83×10^{-3}	2.41×10^{-5}	3.64×10^{-6}	2.53×10^{-6}	2.22×10^{-6}
Mg_2SiO_4	6.89×10^{-2}	6.86×10^{-2}	8.70×10^{-2}	8.76×10^{-2}	6.44×10^{-2}	4.64×10^{-2}	2.11×10^{-2}	1.22×10^{-2}
MgO	6.59×10^{-7}	7.35×10^{-7}	7.60×10^{-7}	2.02×10^{-6}	1.73×10^{-6}	5.26×10^{-6}	6.62×10^{-7}	5.76×10^{-7}
Al_2O_3	1.19×10^{-2}	1.09×10^{-2}	8.58×10^{-3}	3.63×10^{-3}	2.64×10^{-3}	7.47×10^{-3}	5.58×10^{-3}	2.46×10^{-3}
FeO	3.05×10^{-6}	3.05×10^{-6}	2.01×10^{-6}	1.36×10^{-6}	7.79×10^{-7}	1.49×10^{-6}	2.08×10^{-6}	1.72×10^{-6}
Fe_3O_4	4.88×10^{-5}	4.90×10^{-5}	3.31×10^{-5}	2.32×10^{-5}	1.42×10^{-5}	2.78×10^{-5}	3.57×10^{-5}	2.95×10^{-5}
Total	1.04×10^{-1}	1.03×10^{-1}	1.45×10^{-1}	1.31×10^{-1}	1.84×10^{-1}	7.70×10^{-2}	5.05×10^{-2}	3.84×10^{-2}
	M20E78.9	M20dE88.4	M20dE124.0	M25aE0.99	M25aE1.57	M25aE4.73	M25aE6.17	M25aE7.42
C	2.00×10^{-2}	1.44×10^{-2}	1.12×10^{-2}	1.37×10^{-2}	1.37×10^{-2}	1.38×10^{-2}	1.39×10^{-2}	1.39×10^{-2}

Table A.3 (cont'd)

Dust Species	Models							
SiC	1.48×10^{-12}	3.84×10^{-13}	4.61×10^{-14}	7.82×10^{-13}	4.63×10^{-13}	2.09×10^{-13}	1.56×10^{-13}	1.37×10^{-13}
TiC	4.62×10^{-13}	1.08×10^{-12}	1.00×10^{-13}	1.96×10^{-12}	1.15×10^{-12}	7.05×10^{-13}	4.86×10^{-13}	4.67×10^{-13}
Si	8.61×10^{-9}	2.68×10^{-12}	2.26×10^{-15}	4.86×10^{-6}	7.67×10^{-7}	1.34×10^{-1}	1.16×10^{-1}	1.22×10^{-1}
SiO_2	1.51×10^{-4}	1.24×10^{-4}	1.20×10^{-2}	5.92×10^{-8}	4.26×10^{-8}	4.19×10^{-2}	5.43×10^{-2}	4.59×10^{-2}
$MgSiO_3$	3.18×10^{-6}	8.09×10^{-5}	2.18×10^{-5}	7.67×10^{-7}	1.11×10^{-6}	1.13×10^{-3}	2.26×10^{-3}	3.05×10^{-3}
Mg_2SiO_4	1.54×10^{-2}	4.50×10^{-2}	1.69×10^{-3}	3.59×10^{-2}	6.15×10^{-2}	1.60×10^{-1}	2.62×10^{-1}	2.77×10^{-1}
MgO	4.21×10^{-2}	2.48×10^{-3}	7.47×10^{-6}	1.20×10^{-7}	8.15×10^{-8}	8.00×10^{-8}	5.18×10^{-7}	7.36×10^{-6}
Al_2O_3	4.93×10^{-3}	4.37×10^{-3}	7.11×10^{-5}	9.32×10^{-3}	1.42×10^{-2}	1.91×10^{-2}	2.41×10^{-2}	1.97×10^{-2}
FeO	3.76×10^{-5}	1.06×10^{-6}	3.72×10^{-7}	7.86×10^{-7}	5.55×10^{-7}	1.01×10^{-6}	8.11×10^{-7}	9.69×10^{-7}
Fe_3O_4	1.51×10^{-3}	1.55×10^{-5}	7.91×10^{-6}	1.16×10^{-5}	8.30×10^{-6}	1.49×10^{-5}	1.31×10^{-5}	1.80×10^{-5}
Total	8.45×10^{-2}	6.65×10^{-2}	2.51×10^{-2}	5.90×10^{-2}	8.95×10^{-2}	4.76×10^{-1}	5.21×10^{-1}	5.31×10^{-1}
	M25aE14.8	M25bE8.40	M25bE9.73	M25bE18.4	M25d3E0.89	M25d3E0.92	M25d3E1.04	M25d3E1.20
C	1.48×10^{-2}	1.39×10^{-2}	1.39×10^{-2}	1.40×10^{-2}	1.37×10^{-2}	1.37×10^{-2}	3.60×10^{-3}	1.98×10^{-3}
SiC	1.13×10^{-13}	1.71×10^{-13}	1.93×10^{-13}	5.79×10^{-14}	4.97×10^{-13}	9.73×10^{-11}	8.99×10^{-10}	1.63×10^{-9}
TiC	4.99×10^{-13}	6.13×10^{-13}	6.77×10^{-13}	1.65×10^{-13}	1.30×10^{-12}	5.97×10^{-13}	3.99×10^{-12}	1.36×10^{-12}
Si	1.78×10^{-1}	3.43×10^{-5}	8.73×10^{-4}	5.31×10^{-5}	3.58×10^{-6}	1.20×10^{-1}	1.20×10^{-1}	1.17×10^{-1}
SiO_2	9.06×10^{-2}	8.47×10^{-2}	1.11×10^{-1}	2.12×10^{-2}	5.93×10^{-8}	2.34×10^{-1}	5.57×10^{-2}	2.82×10^{-2}
$MgSiO_3$	7.19×10^{-3}	3.91×10^{-2}	1.10×10^{-3}	2.60×10^{-3}	7.11×10^{-7}	1.50×10^{-3}	2.27×10^{-2}	1.23×10^{-3}
Mg_2SiO_4	8.90×10^{-2}	2.46×10^{-1}	2.56×10^{-1}	1.03×10^{-1}	3.68×10^{-2}	2.08×10^{-1}	1.73×10^{-1}	2.57×10^{-2}
MgO	1.35×10^{-4}	8.59×10^{-6}	3.89×10^{-10}	7.67×10^{-5}	1.07×10^{-7}	5.08×10^{-8}	3.27×10^{-5}	8.42×10^{-5}

Table A.3 (cont'd)

Dust Species	Models							
Al_2O_3	2.30×10^{-3}	6.48×10^{-3}	5.29×10^{-2}	1.62×10^{-3}	9.70×10^{-3}	4.82×10^{-2}	2.51×10^{-3}	9.10×10^{-4}
FeO	1.43×10^{-6}	3.11×10^{-7}	1.70×10^{-7}	1.12×10^{-6}	7.91×10^{-7}	2.17×10^{-6}	8.58×10^{-7}	1.24×10^{-6}
Fe_3O_4	3.05×10^{-5}	5.68×10^{-6}	3.81×10^{-6}	2.22×10^{-5}	1.16×10^{-5}	4.03×10^{-5}	1.76×10^{-5}	2.65×10^{-5}
Total	3.88×10^{-1}	3.91×10^{-1}	4.36×10^{-1}	1.43×10^{-1}	6.03×10^{-2}	6.93×10^{-1}	5.38×10^{-1}	5.31×10^{-1}
	M25d2E2.53	M25d2E2.64	M25d2E2.78	M25d2E3.07	M25d1E3.30	M25d1E4.72	M25d1E7.08	
C	1.37×10^{-2}	1.37×10^{-2}	1.37×10^{-2}	4.44×10^{-3}	1.37×10^{-2}	1.37×10^{-2}	1.37×10^{-2}	
SiC	1.54×10^{-12}	1.28×10^{-12}	8.54×10^{-13}	7.19×10^{-11}	6.65×10^{-13}	4.26×10^{-13}	1.74×10^{-11}	
TiC	5.57×10^{-12}	4.11×10^{-12}	2.12×10^{-12}	3.34×10^{-12}	1.70×10^{-12}	1.29×10^{-12}	6.07×10^{-13}	
Si	8.12×10^{-3}	7.20×10^{-2}	7.20×10^{-2}	1.39×10^{-1}	7.88×10^{-2}	7.29×10^{-2}	7.26×10^{-2}	
SiO_2	3.05×10^{-1}	3.29×10^{-1}	1.85×10^{-1}	5.76×10^{-2}	1.26×10^{-1}	3.40×10^{-1}	3.38×10^{-1}	
$MgSiO_3$	5.58×10^{-4}	1.07×10^{-4}	2.62×10^{-3}	1.07×10^{-3}	1.96×10^{-3}	5.35×10^{-5}	6.67×10^{-5}	
Mg_2SiO_4	2.53×10^{-1}	2.52×10^{-1}	2.52×10^{-1}	1.98×10^{-2}	2.52×10^{-1}	2.52×10^{-1}	2.52×10^{-1}	
MgO	2.13×10^{-7}	5.97×10^{-8}	1.43×10^{-9}	6.74×10^{-5}	1.45×10^{-9}	9.97×10^{-10}	7.16×10^{-3}	
Al_2O_3	4.28×10^{-2}	4.42×10^{-2}	4.78×10^{-2}	7.86×10^{-4}	5.58×10^{-2}	5.70×10^{-2}	5.70×10^{-2}	
FeO	1.20×10^{-5}	8.67×10^{-6}	2.11×10^{-6}	1.38×10^{-6}	7.25×10^{-7}	9.78×10^{-6}	1.02×10^{-5}	
Fe_3O_4	5.68×10^{-4}	7.39×10^{-4}	3.91×10^{-5}	2.90×10^{-5}	1.23×10^{-5}	1.07×10^{-3}	1.72×10^{-3}	
Total	6.26×10^{-1}	7.35×10^{-1}	5.89×10^{-1}	3.05×10^{-1}	5.31×10^{-1}	7.40×10^{-1}	7.68×10^{-1}	

Note. — The single element Fe-group grain species are excluded from this table due to very inconsistent non-negligible yields. Entries with a dash line indicate negligible and effectively zero amounts of that species being produced for the given model.